國立臺灣大學工學院應用力學研究所

博士論文

Institute of Applied Mechanics
College of Engineering
National Taiwan University

Doctoral Dissertation

結合聲電效應之板波與表面聲波感測器研製

Development of Surface and Lamb Wave Sensors using Acoustoelectric Effect

王偉姍

Wei-Shan Wang

指導教授：吳政忠 教授

Advisor: Tsung-Tsong Wu, Professor

中華民國 98 年 10 月

October, 2009

謝誌

本論文得以完成，最感謝恩師 吳政忠教授多年來的指導及鼓勵。為學期間，吳老師不斷激勵學生於研究上培養獨立思考與解決問題的能力。當學生迷失方向時，吳老師對學生的包容、適時指出盲點與協助解決難題，更使學生獲益匪淺。此外，吳老師於日常言談中所展現對社會的關懷，更讓學生有著深刻的啟發。吳老師無論是研究或生活上的身教與言教，實為學生心目中學者的典範。在恩師的諄諄教誨下，學生始得今日之成長，感激之情難以言表。

承蒙義守大學 沈季燕教授，交通大學 尹慶中教授，以及本校 馬劍清教授、黃榮山教授於百忙中撥冗擔任學生論文口試委員，對本論文不吝指正，並提供許多精闢見解與寶貴意見，始能改進文中諸項缺失，使之更臻完備。在此表達誠摯的謝意。

論文研究期間，由衷感謝超聲波實驗室所有夥伴在學業上的幫忙及生活上的照顧。特別感謝童建樺博士、徐文信博士、陳永裕博士、孫嘉宏博士、黃自貴博士與許進成博士，無論於研究或學習態度上，皆在學生受挫時適時提供指導與學習經驗。感謝各屆從實驗室畢業的學長學弟們，離開學校後仍不忘關心並給予我精神上的支持。感謝維志、亞珊、正賢、兆誼、哲原、景翔、亞倫、貫綸、鎮宇、智偉、山松、彥廷等學弟妹於實驗上的協助與生活中不斷關心與打氣，使得論文撰寫期間即使辛苦，卻不致感到孤獨無援。感謝蕭俊卿教授、自強基金會林秀芬小姐、志明、啟銘、順區等在儀器設備或製程技術上鼎力相助，使微製程最後得以完成。在應力所求學至今，轉眼已數載，這段期間認識了許多人，也曾麻煩過許多人，對於曾經鼓勵、支持與幫忙我的好友們，在此一併感謝。與各位的情誼，無非是我在應力所的日子裡，除了求學之外最大的收穫。

最後，感謝父親 王清波先生、母親 鄧秀美女士、大姊翠綾與二姊秋嵐。感謝家人這些年來對我的包容與無微不至的關心照顧，總是在旁給予我最大的支持，並默默陪伴我走過一切。家人所給予我的溫暖，是我一直以來最大的精神支柱與動力來源，使我得以完成學業。

謹將此論文獻給幫助過我的師長、朋友，以及我最愛的家人。

中文摘要

由於體積小、敏感度高，表面聲波與板波感測器已廣泛應用於各式感測，而聲電效應即為其重要感測機制之一。然由於板波之傳播機制較徹體波或表面聲波複雜許多，現存文獻中仍缺聲電效應與板波波傳之互制行為探討。有鑑於此，本論文分析聲電效應作用下，表面波與板波感測器之特性，並藉以為研製微尺寸板波感測器之基礎。在實驗方面，文中首度研製以氧化鋅奈米結構為感測材料之表面聲波紫外光感測器，更以氧化鋅薄板同時激發板波與作為感測層，製作出一板波紫外光感測器，並分別探討其特性。

本文首先介紹表面聲波傳遞時受聲電效應影響之理論模型，並討論當一壓電半導體材料與自由載子產生交互作用時，其表面波波速、衰減係數與壓電半導體導電度之變化。接著，針對板波，對聲電效應理論模型引入頻散關係，並以此修正之聲電效應理論，探討板波受自由載子影響時之傳播特性。文中以氧化鋅材料為例，研究在聲電效應影響下單層板與多層板板波之傳遞行為。

為了探討聲電效應於表面波傳遞時之影響，本文製作一以氧化鋅奈米柱為感測材料之表面聲波紫外光感測系統，並針對其即時監測之效能、靈敏度、重複性與穩定性做測試與討論。此外，亦首度將量測到的頻率漂移代入聲電效應之理論模型，反算出受紫外光照射一段時間後之氧化鋅導電度，並與理論做一比較與研究。

以第二章板波頻散關係與聲電效應互制之分析為基礎，本文研製一新型板波紫外光感測器。文中，分別製作出氧化鋅/氮化矽/矽結構與氧化鋅/氮化矽薄板之板波紫外光感測器，並對此兩種感測器做量測與比較。研究成果顯示在 0.06mWcm^{-2} 的紫外光照射下，以氧化鋅/氮化矽薄板為結構之板波紫外光感測器有明顯的波傳損失。表示引入板波頻散關係後，此修正之聲電效應理論可成功設計出感測效能優異之板波感測器。

綜言之，本文提出一分析聲電效應與板波波傳之理論模式，可用於設計單層或多層板板波感測器。在實驗方面，本文基於理論分析設計，亦首度製作出以氧化鋅奈米柱為感測層之表面聲波紫外光感測器以及氧化鋅/氮化矽薄板之板波紫外光感測器。

關鍵字：聲波感測器 、聲電效應、表面波、板波、紫外光

ABSTRACT

Surface and Lamb wave sensors, with advantages such as small volume and high sensitivity, have been widely used in various sensing applications. Acoustoelectric effect, which arises from the interaction of acoustic waves and mobile carriers, is one of important sensing mechanisms of acoustic wave sensors. Nevertheless, Lamb wave propagation is much more complex than bulk and surface waves; in the meanwhile, discussions of the influences of acoustoelectric effect on Lamb wave propagation in the literatures remain little thus far. In this regard, characteristics of surface and Lamb wave sensors affected by acoustoelectric interaction are theoretically investigated, which provide a principle and method for designing Lamb wave microsensors for further applications. In addition, a ZnO-nanorods surface acoustic wave UV sensor and a silicon-based ZnO-membrane Lamb wave UV microsensor both employing acoustoelectric effect are realized and demonstrated respectively for the first time.

First, an acoustoelectric effect model which has been employed surface wave propagation is briefly introduced. Characteristics of a piezoelectric semiconductor interacting with mobile carriers, such as velocity change, attenuation and conductivity are discussed. In particular, by introducing dispersion relations, a model associated with the acoustoelectric effect is modified to deal with interactions of Lamb waves and mobile carriers. A piezoelectric semiconducting ZnO material is used as a numerical example to discuss Lamb wave propagation influenced by acoustoelectric interaction in a single and multi-layered plate respectively.

Next, to reveal the effect of the acoustoelectric interactions on surface wave propagation, a ZnO-nanorod based UV detector system is demonstrated. Characteristics of this UV detector

such as real-time response, sensitivity, repeatability and stability are discussed. In addition, ZnO conductivities under 365nm illuminations for a period of time are derived and discussed by substituting measured frequency shifts into the acoustoelectric model for the first time.

Finally, based on the analysis of the acoustoelectric-effect model for Lamb wave propagation presented in chapter 2, a novel silicon-based Lamb wave UV microsensor is demonstrated for the first time. For comparison, two types of Lamb wave UV microsensors, based on a $ZnO/Si_3N_4/Si$ structure and an ultra-thin ZnO/Si_3N_4 membrane respectively, are realized and discussed. Results show that the ZnO/Si_3N_4 membrane has obvious acoustic losses when the sensor is under a $0.06mWcm^{-2}$ UV illumination, which implies through proper design, a Lamb wave microsensor is a promising candidate for sensing application using acoustoelectric effect.

In brief, influences of acoustoelectric effect on surface and Lamb waves are theoretically investigated. For experimental verifications, a ZnO-nanorod based surface-wave UV sensor and a Lamb wave UV detector based on an ultra-thin ZnO/Si_3N_4 membrane are designed and realized for the first time.

Keywords: Acoustic wave sensor, Acoustoelectric effect, Surface acoustic waves, Lamb waves, Ultraviolet

CONTENTS

謝誌 i

中文摘要 ii

ABSTRACT iii

CONTENTS v

SYMBOLS viii

LIST OF FIGURES xi

LIST OF TABLES xv

Chapter 1 Introduction 1

1.1 Motives 1

1.2 Literature Review 4

1.3 Outline of the Dissertation 9

Chapter 2 Acoustoelectric Effect in Piezoelectric Semiconductors 11

2.1 Acoustoelectric Effect in a Piezoelectric Semiconductor 11

2.2 Influences of Acoustoelectric Effect on Surface Acoustic Wave Propagations 16

2.2.1 Electromechanical Coupling Coefficient 16

2.2.2 Characteristics of Surface Acoustic Wave Propagation Affected by Acoustoelectric Effect 18

2.3 A Modified Acoustoelectric-Effect Model for Lamb Wave Propagation in Piezoelectric Semiconductors 23

2.3.1 Dispersion of Lamb Waves in a Single/Layered Structure 23

2.3.2 Acoustoelectric Effect in a Single Piezoelectric Semiconductor Plate 27

2.3.3 Acoustoelectric Effect in a Multi-layered Plate Structure 29

2.4 Temperature Effect on Acoustoelectric Interaction 32

Chapter 3 A ZnO-Nanorod Based SAW Sensor for Ultraviolet Detection 45

3.1 Design of a SAW oscillator system based on $ZnO/LiNbO_3$ structure 45

3.1.1 Design of a SAW Resonator 46

3.1.2 Electrical Circuit Design 48

3.2 Fabrication of a SAW Device with ZnO-Nanorods Sensing Material 49

3.2.1 Fabrication of a SAW device 49

3.2.2 ZnO Nanorod Growth 52

3.3 Measurement of SAW Oscillators 54

3.3.1 Single SAW Oscillator 54

3.3.2 Dual-Channel-Configuration SAW Oscillators 55

3.4 An Ultraviolet Detector based on a SAW Oscillator System with ZnO-Nanorods Sensing Material 55

3.4.1 Experimental Setup of a Ultraviolet Sensing System 56

3.4.2 Characteristics of the Ultraviolet Detector 56

3.4.3 Calculation of ZnO Conductivities Using the Acoustoelectric Effect 59

Chapter 4 A Silicon-based Lamb Wave Sensor for Ultraviolet Detection 77

4.1 Design of a Silicon-based Lamb Wave Device 77

4.1.1 Dispersions of a Si-based Surface Wave Device 78

4.1.2 Design Consideration of a Si-based Lamb Wave Device 79

4.2 Fabrication of a Silicon-based Lamb Wave Device 81

4.3 Measurement of Silicon-based Acoustic Wave Devices 85

4.3.1 Characteristics of Si_3N_4 and ZnO Thin Films 85

4.3.2 SAW Signals of a $ZnO/Si_3N_4/Si$ Layered Structure 87

4.3.3 Lamb Wave Signals of a $ZnO/Si_3N_4/Si$ structure 88

4.3.4 Lamb Wave Signal of a ZnO/ Si_3N_4 Membrane 90
4.4 An Silicon-based Lamb-Wave Ultraviolet Microsensor 90
4.4.1 Construction of a Silicon-based Lamb Wave UV Detecting System 91
4.4.2 Characteristics of Lamb Wave UV microsensors 91
Chapter 5 Conclusions and Prospects 117
5.1 Conclusions 117
5.2 Prospects 120
Appendix A 123
A.1 Piezoelectric Constitutive Relations and Equations of Motion 123
A.2 Poisson's Equation and the Continuity Equation 124
A.3 Wave Equations of a Piezoelectric Semiconductor 126
A.4 Acoustoelectric Effect of a Piezoelectric Semiconductor 128
Appendix B 135
REFERENCES 139

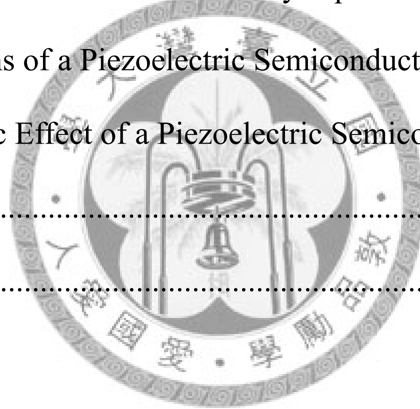

SYMBOLS

Chapter 2

Symbol	Meaning	First Appearance
τ_{ij}	Stress field	(2.1)
ρ	Mass density	(2.1)
u_i	Mechanical displacement component	(2.1)
C_{ijkl}	Elastic stiffness constant	(2.2)
ϕ	Electric potential	(2.2)
e_{lij}	Piezoelectric constants	(2.2)
D_i	Electric displacement	(2.3)
ε_{il}	Permittivity	(2.3)
q	Magnitude of the electronic charge	(2.4)
n_s	Number of electrons per unit volume required to produce the free charge	(2.4)
J_i	Volume current density	(2.5)
f	Fraction of the acoustically-produced mobile space charge	(2.6)
n	Mean current density	(2.6)
μ_{ij}	Electron mobility	(2.6)
β	Constant related to Boltzmann's constant and temperature	(2.6)
ω	Circular frequency	(2.7)

k	Wave number	(2.7)
$\overline{C}_{ijkl}$	Complex elastic constant	(2.7)
ℓ	a unit element in the propagation direction	(2.8)
ω_C	Conductivity frequency	(2.9)
v	Phase velocity	(2.10)
v_0	Phase velocity in a non-piezoelectric insulator	(2.10)
Γ	Adsorption constant	(2.11)
K^2	Electromechanical coupling coefficient	(2.12)
K_{eff}^2	Effective coupling coefficient of surface waves	(2.15)
Γ_S	Coupling parameter	(2.15)
$\varepsilon_S^{(\infty)}$	Effective permittivity at infinite slowness	(2.15)
β	Phase constant	(2.16)
k_x	Wave number when the wave propagates in the x direction	(2.16)
$\beta_l(f)$	Dispersive phase constant	(2.17)
f	Frequency	(2.17)
$v(f)$	Velocity dispersion on a free surface	(2.17)
v_o	SAW phase velocity on a free surface	(2.18)
v_m	SAW phase velocity on a metalized surface	(2.18)
Δv	Velocity difference of v_o and v_m	(2.18)
σ	Conductivity	(2.21)
ε_S	Permittivity of a semiconductor	(2.21)

ε_P	Permittivity of a piezoelectric insulator	(2.21)
ε_0	Permittivity in vacuum	(2.24)
J_S	surface current density	(2.25)
E_x	Electric field in *x* direction	(2.25)
d	Thickness of a semiconducting film	(2.25)
τ_C	Relaxation time	(2.29)
σ_d	Sheet conductivity	(2.32)
σ_m	Material constant of a piezoelectric insulator	(2.33)
$\boldsymbol{\xi}$	State vector	(2.36)
$\mathbf{N}$	Fundamental acoustic tensor	(2.36)
$\mathbf{u}$	Displacement vector	(2.37)
$\mathbf{t}$	Traction vector	(2.39)
$\mathbf{T}$	Generalized traction vector	(2.43)
$\mathbf{G}$	Surface impedance tensor	(2.43)
$\mathbf{U}$	Generalized displacement vector	(2.43)
$\mathbf{G}_0$	Surface impedance tensor	(2.44)
$K_{eff}^2(f)$	Dispersive coupling coefficient	(2.46)
$v_o(f)$	Dispersive Lamb wave phase velocity	(2.46)
$k_x(f)$	Dispersive wave number	(2.47)
m^*	Effective mass	(2.48)
T	Temperature	(2.48)

LIST OF FIGURES

Fig. 2.1 Acoustic velocity shift and attenuation due to AE interaction in an unbounded piezoelectric semiconductor 34

Fig. 2.2 Surface waves propagating on a piezoelectric insulator with an adjacent semiconductor 34

Fig. 2.3 Surface waves propagates on a surface made up of an ultra- semiconducting film on a piezoelectric insulator 35

Fig. 2.4 SAW velocity change and attenuation on a $LiNbO_3$ substrate with a thin sheet of mobile carriers 35

Fig. 2.5 Surface waves propagating in a piezoelectric semiconductor 36

Fig. 2.6 SAW Velocity change of ZnO due to AE interaction 36

Fig. 2.7 SAW attenuation of ZnO in units of coupling coefficient 37

Fig. 2.8 A laminated plate structure 37

Fig. 2.9 A piezoelectric plate with a free down surface 38

Fig. 2.10 Phase velocity dispersion of a ZnO plate with free down surface 38

Fig. 2.11 Coupling coefficient of a ZnO plate with free down surface 39

Fig. 2.12 A piezoelectric plate with a metalized down surface 39

Fig. 2.13 Coupling coefficient of lowest antisymmetric mode in a ZnO plate with metalized down surface 40

Fig. 2.14 Phase velocity dispersion of a $ZnO/Si_3N_4/SiO_2$ laminated plate 40

Fig. 2.15 Coupling coefficient of a $ZnO/Si_3N_4/SiO_2$ laminated plate 41

Fig. 2.16 Velocity changes of A0 mode of a ZnO plate due to AE interaction 41

Fig. 2.17 Loss of A0 mode of a ZnO plate due to AE interaction 42

Fig. 2.18 Velocity change of a ZnO/Si_3N_4/SiO2 plate due to AE interaction 42

Fig. 2.19 Loss of a ZnO/ Si_3N_4/SiO2 due to AE interaction 43
Fig. 2.20 Velocity shifts of different layered structure due to AE interactions 43
Fig. 2.21 Acoustic loss of different layered structure due to AE interactions 44
Fig. 3.1 A schematic diagram of a two-port SAW device 62
Fig. 3.2 Simulated frequency response of a two-port SAW device 63
Fig. 3.3 Configuration of a SAW-based oscillating loop 63
Fig. 3.4 Layout of an amplifier circuit 64
Fig. 3.5 Simulation result of the amplifier response 64
Fig. 3.6 Flow chart of a SAW resonator fabrication process 65
Fig. 3.7 Frequency response of a two-port SAW device 66
Fig. 3.8 Frequency response of a SAW device with ZnO film 66
Fig. 3.9 The XRD pattern of ZnO film 67
Fig. 3.10 A top-view SEM image of ZnO nanorods 67
Fig. 3.11 The XRD pattern of ZnO nanorods 68
Fig. 3.12 A UV-Vis absorption curve of ZnO nanorods 68
Fig. 3.13 Frequency response of a SAW device with ZnO nanorod 69
Fig. 3.14 Phase of a SAW device with ZnO nanorod 69
Fig. 3.15 Frequency response of a SAW device with over-height ZnO nanorods 70
Fig. 3.16 A schematic of a two-port SAW oscillator 70
Fig. 3.17 Signal of a two-port SAW oscillator 71
Fig. 3.18 A dual-channel SAW oscillator system 71
Fig. 3.19 Frequency and time domain signal of the oscillator system 72
Fig. 3.20 Experimental setup of a UV sensing system 72
Fig. 3.21 Response of a UV detector under UV illumination 73
Fig. 3.22 Response of a UV detector under 650 nm illumination 73

Fig. 3.23 Response of a UV detector toward different light power densities 74
Fig. 3.24 Response of a UV detector under 365nm UV illumination for 10 s 74
Fig. 3.25 Velocity shifts of different 365nm power densities 75
Fig. 3.26 Average sheet conductivities under 365nm illuminations for a period of time 75
Fig. 3.27 Conductivity range of the UV detector 76
Fig. 4.1 A ZnO/ SiN_x /Silicon surface wave device 95
Fig. 4.2 A ZnO/ SiN_x /Silicon Lamb wave device 96
Fig. 4.3 A ZnO/SiN_x Lamb wave device 96
Fig. 4.4 SAW velocity dispersion of ZnO/SiN_x/Si 97
Fig. 4.5 Coupling coefficient of SAW on ZnO/SiN_x/Si structures 97
Fig. 4.6 Velocity dispersion of SAW and A_0 mode in ZnO/SiNx/Si 98
Fig. 4.7 Coupling coefficient of SAW and A_0 mode in ZnO/SiNx/Si 98
Fig. 4.8 A_0 mode of Lamb wave dispersion in ZnO/SiN_x 99
Fig. 4.9 Coupling coefficient of A_0 mode in ZnO/SiN_x 99
Fig. 4.10 Fabrication process of a Si-based Lamb wave device 100
Fig. 4.11 Si_3N_4 membrane (a) before annealing (b) after annealing 102
Fig. 4.12 XRD pattern of a ZnO thin film 102
Fig. 4.13 EDS pattern of ZnO/Si_3N_4/ Si structure patterned with IDTs 103
Fig. 4.14 Photograph of IDTs and gratings, linwidth= 2 micron 103
Fig. 4.15 Frequency response of a ZnO/Si_3N_4/Si SAW device, IDT wavelength=8 micron104
Fig. 4.16 Time domain of a ZnO/Si_3N_4/Si SAW device 104
Fig. 4.17 Time-gated SAW signal of a ZnO/Si_3N_4/Si structure 105
Fig. 4.18 SAW signal of a ZnO/Si_3N_4/Si structure, IDT wavelength=9.8 micron 105
Fig. 4.19 SAW signal of a ZnO/Si_3N_4/Si structure, IDT wavelength=12 micron 106
Fig. 4.20 Time domain of a ZnO/Si_3N_4/Si Lamb wave device, wavelength=8 micron 106

Fig. 4.21 Lamb wave signal of a $ZnO/Si_3N_4/Si$ structure, wavelength=8 micron 107
Fig. 4.22 Lamb wave signal of a $ZnO/Si_3N_4/Si$ structure, wavelength=9.8 micron 107
Fig. 4.23 Lamb wave signal of a $ZnO/Si_3N_4/Si$ structure, wavelength=12 micron 108
Fig. 4.24 A photograph of a ZnO/Si_3N_4 Lamb wave device 108
Fig. 4.25 Frequency response of a ZnO/Si_3N_4 Lamb wave device 109
Fig. 4.26 Time domain of a ZnO/Si_3N_4 Lamb wave device..109
Fig. 4.27 Time-gated Lamb wave signal of a ZnO/Si_3N_4 membrane 110
Fig. 4.28 A Lamb wave UV sensing system 110
Fig. 4.29 Response of a $ZnO(0.5)/Si_3N_4(1)/Si(7)$ Lamb wave UV sensor under 370nm illumination 111
Fig. 4.30 Time-gated signal of a $ZnO(0.5)/Si_3N_4(1)/Si(7)$ Lamb wave UV sensor under 370nm illumination 111
Fig. 4.31 Response of a $ZnO(0.5)/Si_3N_4(1)/Si(7)$ Lamb wave UV sensor under 650nm illumination 112
Fig. 4.32 Time-gated signal of a $ZnO(0.5)/Si_3N_4(1)/Si(7)$ Lamb wave UV sensor under 650nm illumination 112
Fig. 4.33 Response of a $ZnO(0.5)/Si_3N_4(1)$ Lamb wave UV sensor under 370nm illumination 113
Fig. 4.34 Time-gated signal of a $ZnO(0.5)/Si_3N_4(1)$ Lamb wave UV sensor under 370nm illumination 113
Fig. 4.35 Response of a $ZnO(0.5)/Si_3N_4(1)$ Lamb wave UV sensor under 650nm illumination 114
Fig. 4.36 Time-gated signal of a $ZnO(0.5)/Si_3N_4(1)$ Lamb wave UV sensor under 650nm illumination 114
Fig. 4.37 Attenuation due to the AE effect in Si-based Lamb wave sensors 115

LIST OF TABLES

Table 3.1 Properties of several piezoelectric substrates..62

Table 4.1 IDT parameters 95

Chapter 1 Introduction

1.1 Motives

Microsensors, which have at least one physical dimension at the submillimeter level, are miniature electronic devices that give information about physical, chemical or biological properties and convert these properties into signals read by an instrument. With several key developments such as the invention of integrated microelectronic circuitry and micro-electro-mechanical system (MEMS) technologies, various types of microsensors have been designed and realized for over decades. Compared with the conventional counterparts, microsensors made with the MEMS technologies have several advantages such as less bulky, much lighter, lower power consumption, more sensitive, and less invasive than larger devices. Furthermore, the cost can be reduced by the mass production of wafers for high volume[1]. In the past few years, MEMS-based microsensors even had the largest share of the global microsensors market. A strong growth of MEMS-based microsensors is also expected in the future.[2] Thus, the MEMS-based microsensors have drawn much attention in recent years and are worth studying.

There are innumerable applications for microsensors, which can be categorized in military, aerospace, automotive industry, process industry, home automation, information technology, consumer electronics, life science, medicine, and environmental monitoring and control. In recent years, largest markets for microsensors are the automotive industry, military and aerospace applications. However, numerous emerging microsensors are highly needed to be developed to meet the requirements of applications such as home automation, medical, environmental monitoring and life science which strongly influence our daily life.

Basically, an ideal sensor should have attributes including high sensitivity, selectivity,

high reliability, fast and linear response, high signal-to-noise ratio, fully reversible behavior, insensitive to surrounding environmental conditions, compact, easy to fabricate, low cost, etc.[1] Several sensing principles for microsensors, for example, are optical, electrical, acoustic, magnetic, and thermal. Among these, acoustic wave sensors are conveniently small, competitively priced, and capable of measuring various input quantities[3,4]. By combining CMOS and MEMS technologies, acoustic wave sensors, which are fabricated on a semiconductor substrate such us silicon, and electric circuits can easily be integrated into a single chip[5,6]. Moreover, acoustic wave sensors have benefit of being passively, which offer an advantage of being wireless sensors used for remote monitoring and control, even in harsh environment.[7] With advantages mentioned above, acoustic wave sensors have become indispensable to nowadays microsensors applications.

Acoustic waves have various forms of propagation and are guided by the properties and the boundaries of the media in which they propagate.[8] Bulk acoustic waves (BAW) are the elastic waves propagating in the interior of an unbounded medium in which just two vibrations, longitudinal and transverse, are supported. Surface acoustic waves (SAW), known as the Rayleigh waves, were discovered by Lord Rayleigh in 1885[9]. This kind of acoustic modes travels in semi-infinite solids, with nearly all the acoustic energy that is confined within one wavelength of the surface and with amplitude that decays exponentially with distance below the surface. In contrast with bulk waves, acoustic waves propagate in solid plates with two plane boundaries are much more complex. In 1917, Horace Lamb gave analysis and descriptions of this type of acoustic waves, called Lamb waves[10]. The applications of acoustic waves such as seismology, sonar, and non-destructive evaluation have been known for a long period. Owing to the intense development interest in exploring new piezoelectric materials and the use of interdigital transducers invented by White and Voltmer[11], a large number of microsensors based on BAW, SAW, Lamb waves are developed.

When using acoustic devices as sensors, several crucial detection mechanisms are needed to be clarified first. Typically, these important detection mechanisms include mass loading, elastic and viscoelastic effect, and acoustoelectric (AE) interaction[3]. Mass loading is the response resulting from the changes in the mass density, defined as mass per unit area, on the propagating surface[3]. The sensing targets, which are strongly bound to the sensor surface, move synchronously with the surface displacement and cause additional contributions to velocity change of acoustic waves. Viscoelastic loading usually applies on evaluating properties of a finite film whose thickness is no longer negligible. Energy storage and power dissipation resulting form acoustic waves-induced film deformation lead to velocity change and attenuation of acoustic wave sensors. AE interaction occurs in a piezoelectric semiconducting material or in composite structures of piezoelectric dielectrics and semiconductors.[12] The interaction between the electric field accompanying the propagating acoustic waves and mobile charges in semiconductors results in a velocity change and attenuation.[13]

Among detection mechanisms listed above, mass loading is the one most used for acoustic wave sensor applications, yet it is the simplest and the mature one. In recent years, the AE effect has been utilized in a variety of sensors, such gas sensors[14-19] and photodetectors[20-29]. However, most of sensors were based on surface waves. In addition, analysis of the influence of AE effect on Lamb waves in piezoelectric semiconductors is complex and only a few Lamb wave sensors using the AE effect are realized and discussed[30,31]. In this regard, this study focuses on the analysis and realization of acoustic wave microsensors using the acoustoelectric effect. The influence of AE effect on acoustic waves in piezoelectric semiconducting materials is introduced first. An approximate AE model applied to surface waves in half-space piezoelectric semiconductors and composite structures of piezoelectric dielectrics and semiconductors are studied. Next, when

discussing the Lamb wave propagation affected by the AE effect, the dispersion relation is taken into account. An analysis of a modified AE model applied to Lamb waves by introducing dispersion relations is given. Finally, surface and Lamb wave microsensors using the AE effect will be realized and compared with the theoretical AE model.

1.2 Literature Review

The phenomenon "acoustoelectric effect" was named and discussed first by Parmenter in 1953[32]. Parmenter pointed out that the presence of a travelling acoustic wave in a conducting medium gives rise to an electric field, which travels through the medium with the same velocity as that of the acoustic wave. The electrons being trapped by the moving electric field give rise to a net electric current. Such a generation of an electric current by an acoustic wave is called the acoustoelectric effect. Several follow-up studies[33-35] gave theoretical calculations of the acoustoelectric effect, however, these researches focused on metals. Based on numerical estimation, Van Den Beukel[36] in 1956 demonstrated that the acoustoelectric effect was difficult to realized experimentally in a metal, while for a semiconductor the effect is much easier to be observed. In the same year, Weinreich[37] gave a theoretical treatment of the acoustoelectric effect by application of a dc field in a nonpiezoelectric semiconductor. However, in 1959, Weinreich et al.[38] realized an experiment of the acoustoelectric effect in n-type germanium, and the results showed that the absolute values of acoustic wave attenuation were all quite small, which means that the acoustoelectric effect in a nonpiezoelectric semiconductor is hard to be observed.

Since the piezoelectric effect has been discovered in some semiconducting materials such as cadmium sulfide (CdS) and zinc oxide (ZnO)[39,40], elastic wave propagation in piezoelectric semiconductors were able to be discussed. In 1962, Wang[41] indicated that in the semiconductors which are also piezoelectric, the coupling between acoustic waves and

conduction electrons is much stronger than that in semiconductors. The theory of velocity change and attenuation of acoustic waves interacting with free carriers in piezoelectric semiconductors has been worked out by Hutson and White[13] in 1962. They considered a one-dimensional model for bulk acoustic wave propagation and dealt with nondrifting carriers in piezoelectric semiconducting medium. In the study, they found maximum interaction occurs when the conduction current due to the acoustic fields was of the same order of magnitude as the displacement current. Blotekjaer and Quate[42] proposed another approach, called the coupled modes, to analyze the interaction of bulk waves and drifting carriers in piezoelectric semiconductors in 1964.

In 1970, Ingebrigtsen[12] analyzed the interaction of surface acoustic waves and free carriers in a piezoelectric coated with a semiconducting film. In this research, Ingebrigtsen investigated linear and nonlinear attenuation of surface waves. The change of velocity due to the acoustoelectric effect was not discussed. Wixforth et al.[43] in 1989 gave an approximation of the acoustoelectric effect in a SAW device, which was based on the theory developed by Hutson and White[13]. Utilizing two models, which were developed by Hutson and White[13] and Adler[44] respectively, Wixforth pointed out that the velocity change and attenuation of SAW due to acoustoelectric effect are dependent on conductivities of the materials but not frequency. The formulas proposed by Wixforth et al. are the most common adopted approximation model of acoustoelectric effect for surface waves so far. A number of studies analyzed the amplification of SAW due to the acoustoelectric effect[45-48], and some studies focused on transversal[49-52] and nonlinear[53,54] acoustoelectric effect, however, are not parts of discussions in this dissertation.

Exact analysis of velocity change and attenuation due to acoustoelectric effect of surface waves is complex, and an approximation model developed by Wixforth et al. has been widely adopted. Likewise, the analysis of influences of AE effect on Lamb wave

propagation is much more complex thus lack of developed theories and models. In 1988, Niemczyk et al.[55] investigated the acoustoelectric interaction between acoustic plate mode (APM) devices and solutions contacting the surface of the plate device. Acoustic plate waves propagating in a piezoelectric generate an evanescent RF electric field. This electric field extends into the adjacent liquid and couples to the permanent or induced ions (or dipoles) in the liquid which leads to velocity perturbation and attenuation of the APM. Niemczyk et al. analyzed the acoustoelectric interaction of APM by developing an equivalent circuit model, and a designed experiment gave agreement with the constructed model. In 1998, Yang and Shue[56] discussed the leaky Lamb wave propagation characteristics in a piezoelectric plate immersed in a conductive fluid. Based on partial wave analysis, they established a theoretical model to simulate the influence of fluid conductivity on the velocity shift of leaky Lamb waves. Lee and Kuo[57] in 2006 also gave an analysis of the interaction between conducting fluid and leaky Lamb waves based on partial wave analysis. They not only can simulate the velocity shift but also attenuation properties of leaky Lamb waves propagating in a conductive fluid. However, these models are only suitable for designing liquid Lamb wave sensors. The acoustoelectric models for other types of Lamb wave sensors are not completely given. In 2004, Yang et al.[58] analyzed the dispersion and dissipation as well as amplification of acoustic waves due to AE effect in a special laminated piezoelectric semiconductor plate consisting of silicon and PZT-5H. In brief, a generalized AE model for Lamb wave propagation has not been given so far.

Experimental verifications of the AE effect have been accomplished since the theories associated AE interactions were developed. In the early stage, the experimental measurements focused on the amplification of acoustic waves[47,59] by applied an voltage on piezoelectric semiconductors. In 1982, Urabe[60] demonstrated a frequency variable SAW oscillator based on ZnO/SiO_2/Si structure by adjusting the applied voltage. In 2000, Rotter

et al.[61] presented a voltage-controlled SAW oscillator which using the interaction between SAW and a semiconductor quantum well structure. Zhu et al.[62] showed a voltage tunable SAW phase shifter using multilayer ZnO grown on a r-sapphire substrate in 2006. In 2007, Saddik et al.[63] presented a dc electric field tunable BAW resonator using $SrTiO_3$. Except for the voltage controlled acoustoelectric interaction, several studies[64-66] discuss the interaction between acoustic waves and light in piezoelectric semiconductor heterostructures. Furthermore, Reulet et al.[67] reported observations of AE effect in carbon nanotubes (CNTs) in 2000. Ebbecke et al.[68] observed acoustoelectric current transport through single-walled carbon nanotubes (SWCNTs). Talyanskii et al. demonstrated several new devices such as acoustoelectric Y-branch switch[69] in 2006 and acoustoelectric single photon detector[70] in 2007. These researches indicate that exploring more novel applications using acoustoelectric effect can be expected in the future.

As well as the experimental observations mentioned above, microsensors using acoustoelectric effect have also attracted much attention. Since the first of the acoustic sensors, the so-called quartz crystal microbalance (QCM), was realized, acoustic wave devices have been used for various sensing applications for over 50 years. In 1985, the first SAW gas sensor based on changes in conductivity of a thin surface film was reported by Ricco et al.[14]. The conductivity of the PbPc sensing film increased when reacting with NO_2. Acoustoelectric coupling in the sensing film thus slowed the SAW velocity and changed the oscillation frequency of the gas sensor. In 1986, Vetelino et al.[71] designed and tested a hydrogen sulfide (H_2S) SAW gas detector using a semiconducting thin film deposited on a $LiNbO_3$ substrate. Penza and Vasanelli[16] fabricated a SAW NOx gas sensor by adopting a semiconducting WO_3 film in 1997. In 2000, Giriuniene and Garska[17] studied acoustoelectric interaction between SAW and tin oxide semiconducting film in a temperature interval from 20℃ to 140℃, where several gas targets were also tested and

discussed. In 2005, Jakubik[72] developed a SAW hydrogen gas sensor based on a semiconductor-metal bi-layer deposited on a piezoelectric substrate. In 2006, Ippolito et al.[18] presented a layered WO_3/ZnO/$LiTaO_3$ SAW sensor for ethanol sensing. In 2009, Huang et al.[73] proposed a SAW hydrogen sensor with Pt coated ZnO nanorod, which can work at room temperature.

Semiconductors such as ZnO, GaN, AlN and their alloys are suitable for near-visible and ultraviolet (UV) range optical sensing applications due to the wide band gap energy[20,74]. Acoustic wave propagation in these semiconductors makes the acoustic wave-based devices attractive for optical sensing applications. One of the first studies on the UV detectors based on SAW devices was demonstrated by Ciplys et al.[20] in 2002. The UV photoresponse of a GaN-based SAW oscillator was discussed. Ciplys et al. also studied the AlGaN-based SAW photoresponses in UV[75] and deep-UV[76] range, respectively. In 2003, Sharma[22] revealed a UV detector using a semiconducting ZnO film deposited on piezoelectric $LiNbO_3$ substrate. In 2004, Emanetoglu et al.[77] demonstrated a UV sensor fabricated with ZnO/Mg:ZnO/ZnO multilayers on r-plane sapphire SAW device. In 2007, Kumar et al.[78] fabricated a UV detector on a ZnO/quartz SAW device. In 2008, Ma et al.[79] fabricated an UV array photodetector by the application of ZnO/LiNbO3 SAW device using slanted finger interdigital transducers as electrodes. However, most of the presented cases used semiconductor films as the sensing material. Moreover, only a few studies compared the photoresponse with the theoretical AE model. Therefore, one of objectives in this dissertation is to discuss the relation between the SAW microsensor response and the developed AE model by designing and realizing a novel ZnO nanorod-based UV detector.

Some acoustic microsensors based on quartz crystal resonators[80] and SH-SAW devices[30] used for liquid sensing applications utilizing AE interaction are also reported. In 1998 and 2006, Yang and Shue[56] and Lee and Kuo[57] discussed Lamb wave of a

piezoelectric plate interaction with conducting fluid, respectively. As can be seen, Lamb wave sensors which use AE effect were restricted in liquid sensing. In 2006, Duhamel et al.[81] demonstrated a thin AlN membrane with 2μm thick for liquid sensing using mass loading effect. In 2008, Yu and Lin[82] reported a composite PZT/SiNx thin film Lamb wave device which can be used in liquid density sensing and biosensing. These studies show that the Lamb wave devices with ultra thin-film have excellent sensitivities which are even better than SAW microsensors. In 2008, Yamamoto et al.[83] fabricated a Lamb wave hydrogen gas sensors based on $LiNbO_3$ substrate. This indicates that the Lamb wave sensors using AE effect apply not only to liquid sensing but other sensing target such as gas and light are worth discussed and studied. Therefore, main objective of this dissertation is to develop an AE model applied to Lamb wave propagation in a piezoelectric semiconducting material, design a silicon-based ultra-thin semiconducting film Lamb wave UV sensor and discuss the properties of this sensor which can be further used in other sensing applications.

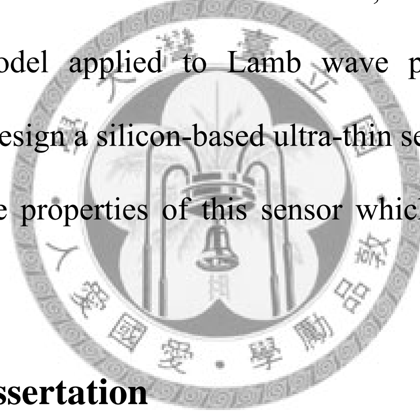

1.3 Outline of the Dissertation

This study is divided into five chapters. Chapter 1 states the motivation of this research and gives development and publications of microsensors which mainly focus on acoustic wave-based sensors utilizing acoustoelectric effect.

Chapter 2 gives characteristics of surface wave and Lamb wave propagations affected by AE interactions. First, an AE model for acoustic wave propagation in an unbounded piezoelectric semiconductor is briefly introduced. Then, a model for surface wave propagation associated with AE interaction is described. Surface wave propagating properties such as velocity shift and attenuation resulting form acoustoelectric effect are studied. By taking the dispersion relation into account, a modified AE model is constructed

and can be apply to Lamb wave propagation in piezoelectric semiconducting materials.

To experimentally verify the AE effect in a SAW microsensor, a novel SAW-based UV detector with ZnO nanorod sensing material is designed, realized and measured in Chapter 3. First, a two-port SAW oscillator on a 128∘YX-$LiNbO_3$ substrate in fabricated. Then, a ZnO nanorod used as a sensing material is grown on the substrate. By combining the SAW oscillators and ZnO nanorod, a UV detector based on a dual delay line SAW oscillator system is constructed. The characteristics of the UV detector such as real-time response, sensitivity, repeatability and stability are measured. Furthermore, by substituting the measured frequency shifts into the AE model, ZnO conductivities are derived and discussed.

Chapter 4, also the last part of the main body of this dissertation, a novel silicon-based ZnO-membrane Lamb wave microsensor is discussed. A Lamb wave sensor is designed on the basis of numerical simulation and fabricated using MEMS technology. Two types of Lamb wave microsensors, which consist of $ZnO/Si_3N_4/Si$ and ZnO/Si_3N_4 respectively, are realized and discussed. A Lamb wave UV sensing system is constructed. Measurements of Lamb wave UV detectors are then proposed for the first time.

Finally, Chapter 5 concludes this study and proposes some prospects of acoustic microsensors using acoustoelectric interaction.

Chapter 2 Acoustoelectric Effect in Piezoelectric Semiconductors

This chapter analyzes the propagation of acoustic waves in piezoelectric semiconductor materials. The acoustoelectric effect means the interactions between travelling acoustic waves and mobile charges in piezoelectric semiconductors. First, acoustic wave propagation in an unbounded piezoelectric semiconductor is introduced in Sec.2.1. Sec. 2.2 gives a model applied to the interactions of surface waves and mobile charges. Sec 2.3 proposes a modified acoustoelectric-effect model for Lamb wave propagations in piezoelectric semiconductor plates and some numerical examples are calculated. In Sec 2.4, temperature effect on acoustoelectric effect is briefly introduced.

2.1 Acoustoelectric Effect in a Piezoelectric Semiconductor

Elastic wave propagation in piezoelectric media has been analyzed and used for various applications for decades. When discussing wave propagation in a piezoelectric, the piezoelectric material is assumed as an insulator. If the medium is piezoelectric and also semiconducting, which is called piezoelectric semiconductor (PS), characteristics of wave propagation differs from those in a piezoelectric insulator (PI). Acoustoelectric (AE) effect arises from the interaction of acoustic waves and mobile carriers in a PS. This section briefly introduces elastic wave propagation affected by AE interactions in an unbounded PS. The detailed derivation is given in Appendix A.

For acoustic wave propagation in a PS, the equation of motion from Newton's law with neglecting the body force are given by

$$\tau_{ij,j} = \rho \ddot{u}_i \tag{2.1}$$

where τ_{ij} is the stress field, ρ is the mass density , and the mechanical displacement of an arbitrary point with position $\mathbf{r} = (x_1, x_2, x_3)$, varying with time t, can be denoted as $u_i(\mathbf{r}, t)$.

Under quasi-static approximation, the generalized constitutive relations[84] in index notation are

$$\tau_{ij} = C_{ijkl}u_{k,l} + e_{lij}\phi_{,l} \quad (2.2)$$

$$D_i = e_{ikl}u_{k,l} - \varepsilon_{il}\phi_{,l} \quad (2.3)$$

where D_i is the electric displacement field, ϕ is electric potential, and C_{ijkl}, e_{lij}, and ε_{il} are elastic stiffness constants, piezoelectric constants, and permittivity, respectively.

To solve the wave equation, the effect of mobile carriers must be taken into account. Poisson's equation, equivalent to Gauss' law for the electric field, is

$$D_{i,i} = -qn_s \quad (2.4)$$

where the right hand side represents the volume density of free charge. (coulomb per meter cubed). q is the magnitude of the electronic charge and n_s is the number of electrons per unit volume required to produce the free charge. The continuity equation, also known as the law of conservation of charge, is given by

$$J_{i,i} = q\dot{n}_s \quad (2.5)$$

where J_i is the volume current density, or simply called current density (amperes per meter square).

To simplify the model, only an n type of extrinsic semiconductor is considered [13]. The current density for such type of material can be expressed as

$$J_i = -q(n + fn_s)\mu_{ij}\phi_{,j} + \frac{f}{\beta}\mu_{ij}n_{s,j} \quad (2.6)$$

where n is the mean current density, f is the fraction of the acoustically produced space charge which is mobile, μ_{ij} is the electron mobility, and $\beta = (\mathrm{k}T)^{-1}$ is the constant related to Boltzmann's constant k and temperature T.

Eq. (2.1) to (2.6) are the equations for elastic waves propagating in a PS. Consider plane wave solutions be proportional to a complex wave function $\exp[i(\omega t - k\hat{\ell}\bullet\mathbf{r})]$, where ω is the circular frequency, k is the wave number, $\hat{\ell} = \ell_x\hat{x} + \ell_y\hat{y} + \ell_z\hat{z}$ represents a unit vector in the propagation direction, and $\mathbf{r}=(x, y, z)$ is the position vector. After some rearrangement of terms, we have

$$\rho\omega^2 u_i = k^2 \bar{C}_{ijkl} u_k \tag{2.7}$$

where $\bar{C}_{ijkl}$ is the complex elastic constant, given as

$$\bar{C}_{ijkl} = \ell_l C_{ijkl} \ell_j + \frac{i\omega \ell_r e_{ris} \ell_s \ell_l e_{pkl} \ell_p + k^2 \dfrac{f \ell_i \mu_{ij} \ell_j}{q\beta} \ell_l e_{pkl} \ell_p \ell_r e_{ris} \ell_s}{i\omega \ell_p \varepsilon_{pl} \ell_l + k^2 \dfrac{f \ell_j \mu_{ij} \ell_i}{q\beta} \ell_p \varepsilon_{pl} \ell_l + qn \ell_j \mu_{ij} \ell_i} \tag{2.8}$$

If acoustic waves propagate along the x-direction, the complex elastic constant is

$$\bar{C} = C\left\{1 + \frac{e^2}{C\varepsilon}\left[\frac{1 + i(\omega_C/\omega)}{1 + (\omega_C/\omega)^2}\right]\right\} \tag{2.9}$$

where $\omega_C = \sigma/\varepsilon$, defined as a conductivity frequency and also called relaxation frequency, is the ratio between a homogeneous bulk conductivity σ and permittivity ε. As can be seen, if the conductivity is small and can be neglected, the complex elastic constant can be reduced as the one in a PI. To explain the physical meaning of ω_C, one should start with the inverse of ω_C, i.e., the dielectric relaxation time. The dielectric relaxation time is the time for charge becoming neutralized again in conduction process. In other words, it is the time for an electron system relaxes from a perturbation, for example, an external electric

field, into its equilibrium distribution[43]. In metals, the dielectric relaxation time is small while in semiconductors and insulators it can be large. Thus, high conductivity frequency ω_C which equals to short dielectric relaxation time indicates that the conductivity is large.

Notably, in Eq. (2.9), the material constants have dropped the subscript for convenience and been calculated by a coordinate transformation to ensure the wave propagation is along the crystallographic x direction. The details of coordinate transformation are described in Appendix B. Furthermore, Eq. (2.9) implicitly states that the diffusion effect is neglected[13]. Usually, at room temperature, the acoustoelectric effect due to diffusion effect can be neglected, thus is not considered in this research. The effect of diffusion is discussed in Appendix A.

Using the complex elastic constant in Eq. (2.9), one can obtain acoustic propagating properties of a PS. Velocity and absorption constants in terms of $\bar{C}$ [13] are

$$v = v_0 \operatorname{Re}(\bar{C}/C)^{1/2},\ v_0 = (C/\rho)^{1/2} \tag{2.10}$$

$$\Gamma = \frac{\omega}{v_0} C^{1/2} \operatorname{Im}\left(\bar{C}^{-1/2}\right) \tag{2.11}$$

Where $v_0 = (C/\rho)^{1/2}$ is an acoustic velocity in a nonpiezoelectric insulator. Since $e^2/C\varepsilon = K^2/(1-K^2) \cong K^2$ is small ($K^2 \ll 1$), where K^2 is the electromechanical coupling coefficient, one have

$$v = v_0 \left\{ 1 + \frac{K^2/2}{1+\left(\omega_C/\omega\right)^2} \right\} \tag{2.12}$$

$$\Gamma = \frac{\omega}{v_0} \frac{K^2}{2} \left[\frac{\left(\omega_C/\omega\right)}{1+\left(\omega_C/\omega\right)^2} \right] \tag{2.13}$$

Eq. (2.12) and (2.13) illustrates velocity dispersion and loss influenced by acoustoelectric effect in a PS which acoustic waves propagate in. A numerical example is shown in Fig.

2.1. The x axis is the ratio of acoustic circular frequency ω and ω_C. The vertical axis on the left side represents acoustic loss, in the form of the acoustic loss over ω/v_0 in units of $K^2/2$. On the right side, the vertical axis indicates acoustic velocity variation in terms of $v-v_0/v_\infty-v_0$, where $v_\infty=v_0\left(1+e^2/2C\varepsilon\right)$ is the acoustic velocity in a PI.

In Fig. 2.1, the velocity variation shows that the value goes from v_0 to v_∞. When acoustic frequencies are very low, the velocity is equal to v_0; while at high frequencies, the velocity is v_∞. Acoustic loss approaches to zero at very high or low frequencies. For example, when ω is much lower than ω_C, the conductivity is large that the carriers can screen the piezoelectric field, thus the velocity is equal to v_0. On the contrary, when $\omega \gg \omega_C$, the conductivity is relatively small that the material act as an insulator and the velocity is v_∞.The maximum acoustic loss occurs at $\omega=\omega_C$, and the term $\Gamma v_0/\omega$ which is associated with acoustic loss has a maximum value of $K^2/4$, as the triangle indicated in Fig. 2.1. The velocity $v=v_0+v_\infty/2$ occurs at $\omega=\omega_C$, as the red circle shown in the figure. As can be seen in Fig. 2.1, acoustic loss and the slope of velocity change is largest at frequencies around $\omega=\omega_C$, which indicates that the acoustoelectric interaction is strong around $\omega=\omega_C$; while at high or low frequencies, the acoustoelectric effect are not obvious.

In this section, the influence of AE interaction on acoustic wave propagations in an unbounded PS which does not consider boundary conditions is discussed. Parameters which dominate the changes of acoustic velocity and loss are the electromechanical coupling coefficient K^2 and conductivity frequency ω_C associated with the conductivity.

2.2 Influences of Acoustoelectric Effect on Surface Acoustic Wave Propagations

Exact analysis of velocity change and attenuation of surface waves due to AE effect is complex. In this section, SAW propagations affected by AE effect in different structures are discussed. First, the coupling coefficient of surface waves is derived. Then, SAW propagating in a piezoelectric half-space with an ultra-thin semiconducting film is introduced. Finally, SAW propagation influenced by AE interactions in a piezoelectric semiconductor is given.

2.2.1 Electromechanical Coupling Coefficient

Sec. 2.1 demonstrates that the electromechanical coupling coefficient K^2 is one of the parameters which dominate acoustic velocity shift and loss resulting from AE interactions. Electromechanical coupling coefficient is a measure of the conversion efficiency between electrical energy and acoustic energy in piezoelectric materials, which means

$$K^2 = \frac{\text{stored mechanical energy}}{\text{supplied electrical energy}} \tag{2.14}$$

The coupling coefficient directly influences the insertion loss of acoustic wave devices, thus it is a crucial parameter while choosing the piezoelectric material for further applications. For bulk waves, the coupling coefficient is defined as $K^2 \simeq e^2/C\varepsilon$. For surface waves, the coupling coefficient differs slightly from that of bulk waves and is defined as [85]

$$K_{eff}^2 = 2\Gamma_S \varepsilon_S^{(\infty)} \tag{2.15}$$

Where $\varepsilon_S^{(\infty)}$ is the effective permittivity at infinite slowness, and the function Γ_S is a coupling parameter, which can be exactly calculated using the following equation [86]

$$\frac{1}{\Gamma_S} = -\beta \left[\frac{d\varepsilon_S(k_x)}{dk_x} \right]_\beta \tag{2.16}$$

Where k_x is the wave number when the wave propagates in the x direction. When the substrate in which surface waves propagate is a free piezoelectric half-space, $\beta = k_x$. If the substrate is a layered structure, β is a function of frequency, which means

$$\beta_l(f) = \frac{2\pi f}{v(f)} \tag{2.17}$$

where $v(f)$ represents the velocity dispersion on a free surface.

Another common-used calculation of coupling coefficients is also base on Eq. (2.15), however, the value of Γ_S is not exactly evaluated by using Eq. (2.16) but calculated by adopting Ingebrigtsen's approximation[86]. After applying Ingebrigtsen's approximation, the formula for coupling coefficient can be rewritten as

$$K_{eff}^2 \cong \frac{v_o^2 - v_m^2}{v_o^2} = \frac{2(v_o - v_m)}{v_o} = \frac{2\Delta v}{v_o} \tag{2.18}$$

where v_o and v_m are SAW phase velocities on free surface and metalized surface respectively. It is noted that this approximation is valid only for Rayleigh waves. Moreover, in reality, v_m is the velocity of SAW which propagates on a highly-conducting metal film deposited on a piezoelectric surface. This indicates that the metal film removes all longitudinal electric fields along the surface, but does not short-circuit the field in the interior like what the homogeneous conductivity of the bulk material does. Therefore, in the same material, K_{eff}^2 for surface waves is slightly smaller than K^2 for bulk waves.

Chen[87] has concluded that for SAW propagating in piezoelectric material, especially in a layered structure such as ZnO/diamond, coupling coefficient derived by using Eq. (2.15) and measured values match more well than those calculated by using Eq. (2.18). In

this study, coupling coefficients of different cases discussed in the following are exactly derived by using Eq. (2.15).

2.2.2 Characteristics of Surface Acoustic Wave Propagation Affected by Acoustoelectric Effect

From section 2.1, in an unbounded PS, velocity change and attenuation of acoustic waves due to AE interaction which neglects diffusion effect can be rewritten as

$$\frac{\Delta v}{v_0}=\frac{K^2}{2}\frac{1}{1+\left(\omega_C/\omega\right)^2} \tag{2.19}$$

$$\frac{\Gamma}{\omega/v_0}=\frac{K^2}{2}\frac{\omega_C/\omega}{1+\left(\omega_C/\omega\right)^2} \tag{2.20}$$

For surface waves, exact analysis of velocity change and attenuation due to acoustoelectric effect is complex. Parameters such as coupling coefficient and conductivity frequency are no longer the same with those calculated for bulk waves because of boundary conditions of the medium where surface waves propagate. In the following, surface wave propagations affected by AE interactions in different structures are introduced.

(1) A semiconducting material which is adjacent to a piezoelectric:

First, consider two half-spaces where a semiconductor material is near the surface of a PI, as shown in Fig. 2.2. In this case, a spatially periodic potential is applied along the boundary of these two materials. Surface waves propagating on the surface of the PI are affected by the carriers moving in the semiconducting material which is parallel and very closely adjacent to the PI. Because permittivity is uniform in each of these two half-spaces which are homogeneous, the upper and lower displacement currents are symmetrical, which means the corresponding capacities can be considered in parallel[44]. Thus, the relaxation time can be given as a value of $\left(\varepsilon_S+\varepsilon_P\right)/\sigma$ [44], which indicates that

$$\omega_C = \frac{\sigma}{\varepsilon_S + \varepsilon_P} \tag{2.21}$$

where σ and ε_S are the conductivity and permittivity of the semiconductor; ε_P is the permittivity of the PI.

Therefore, the SAW velocity change and loss can be written as

$$\frac{\Delta v}{v_o} = \frac{K_{eff}^2}{2} \frac{1}{1+(\omega_C/\omega)^2} \tag{2.22}$$

$$\frac{\Gamma}{\omega/v_o} = \frac{K_{eff}^2}{2} \frac{\omega_C/\omega}{1+(\omega_C/\omega)^2} \tag{2.23}$$

where K_{eff}^2 and ω_C can be derived form Eq. (2.15) and Eq. (2.21), respectively.

(2) A piezoelectric beneath a thin sheet of mobile carriers

Now, consider a PI with a thin semiconducting layer located directly on the top surface of the PI, as Fig. 2.3 shows. Mechanical contact of these two materials which causes mechanical effects is neglected. Assume the thickness d of the thin semiconducting layer is much smaller than the SAW wavelength.

To find the conductivity frequency of this structure, one should begin with the relaxation time of the semiconducting film. Consider the upper half-space of the structure in Fig. 2.3, the potential field ϕ must satisfy the Laplace equation, $\nabla^2\phi = 0$, which means $\phi \sim e^{-k_x z}$. Moreover, the potential field is zero when $z = +\infty$. Thus the normal component of the electrical displacement is

$$D_z\big|_{z=0^+} = -\varepsilon_0 \phi_{,z}\big|_{z=0^+} = \varepsilon_0 k_x \phi\big|_{z=0^+} \tag{2.24}$$

ε_0 is the permittivity in vacuum and k_x is the acoustic wave number.

The surface current density in the thin film is given as

$$J_S = J_x d = \sigma E_x d = -(\sigma d)\phi_{,x} \tag{2.25}$$

where J_x is the current density mentioned in Eq. (2.5),

Substitute Eq.(2.25) into $J_{S x,x} = -\dot{D}_z$ at $z = 0$, on can get

$$-(\sigma d)\phi_{,xx} = -\varepsilon_0 k_x \dot{\phi} \tag{2.26}$$

where

$$\phi_{,xx} = -k_x^2 \phi \quad , \quad \phi \sim e^{-k_x z} \tag{2.27}$$

Therefore, Eq. (2.26) can be rewritten as

$$(\sigma d) k_x^2 \phi = -\varepsilon_0 k_x \dot{\phi} \tag{2.28}$$

Assume the electric potential with a time constant which represents exponential decay is

$$\phi = \phi_0 e^{-t/\tau_C} \tag{2.29}$$

which implies that $\dot{\phi} = -\phi/\tau_C$. Then Eq. (2.28) can be rearranged as

$$\tau_C = \frac{\varepsilon_0}{(\sigma d) k_x} \tag{2.30}$$

Eq. (2.30) represents the relaxation time in terms of conductivity and wave number. If further consider the upper (vacuum) and lower (PI with a thin sheet of mobile carriers) half-spaces as two condensers which are in parallel, the relaxation time of this structure will be [44]

$$\tau_C = \frac{\varepsilon_0 + \varepsilon_P}{(\sigma d) k_x} \tag{2.31}$$

Notably, the term σd is in fact the sheet conductivity of the semiconducting film which carries the induced currents, and the unit is Ω^{-1}. Define this sheet conductivity as $\sigma_d = \sigma d$, the conductivity frequency of the structure shown in Fig. 2.3 is thus

$$\omega_C = \frac{\sigma_d k_x}{\varepsilon_0 + \varepsilon_P} \tag{2.32}$$

Define a material constant[43]

$$\sigma_m = v_o\left(\varepsilon_0 + \varepsilon_P\right) \tag{2.33}$$

where v_o is SAW phase velocity on a free surface of the PI. By substituting Eq. (2.32) and Eq. (2.33) into Eq. (2.22) and Eq. (2.23), the velocity change and acoustic attenuation of surface waves in a piezoelectric insulator coated with an ultra-thin semiconducting film are[43]

$$\frac{\Delta v}{v_o} = \frac{K_{eff}^2}{2}\frac{1}{1+\left(\sigma_d/\sigma_m\right)^2} \tag{2.34}$$

$$\frac{\Gamma}{k_x} = \frac{K_{eff}^2}{2}\frac{\sigma_d/\sigma_m}{1+\left(\sigma_d/\sigma_m\right)^2} \tag{2.35}$$

These two equations developed by Adler and Wixforth are the most common-used formulas for surface wave propagation influenced by AE interaction. In Eq. (2.34), $\Delta v = v - v_m$ means the difference between the velocity under AE interaction and the velocity when the conductivity of the surface is infinity (short condition). The main difference of Eq. (2.34) and Eq. (2.35) compared with those discussed in Sec. 2.1 and the section (1) is that the frequency-independent ratio σ_d/σ_m replaces the ratio ω_C/ω in the equations. In other words, the velocity change and attenuation are independent of frequency but dependent of sheet conductivity of the semiconducting material.

Fig. 2.4 is the velocity change and loss versus sheet conductivity of a structure with an ultra-thin semiconducting film located on a 128°YX-$LiNbO_3$ substrate. The left side of *y* axis represents the value of velocity change, while the right side of *y* axis indicates the attenuation constants. When the sheet conductivity is very small, $\sigma_d \to 0$, which means the boundary condition of the surface is open, a maximum velocity change is $\Delta v/v_o = K_{eff}^2/2 = 2.7\%$ in 128°YX-$LiNbO_3$. On the contrary, when the sheet conductivity

is so large that the surface is just like metalized, the velocity change approaches to zero. The slope of the velocity change under AE interaction is large when σ_d is around σ_m. For attenuation, the numerical calculation shows that when the sheet conductivity is rather too small or too large, there is no SAW attenuation due to AE interaction. The maximum attenuation occurs at $\sigma_d = \sigma_m$, as the star sign marked in Fig. 2.4 and is a value of $K_{eff}^2 / 4$. In this case, $\sigma_m = 1.907 \times 10^{-6} \Omega^{-1}$.

(3) A piezoelectric semiconductor:

AE interaction of SAW on a piezoelectric substrate coated with a thin semiconducting film is discussed in section (2). In that case, the semiconducting film and the piezoelectric beneath it are treated as one material; therefore, the material constants such as SAW velocities of free or short boundary conditions, coupling coefficient and permittivity all adopt those of the piezoelectric except for the sheet conductivity which comes from the semiconducting thin film.

If we further consider a piezoelectric semiconductor in which SAW propagates, as schematically shown in Fig. 2.5. Acoustic energy of surface waves decays as the depth increases, which means the energy is confined on the surface. Therefore, the effective region where acoustoelectric effect takes place can be regarded as the grey region marked in Fig. 2.5, and the situation is similar to the case (2). SAW velocity change and attenuation in a piezoelectric semiconductor can thus be described by Eq. (2.34) and Eq. (2.35). Fig. 2.6 shows the percentage of SAW velocity change due to AE interactions in a ZnO half-space. SAW propagation in this example is perpendicular to the C-axis of the ZnO. K_{eff}^2 of ZnO calculated by using Eq. (2.15) is 0.96%. As can be seen, the percentage of velocity change decreases when the sheet conductivity of ZnO increases and the curve is similar to that in Fig. 2.4. Moreover, the reason that percentages of SAW velocity shifts are

smaller than the case (2) results from smaller K_{eff}^2 of ZnO compared with $LiNbO_3$. Fig. 2.7 is the SAW attenuation of ZnO resulting from AE interactions. The maximum loss over wave factor is smaller than 0.0025.

2.3 A Modified Acoustoelectric-Effect Model for Lamb Wave Propagation in Piezoelectric Semiconductors

In previous sections, elastic wave propagations in a piezoelectric semiconductor affected by AE interactions are derived. In the structures discussed above, there is no dispersion in wave velocity and coupling coefficient. Nevertheless, when a plate with a thickness which is comparable to wavelength, Lamb wave modes exist and propagate in the plate so that phase velocity dispersion occurs. Therefore, when discussing the influence of AE interaction on Lamb wave propagations, dispersion relations must be taken into account. In this section, a transfer matrix method is employed to calculate the phase velocity dispersion of Lamb wave modes first. Then, a modified AE model applied to Lamb wave propagation in a piezoelectric semiconductor plate which includes the dispersion relation is constructed. Finally, AE effect in a multi-layered plate with dispersion is discussed.

2.3.1 Dispersion of Lamb Waves in a Single/Layered Structure

Surface wave propagation in a layered structure which consists of piezoelectric and/or nonpiezoelectric has been analyzed based on transfer matrix by Honein et al. in 1991[88] and Wu and Chen in 2002[89]. Here, Lamb wave velocity dispersion and coupling coefficient adopting the transfer matrix method developed by Chen[90] which can be applied on Lamb wave modes are introduced and derived. The general layered-plate structure is shown in Fig. 2.8.

In a piezoelectric insulator, the governing equations are $\tau_{ij,j} = \rho \ddot{u}_i$ and $D_{i,i} = 0$.

The constitutive equations are $\tau_{ij} = C_{ijkl}u_{k,l} + e_{lij}\phi_{,l}$ and $D_i = e_{ikl}u_{k,l} - \varepsilon_{il}\phi_{,l}$. Honein et al. [88] demonstrated that these four equations can be written in the form

$$\partial_z \boldsymbol{\xi} = \mathbf{N}\boldsymbol{\xi} \tag{2.36}$$

where $\boldsymbol{\xi} = (\mathbf{u}, \phi, \mathbf{t}, D_z)^{\mathrm{T}}$ is the state vector consisting of the displacement vector $\mathbf{u}$, the traction vector $\mathbf{t}$, the electric displacement D_z and the electric potential ϕ; $\mathbf{N}$ is the fundamental acoustic tensor.

Consider plane harmonic waves propagation in the *x* direction, then

$$\mathbf{u}(x,z,t) = \hat{\mathbf{u}}(z)exp\{i(\omega t - k_x x)\} \tag{2.37}$$

$$D_z(x,z,t) = \hat{D}_z(z)exp\{i(\omega t - k_x x)\} \tag{2.38}$$

$$\mathbf{t}(x,z,t) = \hat{\mathbf{t}}(z)exp\{i(\omega t - k_x x)\} \tag{2.39}$$

$$\phi(x,z,t) = \hat{\phi}(z)exp\{i(\omega t - k_x x)\} \tag{2.40}$$

where ω is the radio frequency and k_x is the wave number in the x direction. Substituting Eq. (2.37) ~ (2.40) into Eq. (2.36), the differential equation system can be rewritten as

$$\partial_z \hat{\boldsymbol{\xi}}(z) = -i\hat{\mathbf{N}}(z) \cdot \hat{\boldsymbol{\xi}}(z) \tag{2.41}$$

where $\hat{\boldsymbol{\xi}}(z) = \left(\hat{\mathbf{u}}(z), \hat{\phi}(z), i\hat{\mathbf{t}}(z), i\hat{D}_z(z)\right)^{\mathrm{T}}$.

If the medium where waves propagate are homogeneous, the matrix $\mathbf{N}$ is determined by k_x, ω and material constants of the media; meanwhile, $\mathbf{N}$ is independent of the depth *z*, thus the solution of this differential equation can be given as

$$\hat{\boldsymbol{\xi}}(z) = e^{-i\hat{\mathbf{N}}z} \cdot \hat{\boldsymbol{\xi}}(0) \tag{2.42}$$

where the matrix $e^{-i\hat{\mathbf{N}}z}$ is the so-called transfer matrix and $\hat{\boldsymbol{\xi}}(0)$ represents the initial

condition at $z=0$. To get the general solution for a layered system shown in Fig. 2.8, the surface impedance approach is adopted[88]. The surface impedance tensor $\mathbf{G}$ which represents the ratio between the generalized traction vector $\mathbf{T}$ and the generalized displacement vector $\mathbf{U}$ is defined as

$$\mathbf{T} = i\omega \mathbf{G}\mathbf{U} \tag{2.43}$$

where $\mathbf{T} = \left\{ i\hat{\mathbf{t}}(z)\ \ i\hat{D}_z(z) \right\}^T$ and $\mathbf{U} = \left\{ \hat{\mathbf{u}}(z)\ \ \hat{\phi}(z) \right\}^T$. By applying boundary conditions and the continuity of the interface between each layer, the surface impedance of the down surface $\mathbf{G}_0$ can be derived, the following surface impedance of each layer can be calculated and the dispersion relations can thus be examined. Furthermore, the coupling coefficient of a piezoelectric plate in which the effect of electrode arrangements is concluded[90] can be exactly calculated by using Eq. (2.15).

In the following, two cases, dispersion relations of a single piezoelectric plate and a laminated plate, are discussed respectively.

(1) a single piezoelectric plate

First, consider a PI plate with a free down-surface, as shown in Fig. 2.9. The boundary conditions of this down surface at $z=0$ are traction free $t(0)=0$ and zero electrical displacement ($\mathrm{D_z}(0)=0$). Thus the surface impedance tensor $\mathbf{G}_0$ can be given as

$$\mathbf{G}_0 = \begin{bmatrix} 0 & 0 \\ 0 & -\varepsilon_0 k_x \end{bmatrix} \tag{2.44}$$

where ε_0 is the permittivity in vacuum and the Lapace equation $\nabla^2\phi = 0$ in the vacuum is satisfied.

The phase velocity dispersion of a single ZnO plate with free down surface is shown in Fig. 2.10. This is the velocity dispersion of the lowest antisymmetric mode, the A_0 mode,

of Lamb waves calculated by using the transfer matrix method. The horizontal axis is the product of frequency and the thickness of the ZnO plate. In this mode, the phase velocity is smaller than the surface waves in the same structure. Fig. 2.11 shows the coupling coefficient of the A_0 mode in a ZnO plate with free down surface. The figure shows that the coupling coefficient varies with different frequency and thickness of the ZnO plate, which differs from bulk and surface waves in a half-space material. Fig. 2.11 also indicate that the coupling coefficient of A_0 mode of a ZnO plate is larger than the one of surface wave, which reveal one of the advantage of using Lamb wave to realizing acoustic wave devices for further applications.

Next, consider a plate with metalized down surface, as Fig. 2.12 shows. In this structure, the boundary conditions at $z=0$ include traction free $t(0)=0$ and zero electric potential ($\phi(0)=0$). Therefore, the surface impedance tensor $\mathbf{G}_0$ of the down surface is

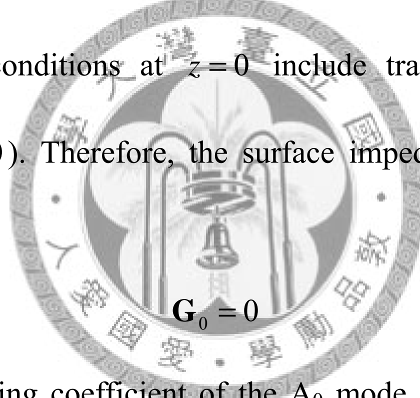

$$\mathbf{G}_0 = 0 \tag{2.45}$$

Fig. 2.13 shows the coupling coefficient of the A_0 mode in a ZnO plate with metalized down surface. The coupling coefficient becomes larger when the product of frequency and plate thickness increases from 0 to 1000.

(2) A laminated plate:

One of the main advantage of transfer matrix method is that it can deal with a layered structure consists of different materials. Herein an example of ZnO/silicon nitride (Si_3N_4)/silicon dioxide (SiO_2) laminated plate with free surfaces is employed to discuss characteristics of the velocity dispersion and coupling coefficient of Lamb waves. Thickness of ZnO is 0.5 μm, and those of Si_3N_4 and SiO_2 are both 0.2 μm.

Fig. 2.14 shows the phase velocity dispersion of the first three Lamb wave modes of a

$ZnO/Si_3N_4/SiO_2$ laminated plate with free surfaces. As can be seen in the plot, only the A_0 mode is the all-pass mode while the other two higher modes appear in larger frequency-thickness products. Thus, for a further design, a proper choice of frequency and plate thickness should be considered for the successful excitation of S0 and A1 mode. It is also noted phase velocities are larger than the one of surface wave except for the A_0 mode.

The coupling coefficient of a $ZnO/Si_3N_4/SiO_2$ laminated plate with free surfaces is shown in Fig. 2.15. The figure indicates that the coupling coefficient is relative large (over 1%) in comparison with surface waves in the same structure. However, the figure also shows that at lower frequency-thickness products, S_0 and A_1 cannot be excited. The excitation efficiency of S0 and A1 modes could be large when a corresponding proper frequency-thickness product is chosen.

In this section, velocity dispersion and the coupling coefficients of a single plate and a laminated plate are discussed. In the next section, these dispersion relations will be employed in the acoustoelectric interaction in piezoelectric semiconducting plates.

2.3.2 Acoustoelectric Effect in a Single Piezoelectric Semiconductor Plate

In section 2.2, SAW velocity change and attenuation in a piezoelectric semiconductor is described by Eq. (2.34) and Eq. (2.35). When discussing Lamb wave propagation in a PS plate, dispersion relation of phase velocity and coupling coefficient must be taken into account. Therefore, by introducing dispersion relations, an AE model applied to Lamb wave propagation in a piezoelectric semiconductor plate is modified as

$$\frac{\Delta v}{v_o(f)} = \frac{K_{eff}^2(f)}{2} \frac{1}{1+\left(\sigma_d / \sigma_m\right)^2} \tag{2.46}$$

$$\frac{\Gamma}{k_x(f)} = \frac{K_{eff}^2(f)}{2} \frac{\sigma_d / \sigma_m}{1+\left(\sigma_d / \sigma_m\right)^2} \tag{2.47}$$

where the phase velocity $v_o(f)$ and coupling coefficient $K_{eff}^2(f)$ can be calculated by

employing the transfer matrix method.

A piezoelectric semiconducting ZnO membrane with thickness of $1\mu m$ is used as a numerical example to demonstrate influences of AE interaction on Lamb wave propagation. Assume the bottom surface is free, the velocity change of A_0 mode due to AE interaction with different conductivities is shown in Fig. 2.16. The main difference between Lamb waves and surface waves in a half-space is that the coupling coefficient which influences the velocity change varies with frequency. For a same material, the coupling coefficient of Lamb waves is usually larger than that of surface waves. Moreover, unlike the constant value of K_{eff}^2 of surface waves in a single piezoelectric semiconducting material, one can achieve better velocity shift by choosing proper frequency and thickness product when using a piezoelectric semiconducting plate as a media for AE interaction. For example, compare Fig. 2.16 with Fig. 2.6, at $\sigma_d = \sigma_m$, the SAW velocity change of ZnO is about 0.25%, while the velocity change of Lamb wave in ZnO is larger than 0.4% at frequencies above 200MHz. Moreover, at higher frequency, the Lamb wave velocity change reaches 0.6% approximately, which indicates that by choosing a proper frequency, the velocity shift of A0 mode Lamb wave of ZnO can be 2.4 times larger than that of SAW in ZnO. On the other hand, when $\sigma_d = \sigma_m$, the Lamb wave velocity shift is smaller than 0.2% at the frequency lower than 100MHz, which means at lower frequency, the Lamb wave velocity shift is smaller than SAW velocity shift due to AE interactions. Therefore, when consider Lamb wave propagation influenced by AE interactions, dispersion relations must be taken into account, and the value of velocity shifts due to AE interactions varies with frequency.

Fig. 2.17 shows acoustic loss of a ZnO plate due to AE interaction. When conductivity changes from $0.1\sigma_m$ to σ_m, the loss becomes larger. When the conductivity goes from σ_m to $10\sigma_m$, the loss decreases. This trend is the same with SAW attenuation which is

affected by the AE effect. It is noted that at $\sigma = \sigma_m$, losses of a ZnO plate are large compared with the one of SAW in a ZnO half-space when frequency is higher than 200MHz. In particular, at higher frequencies, losses of a ZnO plate due to AE interactions are even 2.4 times larger than SAW losses of ZnO. Therefore, losses of Lamb waves in a ZnO plate resulting from the AE effect are larger than the SAW losses of ZnO in a range of frequency, and the losses can be adjusted by tuning the operating frequency of a Lamb wave device.

2.3.3 Acoustoelectric Effect in a Multi-layered Plate Structure

A laminate plate composed of piezoelectric semiconducting $0.5\mu m$ ZnO membrane, $0.2\mu m$ Si_3N_4 and $0.2\mu m$ SiO_2 is used as a numerical example to demonstrate influences of AE interaction on A_0 mode Lamb wave. This structure is chosen because when realizing a Lamb wave device, silicon nitride or silicon dioxide is often used to support the ZnO membrane and makes the fabrication process easier. Again, the free surfaces condition is assumed in this numerical calculation. Fig. 2.18 shows the velocity change in a ZnO/ Si_3N_4/ SiO_2 laminated plate. The curves are similar to the one in a single ZnO plate because the difference of free phase velocities in these two structures is small. Loss of a ZnO/ Si_3N_4/ SiO_2 laminated plate due to AE interaction is shown in Fig. 2.19. Compare Fig. 2.19 with Fig. 2.17, one can find that loss in this laminated plate is smaller than the single ZnO plate. This phenomenon results from the smaller K_{eff}^2 of the laminated plate compared to the one of the ZnO plate. Therefore, velocity shift and acoustic loss of Lamb waves due to AE interactions depend not only on frequency but also on different structures. To further demonstrate this, three types of layered structures are discussed in the following.

Fig. 2.20 shows velocity change due to AE interactions at $\sigma = \sigma_m$ in Si-based layered structures. The bold line represents the velocity change of A_0 mode in a ZnO(0.5)/

Si_3N_4(0.2)/ SiO_2(0.2) laminated plate, the thin line represents the velocity change of A_0 mode in a ZnO(0.5)/ Si_3N_4(0.2)/ SiO_2(0.2)/Si(5) laminated plate, and the dashed line represents SAW velocity change in a ZnO(0.5)/ Si_3N_4(0.2)/ SiO_2(0.2)/Si(300) layered structure. The number in parentheses represents the thickness of the material. In this figure, velocity shifts of A_0 mode in a ZnO(0.5)/ Si_3N_4(0.2)/ SiO_2(0.2) laminated plate are much larger than SAW velocity changes in a ZnO(0.5)/ Si_3N_4(0.2)/ SiO_2(0.2)/Si(300) layered structure. For example, the maximum velocity change of A_0 mode in ZnO(0.5)/ Si_3N_4(0.2)/ SiO_2(0.2) is 0.52% at 747MHz, while the maximum SAW velocity change in ZnO(0.5)/ Si_3N_4(0.2)/ SiO_2(0.2)/Si(300) is 0.17% at 1GHz. Therefore, by choosing proper frequency, the velocity change of A_0 mode can be more than three time of SAW velocity change due to AE interactions. On the other hand, velocity changes of A_0 mode in a ZnO(0.5)/Si_3N_4(0.2)/SiO_2(0.2)/Si(5) laminated plate only differ slightly from SAW velocity changes in ZnO(0.5)/Si_3N_4(0.2)/SiO_2(0.2)/Si(300). Velocity changes of A_0 mode in ZnO(0.5)/Si_3N_4(0.2)/SiO_2(0.2)/Si(5) are even smaller than SAW velocity changes in ZnO(0.5)/Si_3N_4(0.2)/SiO_2(0.2)/Si(300) form 400 to 800MHz. the maximum velocity change of A_0 mode in ZnO(0.5)/Si_3N_4(0.2)/SiO_2(0.2)/Si(5) is 0.18% at 1GHz, while the maximum SAW velocity change in ZnO(0.5)/Si_3N_4(0.2)/SiO_2(0.2)/Si(300) is 0.17% at 1GHz. Therefore, when using the AE effect, a ZnO(0.5)/Si_3N_4(0.2)/SiO_2(0.2)/Si(5) Lamb wave device does not show advantages as a sensor compared to a ZnO(0.5)/Si_3N_4(0.2)/ SiO_2(0.2)/Si(300) SAW device.

Fig. 2.21 shows acoustic attenuation due to AE interactions at $\sigma = \sigma_m$ in Si-based layered structures. The bold line represents the attenuation of A_0 mode in a ZnO(0.5)/ Si_3N_4(0.2)/ SiO_2(0.2) laminated plate, the thin line represents the attenuation of A_0 mode in a ZnO(0.5)/Si_3N_4(0.2)/SiO_2(0.2)/Si(5) laminated plate, and the dashed line represents SAW attenuation in a ZnO(0.5)/Si_3N_4(0.2)/SiO_2(0.2)/Si(300) layered structure. Fig. 2.21

indicates that the trend of acoustic loss is the same with the velocity changes shown in Fig. 2.20. The reason is that at $\sigma = \sigma_m$, Eq. (2.46) and (2.47) give the same values. By choosing proper frequency, the attenuation of A_0 mode in a $ZnO(0.5)/Si_3N_4(0.2)/SiO_2(0.2)$ laminated plate can be three times or even larger than SAW loss in a $ZnO(0.5)/Si_3N_4(0.2)/SiO_2(0.2)/Si(300)$ layered structure due to AE interactions. However, attenuation in a $ZnO(0.5)/Si_3N_4(0.2)/SiO_2(0.2)/Si(5)$ laminated plate is not much larger than SAW loss in a $ZnO(0.5)/Si_3N_4(0.2)/SiO_2(0.2)/Si(300)$ layered structure. At some frequencies, attenuation due to AE interactions in $ZnO(0.5)/Si_3N_4(0.2)/SiO_2(0.2)/Si(5)$ laminated plate are even smaller than SAW loss in a $ZnO(0.5)/Si_3N_4(0.2)/SiO_2(0.2)/Si(300)$ structure, which indicates that the advantages of a Lamb wave device is not obvious if an improper structure or frequency is chosen. Therefore, when designing a Lamb wave sensor using the AE effect, the dispersion must be taken into account to calculate velocity change and acoustic losses. And the results can be a principle for ones to choose materials of a layered plate and the operating frequency.

In short, by introducing dispersion relations, a modified AE model applied to Lamb wave propagations in single and laminated PS plates are constructed and discussed in this section. Results show that the influence of AE interactions on Lamb wave propagations which is dominated by the coupling coefficient can be designed through calculations of dispersion relations in different propagating media. By a proper choice of a Si-based Lamb wave structure and the operating frequency, the velocity change and attenuation due to the AE effect can be 3 times larger than those in a Si-based SAW device. The choice of thickness of ZnO, Si_3N_4 and silicon will be further discussed in chapter 4.

2.4 Temperature Effect on Acoustoelectric Interaction

Previous sections have demonstrated that the crucial parameters dominating acoustoelectric interaction are the conductivity and the coupling coefficient of the propagating media. In fact, conductivity in a piezoelectric semiconductor is affected by the temperature because of the native properties of semiconducting. The conductivity $\sigma = nq\mu$ indicates that the conductivity is determined both by carrier concentration and mobility.

To discuss the temperature effect on conductivity, one should consider both the relationships between temperature and carrier concentration / mobility.

Take ZnO for example, the relation between mobility and temperature in some range is[39]

$$\mu \cong 3000(m/m^*)^{3/2}(300/T)^{1/2} \tag{2.48}$$

where m^* is the effective mass. This equation indicates that the mobility decreases when temperature increases in some range. Look[91] in 2001and Ozgur[92] et al. in 2005 showed that the mobility of ZnO increases at low temperature but decrease at T>50K. However, the mobility only changes slightly when T=300~400K. Therefore, the dependence of ZnO conductivity on temperature due to mobility for realistic application is not obvious.

The temperature dependence of carrier concentration can basically be expressed as

$$n \propto A\exp(-B/T) \tag{2.49}$$

where T is the temperature; A and B are constants which depends on material. As shown in the equation, n is exponential dependent on temperature. In physical, this phenomenon can be explained as follows. When the temperature of a semiconductor is extremely low, nearly all electrons are held tightly by individual atoms, the carriers are hard to jump into the conduction band due to lack of energies. When a semiconductor is heated, the heat energy

provides more electrons to break away from individual atoms, and become free to move through the semiconductor, which leads to higher carrier concentration and higher conductivity. Therefore, the conductivity of a semiconductor increases with increasing temperature. Because the constants A and B in Eq. (2.49) vary with different materials and differ from the growth condition of a semiconductor, a numerical simulation for the dependence of acoustoelectric interaction on temperature cannot be calculated. However, for realistic applications, the AE interaction can be enhanced not only by material choosing, which mainly decides the velocity and coupling coefficient, but also can be improved by increasing temperature which increases conductivity.

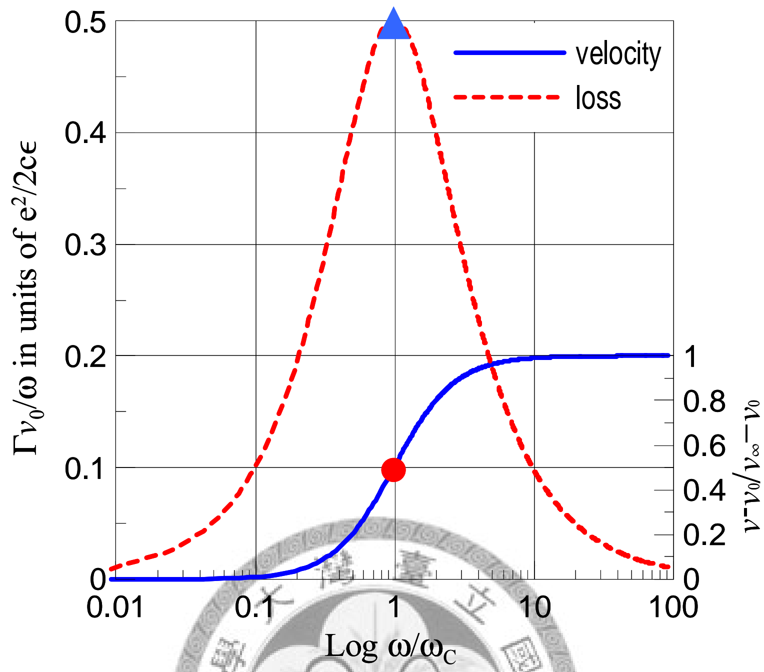

Fig. 2.1 Acoustic velocity shift and attenuation due to AE interaction in an unbounded piezoelectric semiconductor

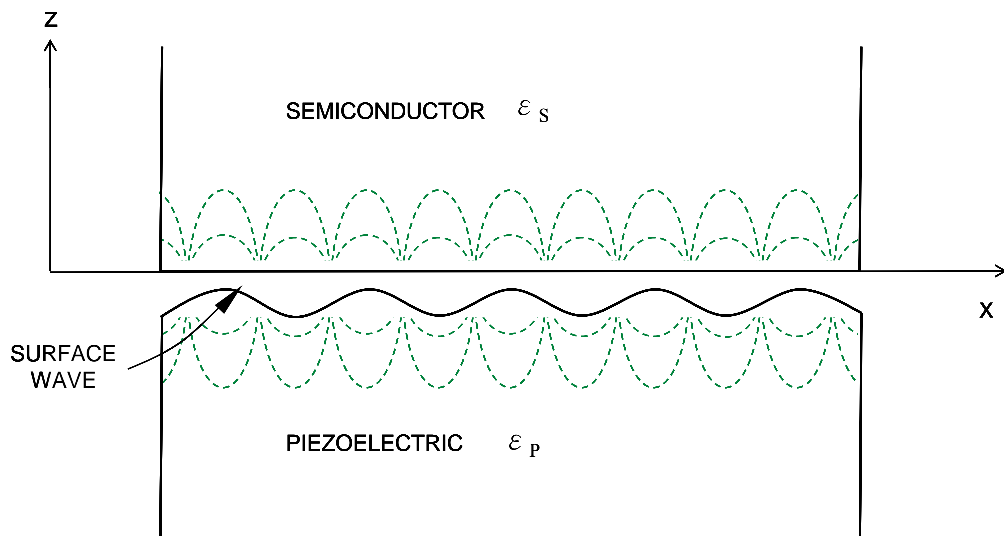

Fig. 2.2 Surface waves propagating on a piezoelectric insulator with an adjacent semiconductor

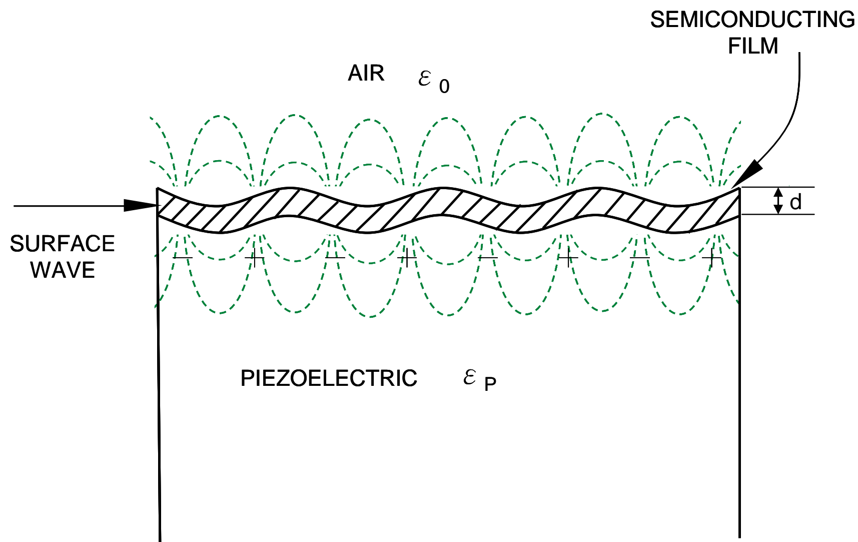

Fig. 2.3 Surface waves propagates on a surface made up of an ultra- semiconducting film on a piezoelectric insulator

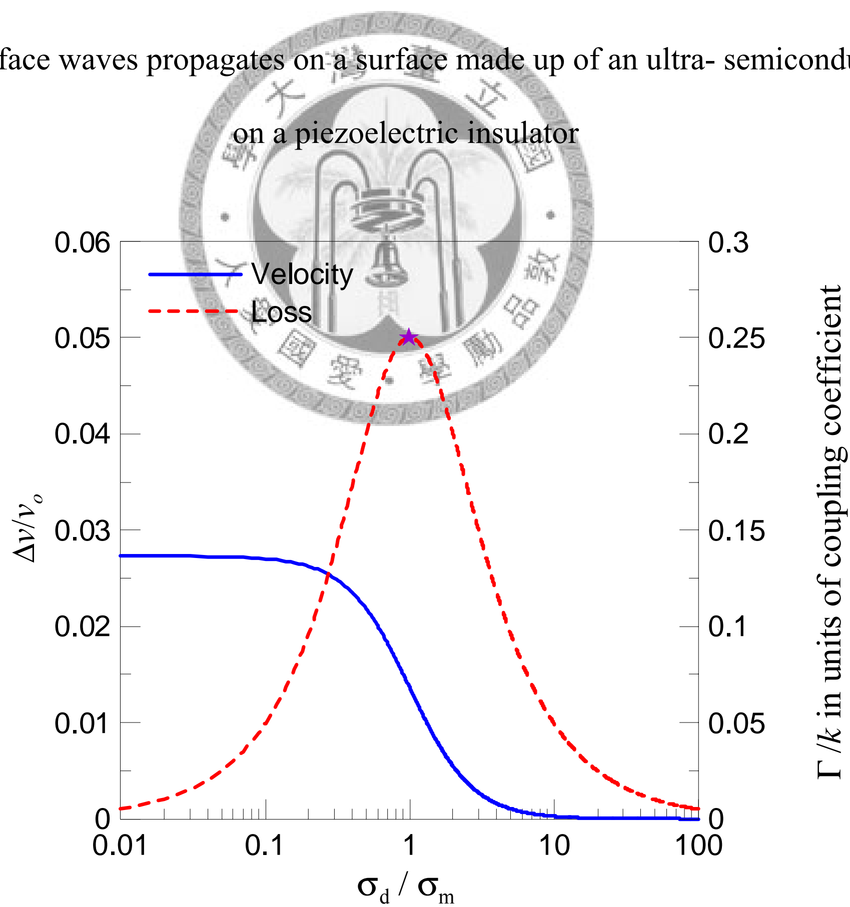

Fig. 2.4 SAW velocity change and attenuation on a $LiNbO_3$ substrate with a thin sheet of mobile carriers

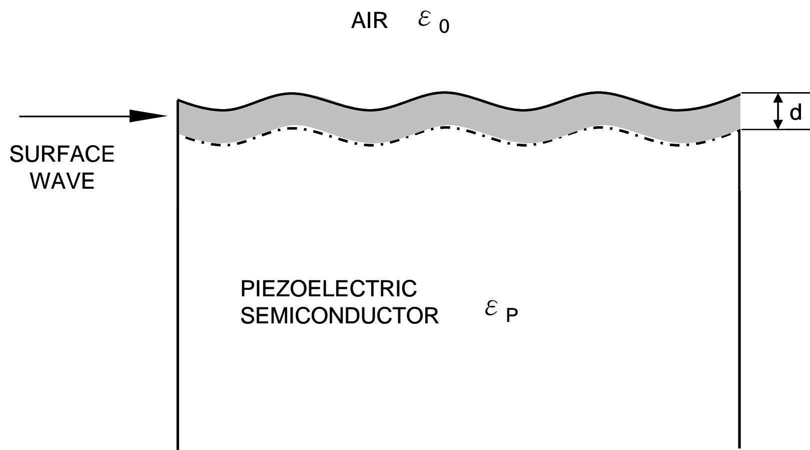

Fig. 2.5 Surface waves propagating in a piezoelectric semiconductor

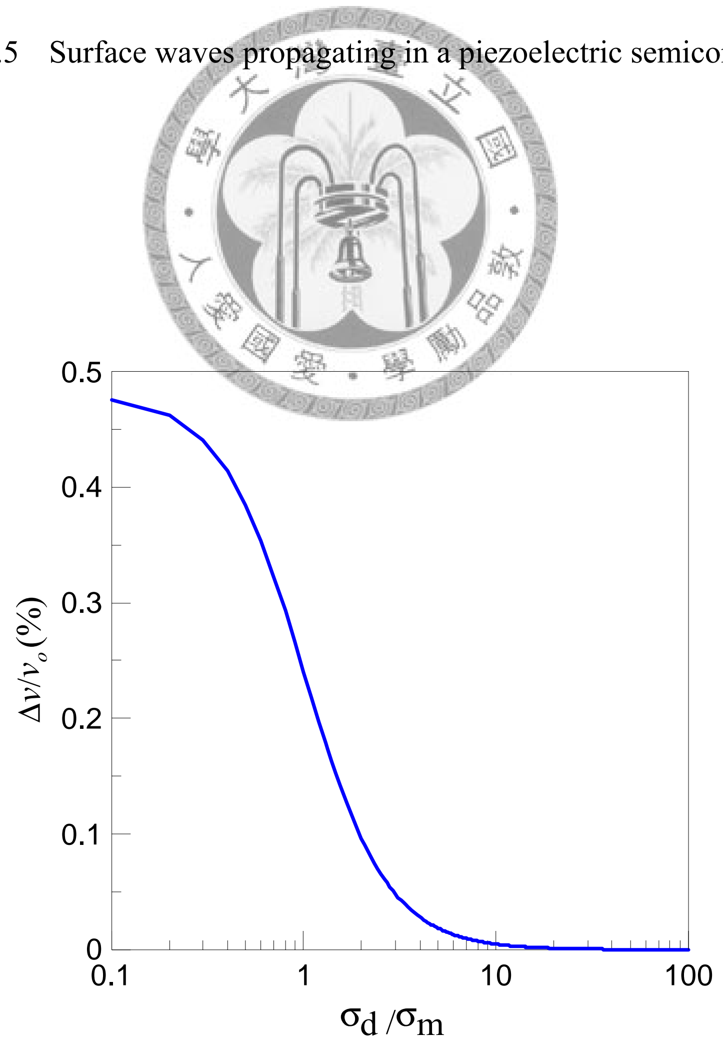

Fig. 2.6 SAW Velocity change of ZnO due to AE interaction

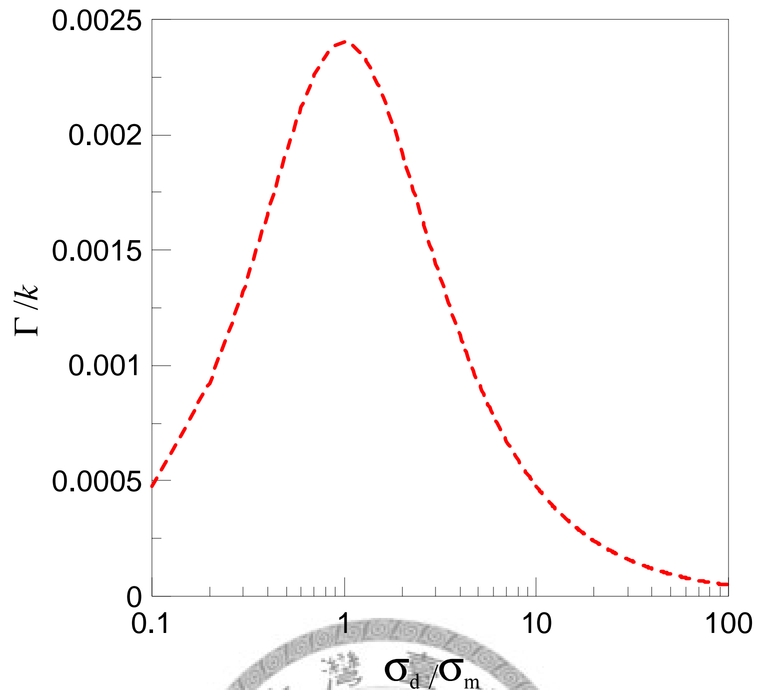

Fig. 2.7 SAW attenuation of ZnO in units of coupling coefficient

國立臺灣大學

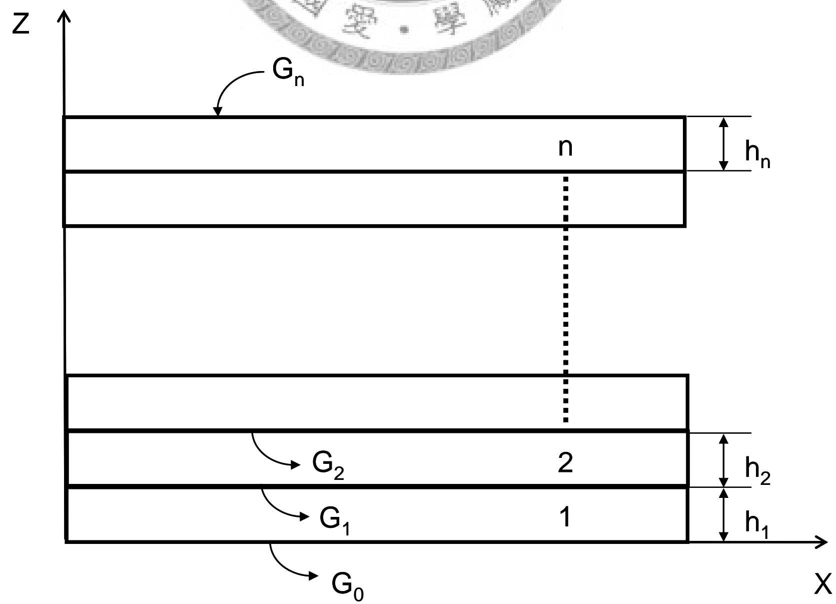

Fig. 2.8 A laminated plate structure

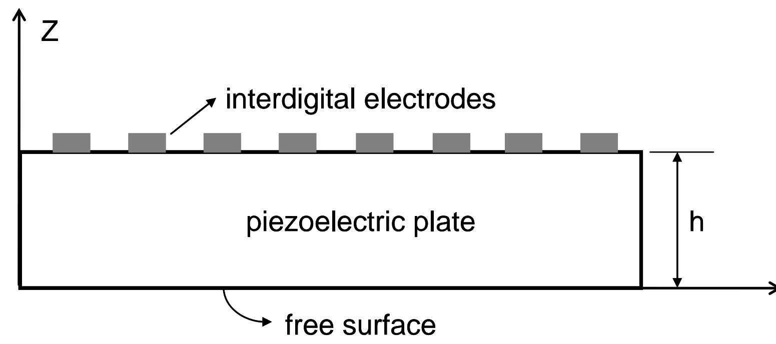

Fig. 2.9 A piezoelectric plate with a free down surface

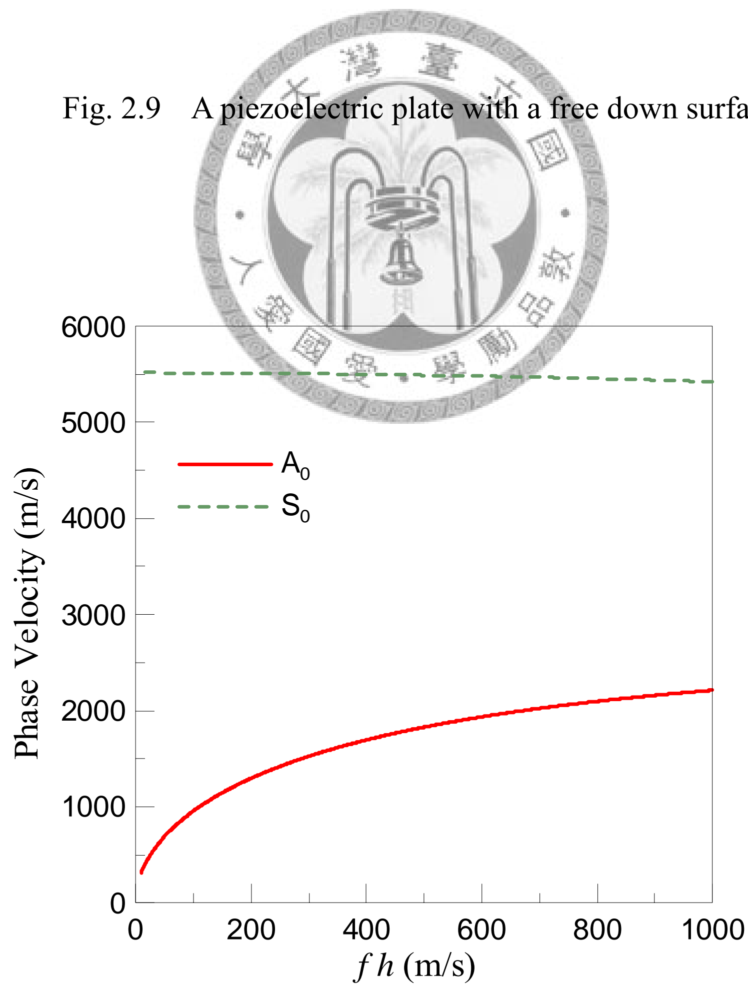

Fig. 2.10 Phase velocity dispersion of a ZnO plate with free down surface

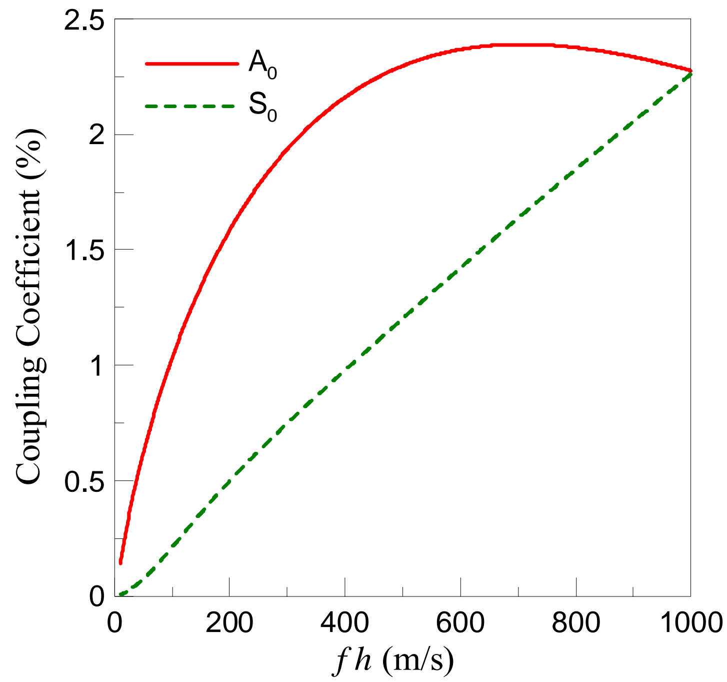

Fig. 2.11 Coupling coefficient of a ZnO plate with free down surface

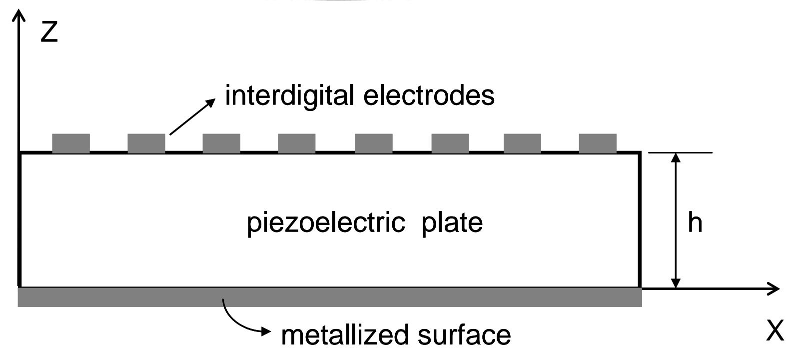

Fig. 2.12 A piezoelectric plate with a metalized down surface

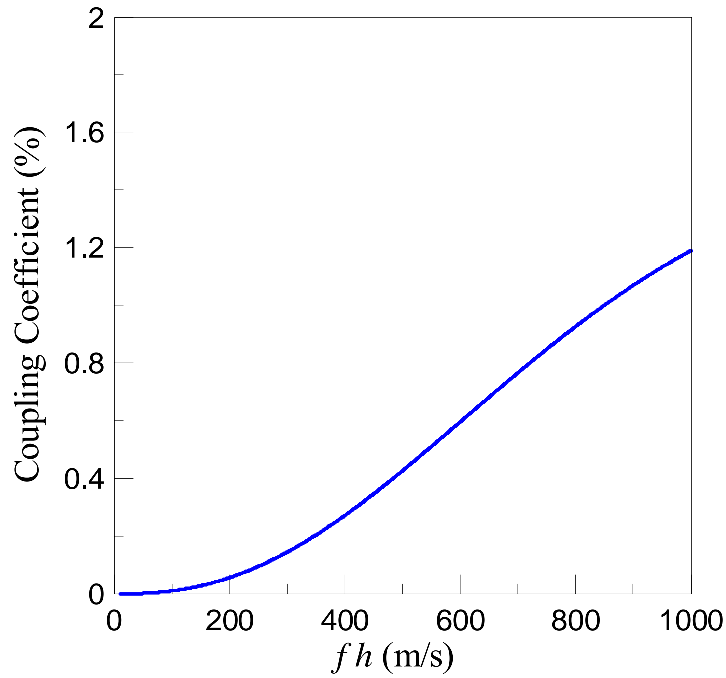

Fig. 2.13 Coupling coefficient of lowest antisymmetric mode in a ZnO plate with metalized down surface

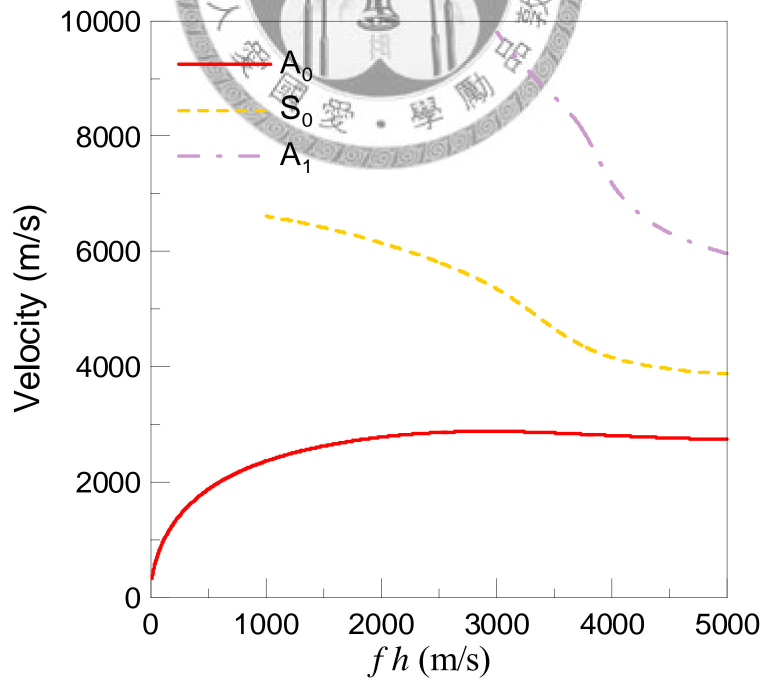

Fig. 2.14 Phase velocity dispersion of a $ZnO/Si_3N_4/SiO_2$ laminated plate

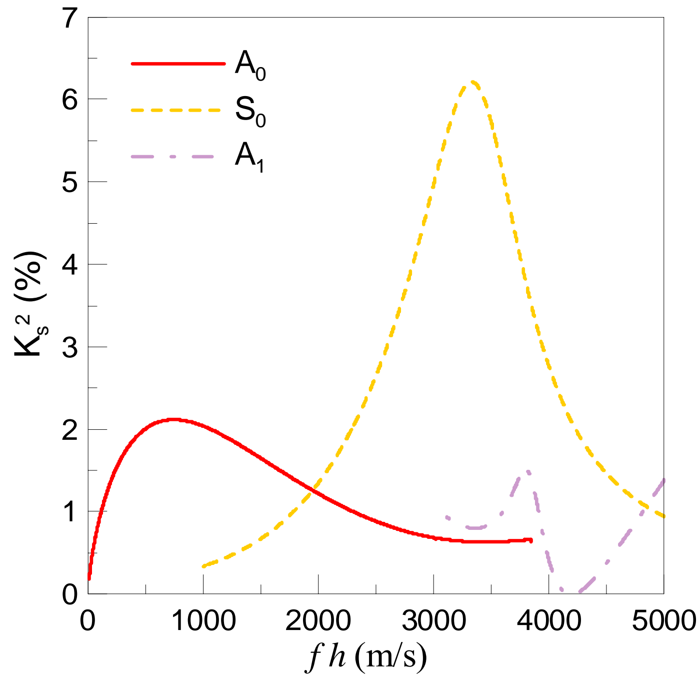

Fig. 2.15 Coupling coefficient of a $ZnO/Si_3N_4/SiO_2$ laminated plate

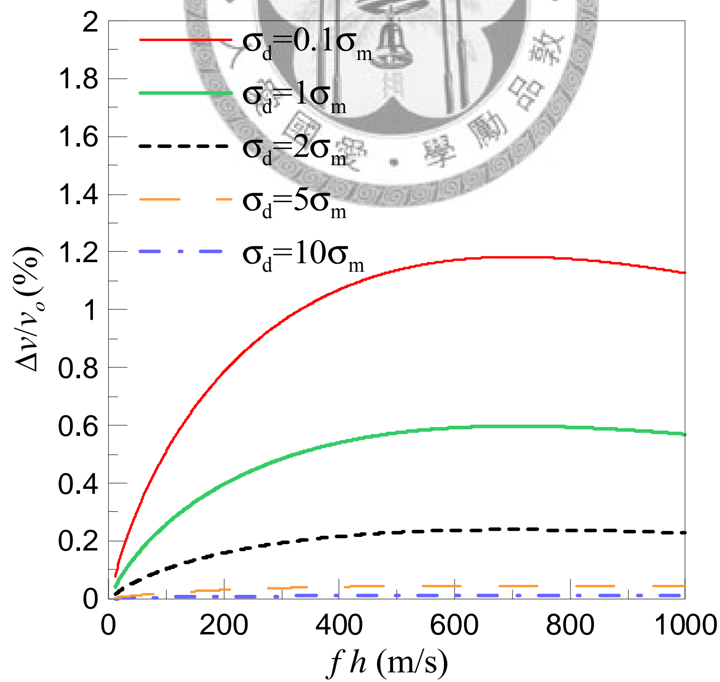

Fig. 2.16 Velocity changes of A0 mode of a ZnO plate due to AE interaction

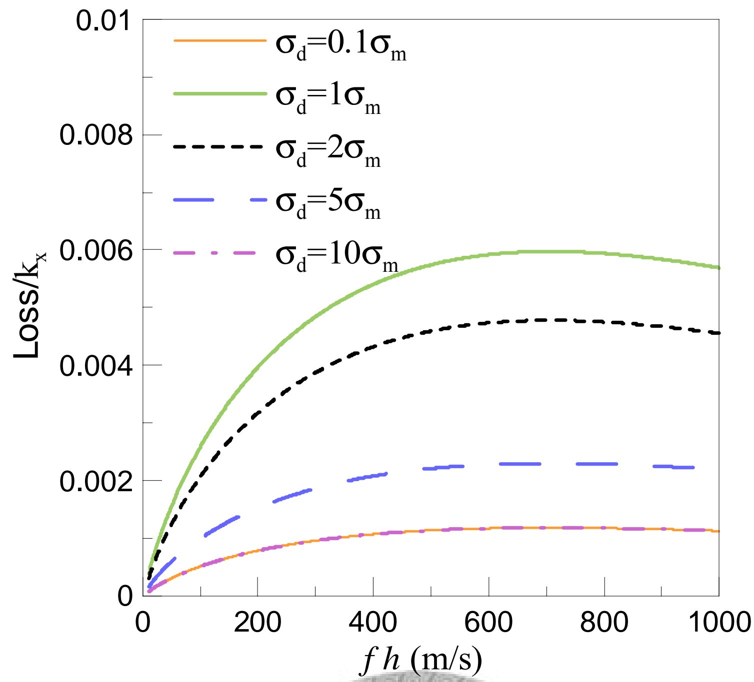

Fig. 2.17 Loss of A0 mode of a ZnO plate due to AE interaction

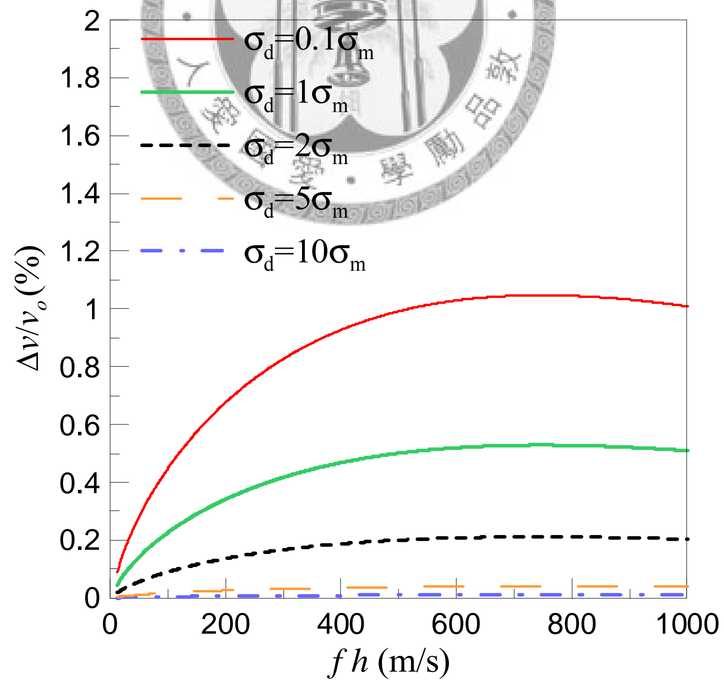

Fig. 2.18 Velocity change of a $ZnO/Si_3N_4/SiO2$ plate due to AE interaction

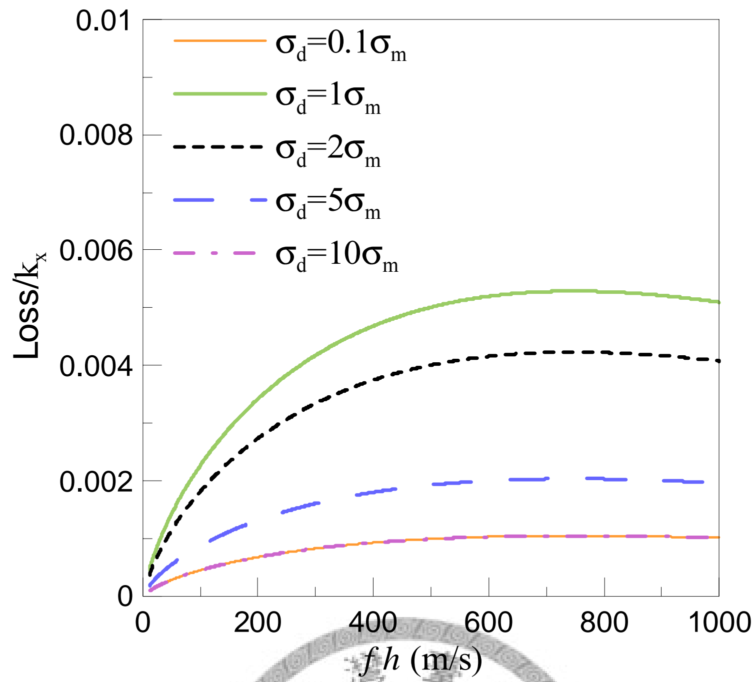

Fig. 2.19 Loss of a ZnO/ Si_3N_4/SiO2 due to AE interaction

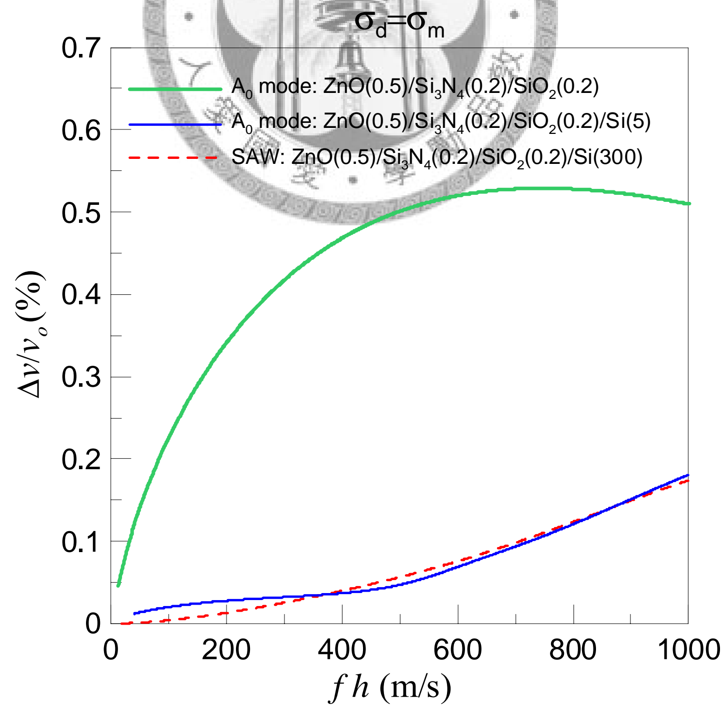

Fig. 2.20 Velocity shifts of different layered structure due to AE interactions

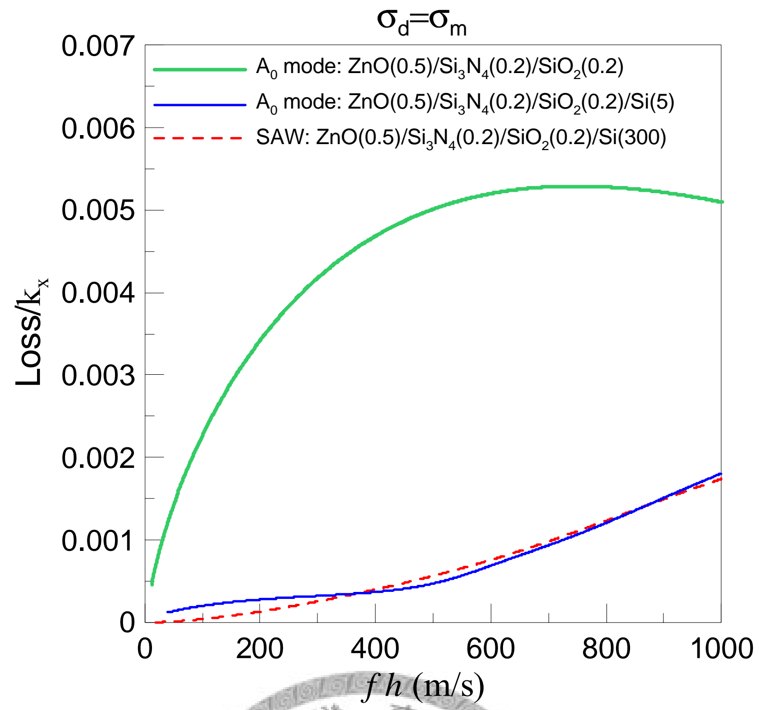

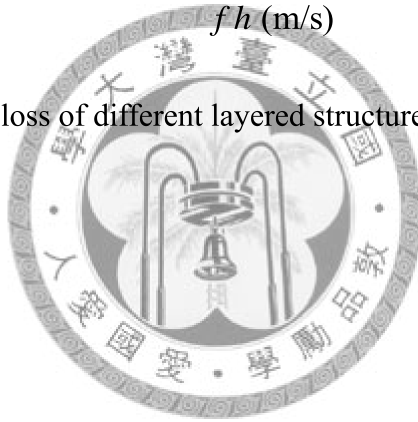

Fig. 2.21 Acoustic loss of different layered structure due to AE interactions

Chapter 3 A ZnO-Nanorod Based SAW Sensor for Ultraviolet Detection

In Chapter 2, influences of acoustoelectric effect on surface wave and Lamb wave propagations are presented. To substantiate the effect of acoustoelectric interactions on surface wave propagations, this chapter embodies a real-time, high-precision ultraviolet (UV) detector. A UV detector which comprises of a surface acoustic wave oscillator and ZnO nanostructure used as sensing material is demonstrated for the first time. Section 3.1 shows a design of interdigital transducer (IDT) and electrical circuit for SAW oscillator. Then, a two-port SAW oscillator is fabricated on a 128°YX-LiNbO3 substrate, and the growth condition of ZnO nanorod on the substrate is introduced in Sec. 3.2 Before setting up an ultraviolet sensing system, functions of SAW oscillators must be checked. Sec. 3.3 shows the measurement results of a single SAW resonator and a dual-channel-configuration SAW oscillator. By combining the SAW oscillators and ZnO nanorod, a UV detector based on a dual delay line SAW oscillator system is constructed. In Sec. 3.4, properties such as real-time response, repeatability and stability of the UV detector are measured. Sensibility related to different power densities are also recorded and discussed. Conductivities of ZnO were also calculated based on both experimental results and theoretical simulation.

3.1 Design of a SAW oscillator system based on ZnO/$LiNbO_3$ structure

In this section, crucial design parameters of a SAW resonator and a calculation result

of the frequency response are introduced. Working principle of electrical circuit and the simulation of an amplifier circuit are described.

3.1.1 Design of a SAW Resonator

Performance of a surface acoustic wave device is mainly governed by the choice of a substrate and design of the interdigital electrodes. To achieve lower insertion loss of a SAW oscillator, higher electromechanical coupling coefficient (K^2) is needed. Table 3.1 shows properties of several common piezoelectric substrate materials used for SAW devices and sensors[93]. Each material contains specific advantages and disadvantages. Among these materials, 128°YX-$LiNbO_3$ has largest coupling coefficient and highest propagation velocity. High piezoelectricity of $LiNbO_3$ not only offers excellent piezoelectric conversion but also scales down the size of a SAW device by reducing IDT pairs. On the other hand, the change in SAW velocity due to acoustoelectric interaction is also proportional to the electromechanical coupling coefficient K^2. A material with a large coupling coefficient such as $LiNbO_3$ is, thus, highly suitable for UV detecting utilizing acoustoelectric effect. Moreover, with the same IDT finger-spacing, high propagation velocity of 128°YX-$LiNbO_3$ raises operating frequency compared to other materials listed in Table 3.1. Therefore, we design and fabricate SAW oscillators on a 128°YX-LiNbO3 substrate.

Interdigital transducers (IDTs) applied to a piezoelectric substrate have been widely employed for the excitation and detection of surface acoustic waves. There are several important theories for designing SAW devices: delta-function model[94], equivalent circuit model[95,96] and coupling-of-modes (COM) model[97]. Delta-function model, the simplest of the various models, provides basic characteristics of IDTs and frequency response of a SAW device. However, it cannot deal with impedances of IDTs, thus absolute insertion loss

values of SAW devices cannot be obtained. Equivalent circuit model has been used for modeling SAW devices as an alternative. Equivalent circuit model not only yields information on impedances of IDTs but also includes some important effects such as internal reflection within IDTs and triple-transit interferences in the passband. Apart from these models, the COM model has been also widely applied for designing SAW devices. The COM model begins by the first-order differential wave equations, and perturbations resulting from IDTs are added to the wave equations individually. The perturbations include propagation loss, electrical transduction, electrode reflections, thin film finger resistance and distributed finger capacitance. These perturbations thus introduce coupling between the waves and the IDTs. Typically, the COM model can deal with arbitrary chirping or weighting of the transducers and gratings. In this research, the COM model is adopted for simulating the frequency response of a SAW resonator. The COM model applies on piezoelectric half space, while the thickness of ZnO is negligible compared to the acoustic wavelength and the thickness of the $LiNbO_3$ substrate. Thus the effect of dispersion due to the ZnO film is excluded.

Primary characteristics of a frequency response of a SAW resonator are central frequency, insertion loss and bandwidth. Parameters related to IDTs which influence these characteristics are the number of finger-pairs in the IDT, the number of gratings, delay-line distances, and thickness of metal films[98]. Fig. 3.1 is a diagram of a two-port SAW resonator. λ is the acoustic wavelength, d is the delay distance between transducers and reflective gratings, D is the delay length of input IDT and output IDT, W is the aperture of transducers, and Λ is the periodicity of gratings. Herein a two-port SAW resonator of 145MHz on a 128°YX-$LiNbO_3$ substrate is designed. In the design, acoustic wavelength is $27\,\mu m$, IDT finger space is $6.75\,\mu m$, delay length D is 160λ, aperture is 100λ, and

finger pairs of IDT are 20. The periodicity of gratings is 13.5 μm, the number of gratings is 50, and the delay distance d is 3/8 λ. By substituting these parameters into the COM model, a frequency response can be simulated, as shown in Fig. 3.2. The simulation reveals that the insertion loss of this SAW resonator is 3dB, and the central frequency is 144.6MHz. The measurement result of the realized device will be discussed later.

3.1.2 Electrical Circuit Design

For real-time sensing which is based on a two-port SAW resonator, an oscillator loop is the most common-used system. Fig. 3.3 shows a typical configuration of oscillator loop in which a SAW resonator is used as a feedback-determining element, controlling the frequency of this oscillator circuit. An oscillator circuit comprising a resonator, an amplifier and a phase shifter can create a high-stability SAW oscillator. The electronic circuit delivers the driving signal for sustaining oscillation and supplies the output port for real-time monitoring the resonant frequency.

For stable oscillation at a desired frequency, the gain of the amplifier must exceed the total insertion loss of components in the feedback loop. Moreover, total phase shift around the circuit loop must be an integral multiple of 2π radians to accomplish positive feedback. When these two conditions are satisfied, the feedback procedure is repeated cycle by cycle and the output signal is continuously enhanced to achieve the maximum oscillating level. The oscillator circuit oscillates at a steady state when the oscillation frequency and the amplitude of the signal are fixed.

The amplifier used in this SAW oscillator circuit adopts the Philips BF17 NPN transistor as one of the components[99]. To assure the amplifier gain be larger than the total loss of the oscillator circuit, two amplifiers are cascaded in the circuit. These two stages provide a value of 40dB, sufficient for sustain the oscillation. Fig. 3.4 is a schematic layout

of the amplifier circuit. The pair associated with the base of transistor, i.e., R1 and R2 of the first stage; R3 and R4 of the second one, form a voltage divider network from the DC voltage. The voltage divider makes the transistor operate by DC biasing. Generally, the base voltage must exceed the emitter voltage by at least 0.6 volts, and the current through the emitter are usually five to ten times of the base current. Thus the values of R5 and R6 can be calculated. Bypass R5 and R6 with capacitors C3 and C4 respectively is to increase the gain of the stage. C1, C2 and C5 are coupling capacitors which serve to isolate the RF signal form DC bias voltages. In other words, these coupling capacitors are for DC blocking, therefore, DC voltages in one stage will not transfer to adjacent stages. Inductors L1 and L2 are used as RF choke. The response of the amplifier shown in Fig. 3.5 is simulated by using Agilent ADS software. As shown in the figure, amplifier gain is larger than 40 dB in the range of 70 to 150MHz, which fits the requirement of the designed operating frequency in this research well.

3.2 Fabrication of a SAW Device with ZnO-Nanorods Sensing Material

This section clarifies the photolithographic process of realizing a two-port SAW resonator. The growth method and conditions of ZnO nanorod are also illustrated in this section.

3.2.1 Fabrication of a SAW device

A two-port SAW resonator of which the electrodes are in micro-scale can be fabricated through photolithographic process. Details of fabrication process are shown in Fig. 3.6 and described as follows.

(i) Wafer Cleaning:

For a successful fabrication of micro-scale IDTs on a substrate, effective cleaning of a

$LiNbO_3$ wafer is an essential procedure. A through cleaning of the substrate surface is vital for obtaining good adhesion and uniform deposition of the metal film which is used for forming IDTs. To prevent any surface contaminants such as dust or soluble organic particles, the $LiNbO_3$ wafer was immersed in acetone for 5 minutes, followed by a methanol bath for 5 minutes and finally rinsed with deionised water for 5 minutes. Then the wafer was dried by nitrogen gas. If obstinate contaminants exist, the wafer can be immersed in a mixture of three parts of H_2SO_4 and one part of H_2O_2 for further cleaning.

(ii) Metallization:

After cleaning the substrate, a metal layer can be deposited. Aluminum and Gold are the most commonly used material for IDTs fabrication on acoustic wave devices. Nevertheless, the adhesion of Au to substrate is poor and additional chromium as an adhesion layer is needed. Aluminum adheres well to the substrate and has lower density compared with gold. Lower density of aluminum stands for fewer reflections from IDTs and smaller passband ripples in the frequency response. Therefore, aluminum is employed as metal film to form IDTs. Aluminum thin film was deposited on $LiNbO_3$ substrate by E-beam evaporation and the thickness was 150nm.

(iii) Coating of Photoresist:

Before the deposition of a positive photoresist, the metalized wafer was rinsed in acetone to remove surface contaminants appeared during storage since the metallization procedure. Then the wafer was rinsed in methanol and deionised water for 5 minutes respectively, followed by an oven bake at 90℃ for 10 minutes. Positive photoresist was spun at 1000rpm for 5 seconds, 1500 rpm for 5 seconds and 3000 rpm for 30 seconds by using a Laurell spin coater. The parameters of spin formed a photoresist layer of 1 micron thick approximately. The photoresist-coated wafer was then prebaked on a hotplate at 90℃ for 90 seconds to drive off excess solvents from the photoresist. Before exposed under UV

light, the photoresist-coated wafer was cooled to room temperature.

(iv) Exposure and Developing

The wafer coated with photoresist was exposed to UV light for 11 seconds with a EVG 620 Top Side Mask Aligner. Then the exposed wafer was developed in a MF-319 developer, followed by a deionised water rinse. The pattern was checked by careful inspection under a microscope. At this stage, timing of exposure and developing should be precisely controlled or the fabrication success will be degraded because of under-developing or over-developing.

(v) Etching and Removal of Photoresist

Before etching process, a post bake of the wafer was performed in an oven at 90℃ for 20 minutes. The post bake supported the formation and hardening of the required shape of the photoresist. After post bake and cooling, the aluminum layer unprotected by the photoresist was then etched by an etchant consisting of 16 parts of phosphoric acid (H_3PO_4), one part of acetic acid (CH_3COOH), one part of nitric acid (HNO_3) and 2 parts of deionised water. Great care should be taken at this stage because undercutting of the structure will occur with prolonged time. After chemical wet-etching, the wafer was rinsed by deionsed water to prevent any residual etchant on the wafer. Then the wafer was rinsed in acetone, methanol and deionised water for 5 minutes respectively to remove the photoresist, and dried by nitrogen gas. The whole fabrication process of two-port SAW resonators was accomplished.

Following successful fabrication, frequency response was measured by an Agilent 8714ES Network Analyzer. The measurement result was shown in Fig. 3.7, the center frequency is 145.81MHz and the insertion loss is 10.1dB. Though the value of insertion loss is lower than the simulation result, the performance is good enough for being a SAW sensor.

3.2.2 ZnO Nanorod Growth

One-dimensional ZnO film, a well-known semiconducting and piezoelectric material, has been widely used in electronic applications. ZnO is also sensitive to ultraviolet due to its attractive optical properties, including wide band-gap of 3.4eV and large exciton binding energy of 60 meV at room temperature. Large photoresponse of ZnO thin film makes it be a promising material used in optical and optoelectric applications. Recently, there has been a growing interest in investigating the properties of nanostructured ZnO. Researches on ZnO nanostructures also have drawn much attention because of their excellent physical properties as well as ZnO film. A number of studies focused on the synthesis of ZnO nanostructures such as nanowires[100], nanorods[101] and nanobelts[102] have been reported. A ZnO nanostructure has been demonstrated as a candidate material for broad applications in technology, including UV lasers[103], field emitters[104] and solar cells[105]. ZnO nanorods are also widely used as sensing materials in humidity sensors[99], gas sensors[19] and biosensors[106] because of their properties including high sensitivity, rapid response and fast recovery. Furthermore, ZnO nanorods have a wide bandgap as ZnO films do, and have a larger surface-to-volume ratio compared with ZnO films, which may yield high light absorption in the UV region and may enhance the response under UV illumination. Therefore, ZnO nanorods are adopted as the UV sensing material in this research.

In this study, a ZnO nanostructure was grown on a LiNbO3 substrate by using the chemical solution method[107]. Before ZnO nanorod growth, a ZnO thin film was deposited on the fabricated two-port SAW resonator by a radio-frequency magnetron sputtering system. The ZnO target is with a purity of 99.99%. The sputtering conditions were 150 W for 25 min, with 25% Ar and 45% O_2. And the substrate temperature was 200℃. This sputtered 50 nm thick ZnO thin film was used as a seed layer for the following growth of

the ZnO nanostructure. It should be noticed that ZnO films and the followed nanorods were grown only on the sensing area, which means the delay line between two IDT electrodes. After deposition of the ZnO seed layer, frequency response was measured, as schematic shown in Fig. 3.8, the center frequency is 145.75MHz and the insertion loss -10.3dB. Compared to Fig. 3.7, the influence on performance of the SAW resonator after the growth of the ZnO thin film was negligible. Moreover, the property of the sputtered ZnO thin film was investigated by using X-ray diffraction method (XRD), as shown in Fig. 3.9. The intensity peak of (0 0 2) is not strong, resulting from too short deposition time for the ultra-thin ZnO film to be well-organized. However, the peak at (0 0 2) orientation represents the C-axis growth of the ZnO film.

Subsequently, the seeded $LiNbO_3$ substrate was immersed in a solution containing a mixture of zinc nitrate hydrate (0.025 M) and methenamine (0.025 M) at 95℃ for 5 hours. With the mixture, ZnO nanorods will be grown on the ZnO seed layer for proper temperature and growth time. After this treatment, the substrate was rinsed with deionized water and dried by nitrogen gas, and the ZnO nanorods were grown on the substrate successfully. Fig. 3.10 shows a SEM image of a top view of the ZnO nanorods. Average diameter of the ZnO nanorods is less than 150 nm. In addition, the height of the ZnO nanorods is about 450 nm. Fig. 3.11 is the XRD pattern of the ZnO nanorods. An intensity peak at 34.45° which represents ZnO(002) diffraction was observed. This diffraction peak indicates preferential growth in the [0 0 2] orientation of ZnO nanorods. To primarily demonstrate that the ZnO nanorod is applicable to UV detection, a UV absorbance diagram was measured. Fig. 3.12 shows a UV-Vis absorption curve of the ZnO nanorods. The high absorption in the UV region, especially 320-400nm, for the ZnO nanorod showed that this material was extremely suitable as a UV-blocking material.

After the growth of ZnO nanorod, the frequency response was measured again, as

indicated in Fig. 3.13. Though the insertion loss dropped to -16dB, it is still highly suitable for the following experiment. Fig. 3.14 shows the phase of the SAW resonator. The sharp slope of the phase in the narrow passband of the resonator affords good stability for oscillation. It is noted that, with longer growth time, the height of ZnO nanorods will increase. However, when the growth time is longer than 5 h**,** the over-height ZnO nanorods would degrade the performance of the SAW resonator, as shown in Fig. 3.15. The measurement signal shown in Fig. 3.15 cannot provide sufficient power for oscillation, namely, the growth time of ZnO nanorod ought to be well-controlled for assuring oscillation.

3.3 Measurement of SAW Oscillators

Functions of SAW oscillators must be checked before setting up an ultraviolet sensing system. This section shows the measurement results of a single SAW resonator and a dual-channel-configuration SAW oscillator.

3.3.1 Single SAW Oscillator

The two-port delay line SAW resonator attached on a printed circuit board (PCB) was wired bonded to the amplifier circuit. An operating voltage was applied to the oscillator circuit via a DC power supply, as shown schematically in Fig. 3.16. After applying the operating voltage, the sustained oscillation at locked frequency occurred because of fitted phase angle and appropriate gain. As shown in Fig. 3.17, a Lecroy wavepro 7000 oscilloscope connected to the oscillator displayed the time domain signal and the unperturbed resonance frequency. The fundamental oscillation frequency of the SAW oscillator was 145.5MHz. The harmonic oscillation frequencies were also observed. The higher the harmonic oscillation, the lower the power was. Therefore, the oscillations of harmonic frequencies did not influence the output signal.

3.3.2 Dual-Channel-Configuration SAW Oscillators

Typically, under sensing conditions, the frequency deviations from the unperturbed resonance of a SAW sensor are relatively small, ranging form several kHz to a few MHz. Such small frequency deviation in the very high frequency (VHF) band (30 to 300MHz) measured through a network analyzer is not obvious. Alternatively, frequency deviations can be measured by heterodyning a reference oscillator frequency and a sensing one. This mixing process can move the measurements from RF spectrum down to audio spectrum. Furthermore, to achieve the optimized performance of the SAW sensor, it is important to eliminate environment fluctuations such as temperature and pressure. By using a dual-channel-configuration SAW oscillator system, these fluctuations can be obviated.

The dual-channel SAW oscillator used in this study basically consists of two counterparts; one is a ZnO nanorod-coated SAW oscillator used as the sensing area and the other one remains the bare surface, which is used as a reference. Then, these two single SAW oscillators are connected to a mixer which carries out the plus and minus operations of the SAW frequencies. Next, a low-pass filter mounted after the mixer is to ensure that only the frequency difference was obtained. A schematic of the whole oscillator system is shown in Fig. 3.18. The output signal from the low-pass filter was read out by the oscilloscope. The time and frequency domain signal were shown in Fig. 3.19. The basic frequency difference was 1.5MHz.

3.4 An Ultraviolet Detector based on a SAW Oscillator System with ZnO-Nanorods Sensing Material

After the measurements of SAW oscillators, an ultraviolet detecting system based on SAW oscillator circuit was realized. This chapter starts with the description of the construction of a UV-sensing system and data acquisition system. Next, experimental

results of including repeatability and sensitivity of a UV detector comprising of a dual-channel SAW-oscillator system are presented. Finally, comparison of experimental results and numerical calculations of the acoustoelectric effect are discussed and analyzed.

3.4.1 Experimental Setup of a Ultraviolet Sensing System

Fig. 3.20 shows the experimental setup of a UV detecting system. The SAW oscillator circuit described in Sec. 3.3 is used as a UV detector. A Xenon lamp and a monochromator are combined to be a UV source. The SAW oscillator was then illuminated by this UV source. When the sensing area made of ZnO nanorods was subjected to UV illumination, a frequency shift resulting from the acoustoelectric effect could be observed. The frequency shift is due to the acoustoelectric effect, which means when illuminated by a UV source, the semiconducting ZnO nanorods will absorb the light and electron–hole pairs are generated. These carriers interact with the electric field accompanying the propagating SAW, resulting in a velocity change, and a frequency shift can be observed[20]. The relatively small frequency deviations were fed to a frequency counter Agilent 53131A which is with a resolution of 0.1Hz. Then the frequency counter transmitted the signals into a personal computer with a general purpose interface bus (GPIB) cable for data acquisition. A personal computer with an attached software Intuilink program provided by Agilent is for real-time frequency-differences monitoring and data storing.

3.4.2 Characteristics of the Ultraviolet Detector

When a SAW oscillator system starts to oscillate, there is a basic frequency difference between the sensing channel and the reference one. The sensing channel results in a frequency shift via the interaction between sensing material and UV light. On the other hand, the reference channel offers the source signal for comparison. As Fig. 3.21 shows, the basic frequency difference of this dual delay line SAW oscillator was about 1.3 MHz

before a UV source was switched on. In this research, all measurements were carried out under steady states of the SAW oscillating system.

First, the response and repeatability of the UV detector with various wavelengths of the UV source were discussed. By proper adjusting the distance between the sensor and light source, the power density of the UV source can be set constant to 3.5mWcm^{-2} even when the optical wavelengths are changed. The UV detector was under UV irradiation with three optical wavelengths, 365nm, 370nm, and 375nm, respectively. In Fig. 3.21, the arrows indicate that UV illumination was on, while the triangles represent that the UV source was switched off. Frequency shifts were fed into a frequency counter and immediately recorded by a personal computer when the detector was under 365nm irradiation toward 3 on-off cycles, 370nm for 2 cycles, and 375nm for 2 cycles subsequently. As shown in Fig. 3.21, when the UV source was turned off for the first time, the frequency shift did not return to the initial value after 200 seconds, leading to a slightly larger frequency shift than the following on–off cycles. The reason might possibly be due to the persistent photoconductivity of a semiconductor, i.e. slow relaxation of photo-excited carriers[108]. Fig. 3.21 shows that the maximum frequency shift occurs at the optical wavelength of 365nm, and gradually decreased as the wavelengths become longer, indicating that the acoustoelectric interaction is most effective when the optical wavelength is 365nm, resulting the UV sensor be most sensitive at 365nm. The subsequent on–off cycles in Fig. 3.21 also demonstrates that good repeatability of the UV detector.

When a light source which is outside the UV range illuminates a UV detector, the detector should be insensitive. To demonstrate the insensitivity of the UV sensor, the detector was under 650 nm illumination for several minutes. The optical power density of the 650 nm source was set to 3.5 mWcm^{-2}. Fig. 3.22 shows the response of the UV detector under a 650 nm illumination. The light source was turned on at 10 s and turned off

at 120 s, and the figure indicates that the UV detector was insensitive to this wavelength which is outside the UV range. A maximum frequency shift under 650 nm light source was about 3 kHz, corresponding to a noise level when the sensor oscillated in a steady state without UV illumination. In addition, even when the light power at 650 nm was larger, the UV detector remained insensitive.

Next, the response of the UV detector toward different light power densities is also studied. The optical wavelength of the UV source was set to 365 nm. By varying power densities, frequency shifts of UV on–off cycles for three times were recorded. As can be seen in Fig. 3.23, maximum frequency shifts are 44, 26 and 12 kHz corresponding to 3.5, 1.6 and 0.5 $mWcm^{-2}$. Average frequency shifts of these measurements are 42 kHz at 3.5 $mWcm^{-2}$, 24 kHz at 1.6 $mWcm^{-2}$ and 12 kHz at 0.5 $mWcm^{-2}$, respectively. When light intensity increases, more electron–hole pairs can be generated and thus the acoustoelectric effect is stronger, resulting in larger frequency shift. Experimental values show that this UV detector can clearly tell the differences in UV intensities.

Response time is also important when discussing the performance of a UV detector. To further demonstrate the fast response time of the UV detector, frequency shifts after the UV source being switched on for a short period were measured. Different power densities of 0.5, 1.6 and 3.5$mWcm^{-2}$ were set. Fig. 3.24 shows the responses of the UV detector under 365 nm UV illumination for 10 s. As can be seen in the figure, the maximum frequency shifts are 19 kHz at 3.5 $mWcm^{-2}$, 10 kHz at 1.6 $mWcm^{-2}$ and 4 kHz at 0.5 $mWcm^{-2}$. Average frequency shifts of these measurements are 18, 9 and 3 kHz corresponding to 3.5, 1.6 and 0.5 $mWcm^{-2}$. The UV detector can tell the differences of various light power densities in a short period. Moreover, in the previous study[75], the maximum frequency shift of an AlGaN-based SAW oscillator was less than 3 kHz with a power of 1–2 mW cm^{-2} at 10 s after 365 nm illumination. Under same period of UV

illumination, the response of ZnO-nanorod based UV detector is much larger than the AlGaN-based SAW UV sensor.

Briefly, the presented UV detector utilizing the ZnO nanorod-based dual-channel SAW oscillator has good sensitivity, good repeatability, and fast response and it can exclude environment fluctuations.

3.4.3 Calculation of ZnO Conductivities Using the Acoustoelectric Effect

The performances of an UV detector such as sensitivity and repeatability were discussed in last section. In previous studies, electric properties of the sensing film were not compared with the theoretical model. In this section, the conductivities of the ZnO sensing material are calculated based on both the measurement results and the acoustoelectric interaction model.

In chapter 2, the relation between velocity difference and conductivity is derived, and the relation is

$$\frac{\Delta v}{v_o} = \frac{\Delta f}{f} = \frac{K_{eff}^2}{2} \frac{1}{1+(\sigma_d / \sigma_m)^2} \tag{3.1}$$

From chapter 2, the coupling coefficient of 128°YX-$LiNbO_3$ is 5.458%. The SAW phase velocity on a free surface of lithium niobate v_o is calculated and the value is 3978.98 m/s. The material constant σ_m is $1.9077 \times 10^{-6} \Omega^{-1}$. The conductivity of the ZnO sensing material σ_d can be found from Eq. (3.1). First, the change in SAW velocity induced by conductivity variation can be calculated through measuring the frequency shifts. Once the values of velocity difference Δv are found, the conductivity of ZnO sensing material can be found by substituting v_o, K_{eff}^2 and σ_m into Eq. (3.1).

Last section states that average frequency shifts under 365 nm illuminations are 42 kHz at 3.5 $mWcm^{-2}$, 24 kHz at 1.6 $mWcm^{-2}$ and 12 kHz at 0.5 $mWcm^{-2}$. The

corresponding average velocity variations with different 365nm power densities are marked in Fig. 3.25. The acoustoelectric effect indicates that the larger conductivity of the surface causes the decrease of the SAW velocity. Here, Δv means the difference between the velocity under UV illumination and the velocity of which the conductivity of the surface is infinity (short condition).The normalized velocity differences $\Delta v / v_o$ are 0.011068 at 0.5mWcm^{-2}, 0.010993 at 1.6mWcm^{-2} and 0.010878 at 3.5mWcm^{-2} respectively. Fig. 3.25 shows that when the power density is larger, the average velocity difference is smaller because the perturbed velocity is approaching to the velocity of short condition.

Substituting the normalized velocity differences $\Delta v / v_o , v_o$, K_{eff}^2 and σ_m into Eq. (3.1), the average sheet conductivities of ZnO under different power densities of 365nm illuminations for a period of time can be obtained, and the values are marked in Fig. 3.26. The average sheet conductivities are $2.28\times10^{-6}\Omega^{-1}$ at 0.5mWcm^{-2}, $2.3\times10^{-6}\Omega^{-1}$ at 1.6mWcm^{-2} and $2.32\times10^{-6}\Omega^{-1}$ at 3.5mWcm^{-2}. As can be seen, the average conductivity of ZnO becomes larger when the light power density increases. And the larger conductivity results in smaller SAW velocity. This phenomenon is consistent with the theory of the acoustoelectric interactions.

In the UV detector system, the range of calculated average-conductivities is marked as the dark-grey region in Fig. 3.27, which is in the range of the conductivities where the acoustoelectric interactions are effective, as the light-grey region marked in Fig. 3.27. The average conductivities where the acoustoelectric interactions are effective ranges from $0.4\,\sigma_m = 7.63\times10^{-7}\Omega^{-1}$ to $4\,\sigma_m = 7.63\times10^{-6}\Omega^{-1}$. The measured conductivities are all around $2\times10^{-6}\Omega^{-1}$. In this case, by increasing conductivities of ZnO, larger effect of acoustoelectric interactions can be further obtained. Therefore, the inversed calculation of

ZnO conductivities in this work provides a further design consideration for enhancing the response of a sensor using AE interactions in the future.

In this study, a ZnO nanostructured ultraviolet detector based on a SAW oscillator system was designed and realized. Responses of light wavelengths both inside and outside the UV range were measured. Frequency shifts of varying optical power densities were also recorded. Under a UV source of 365 nm, frequency shifts reached a maximum value of over 40 kHz; on the other hand, the UV detector was insensitive when a light source was not in the UV range. Moreover, frequency shifts was 19 kHz after 365 nm was switched on for 10 s, much larger than the AlGaN/sapphire UV sensor reported previously[75]. Results show that performance of this UV detector such as repeatability, sensitivity, response time and environmental-fluctuation elimination are excellent. The proposed ZnO nanorod-based SAW oscillator system is a promising candidate for UV sensing applications. Furthermore, the average conductivities of ZnO sensing material under a period of UV illuminations were first calculated based on the theoretical acoustoelectric model. Results shows the measured conductivities are in a reasonable range of which the acoustoelectric interaction takes place. This inversed calculation of ZnO conductivities provides a further design consideration for acoustic wave sensors using the AE interactions in the future.

Substrate	ST-cut quartz	Y-cut lithium niobate	128°-cut lithium niobate	Y-cut lithium tantalate
propagation	X	Z	X	Z
velocity	3158	3488	3992	3230
K^2 (%)	0.11	4.5	5.3	0.72
TCD*(ppm/℃)	0	+94	+75	+35

*: Temperature Coefficient of Delay

Table 3.1 Properties of several piezoelectric substrates

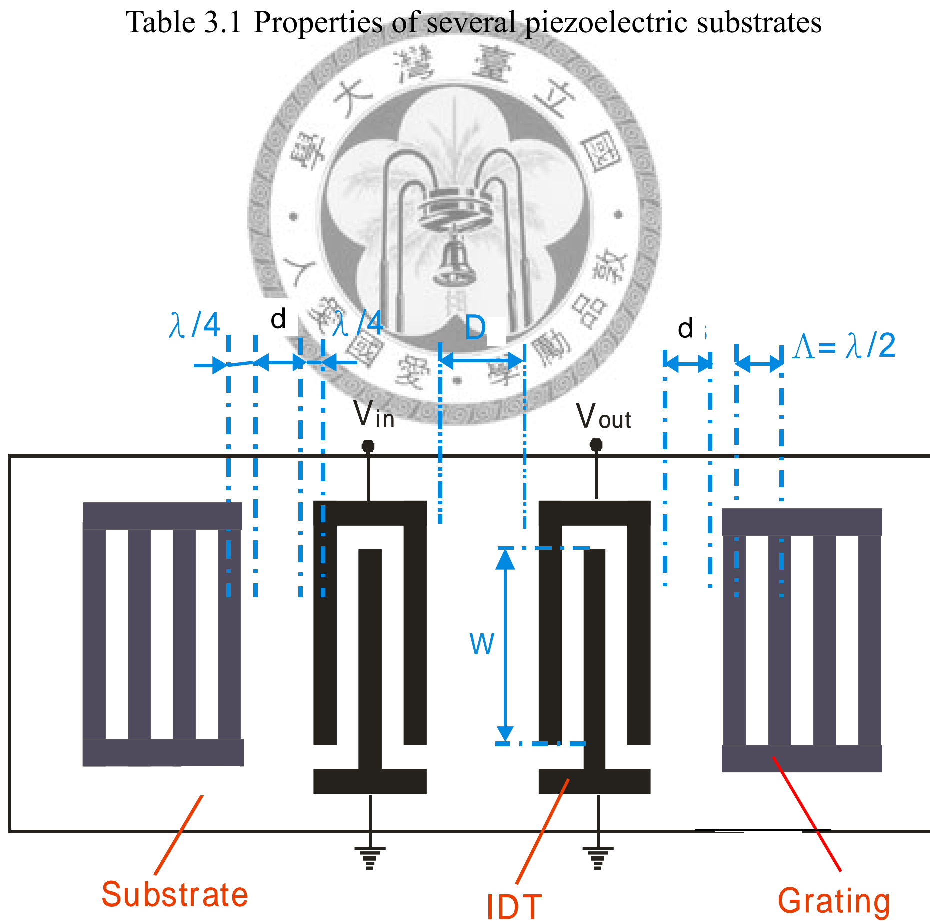

Fig. 3.1 A schematic diagram of a two-port SAW device

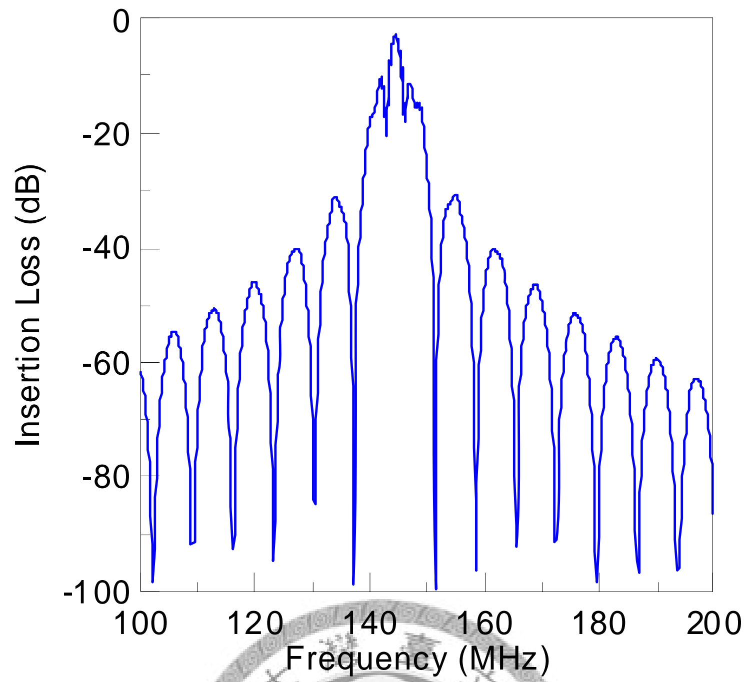

Fig. 3.2 Simulated frequency response of a two-port SAW device

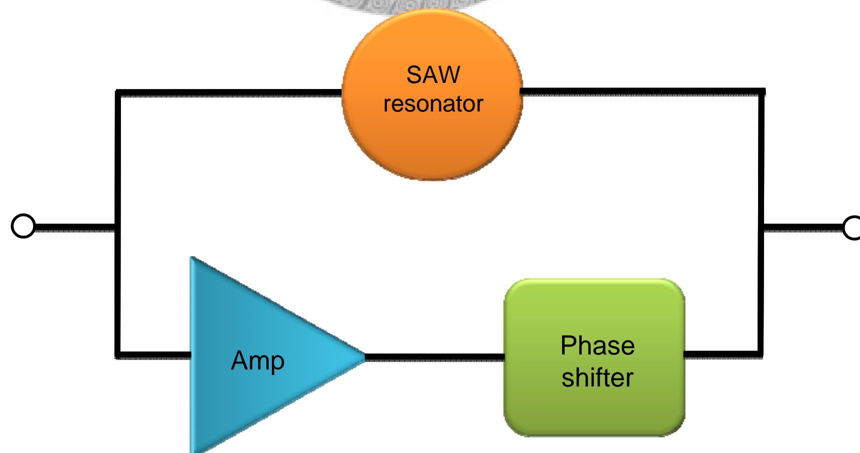

Fig. 3.3 Configuration of a SAW-based oscillating loop

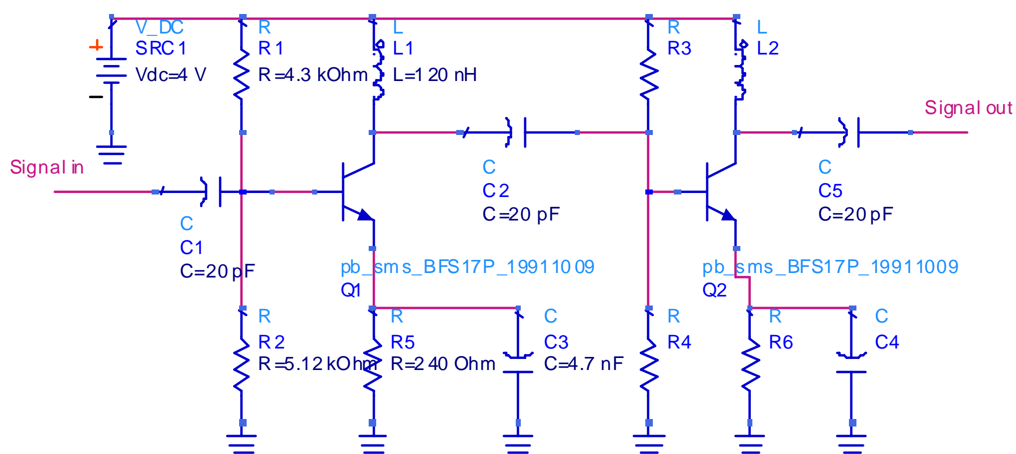

Fig. 3.4 Layout of an amplifier circuit

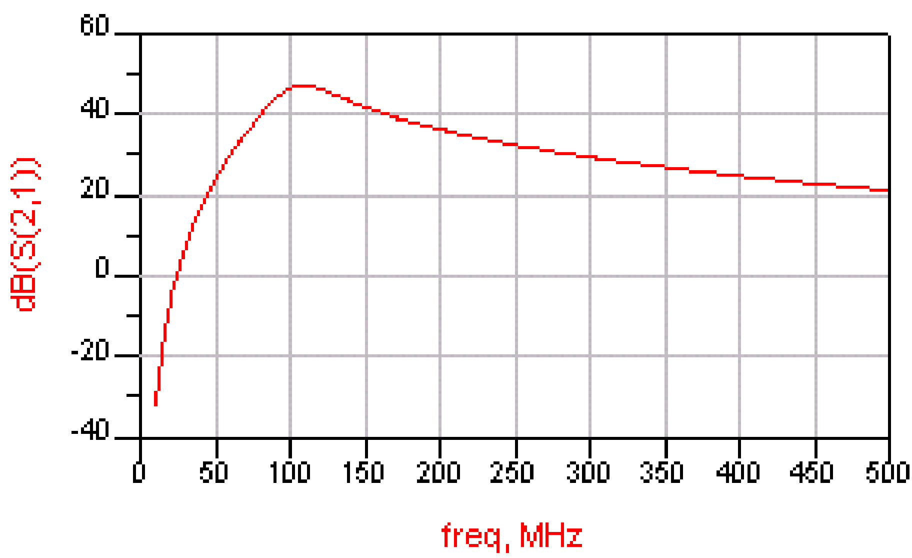

Fig. 3.5 Simulation result of the amplifier response

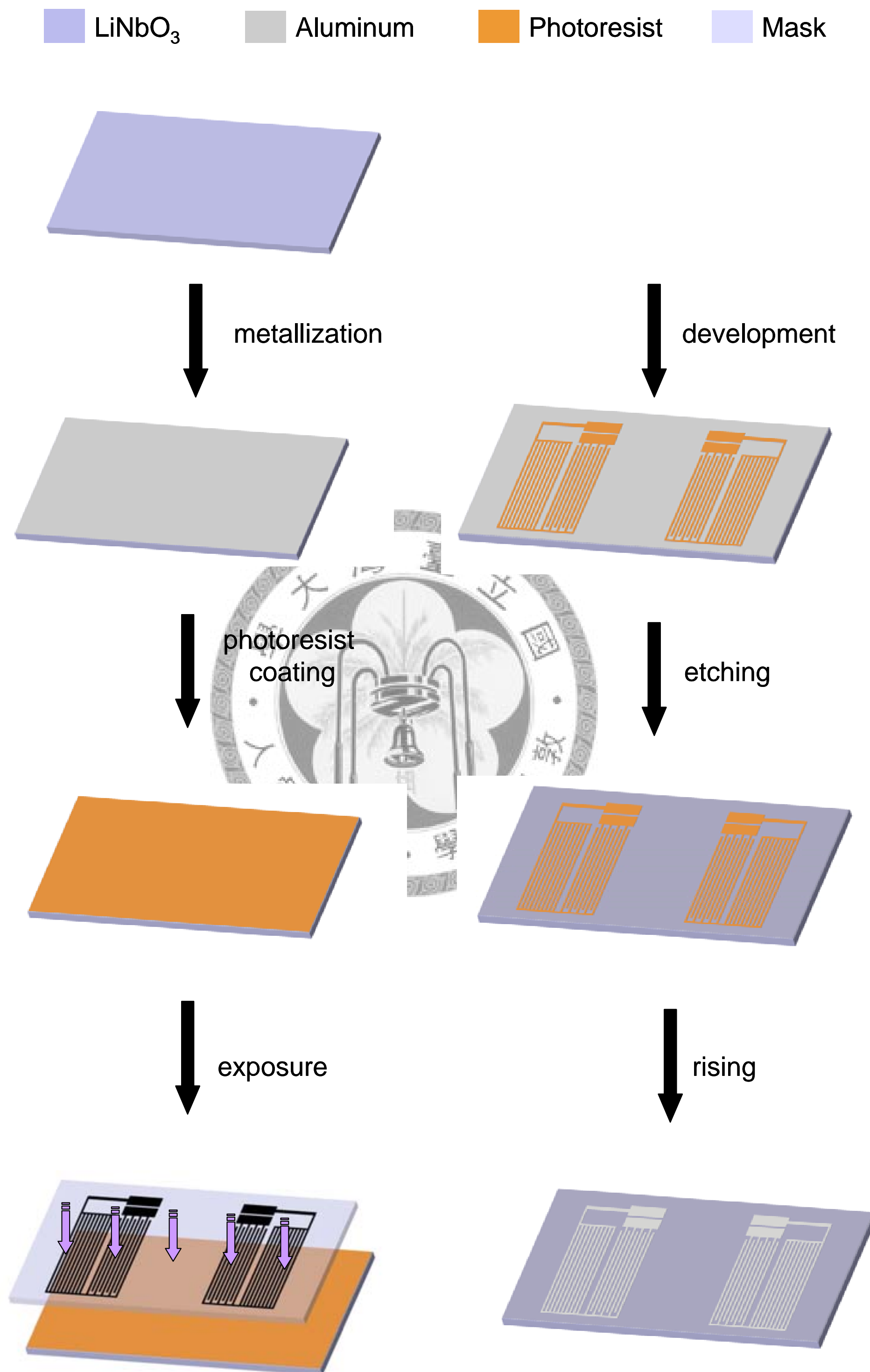

Fig. 3.6 Flow chart of a SAW resonator fabrication process

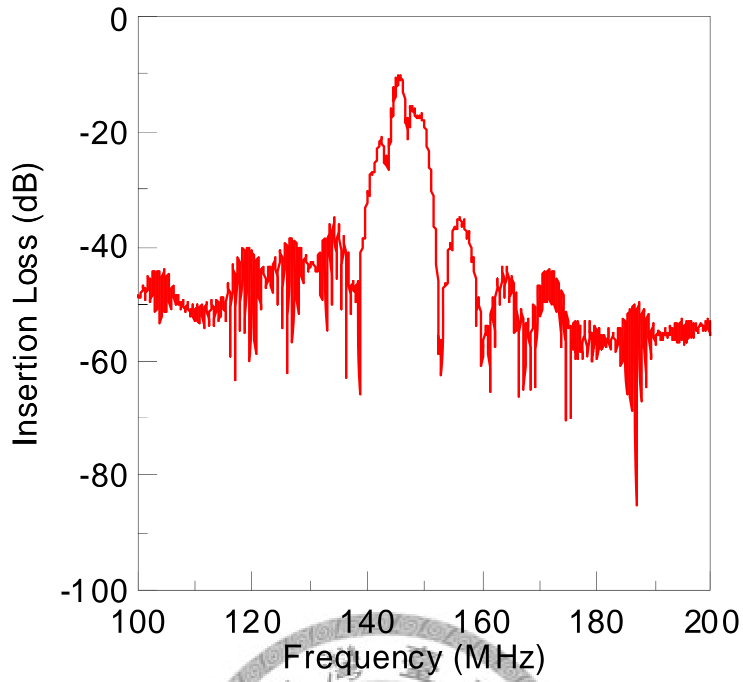

Fig. 3.7 Frequency response of a two-port SAW device

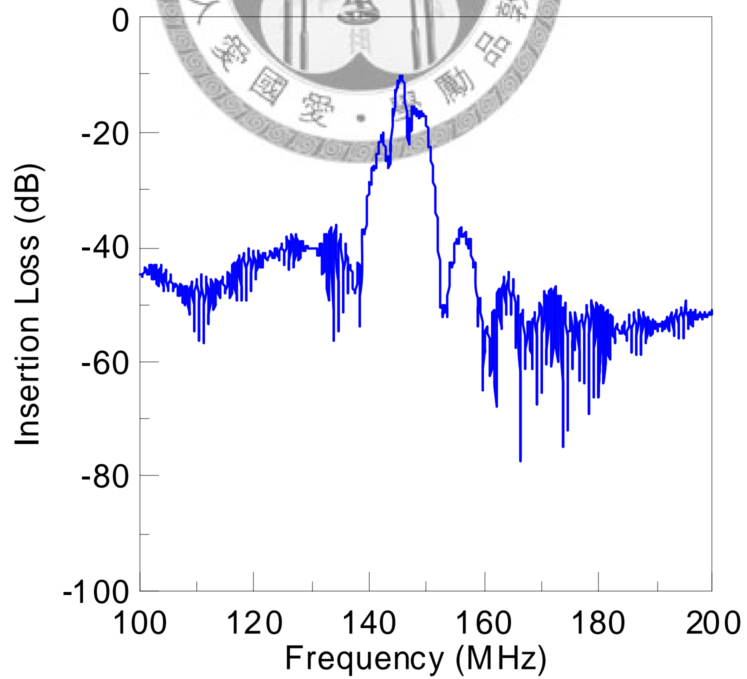

Fig. 3.8 Frequency response of a SAW device with ZnO film

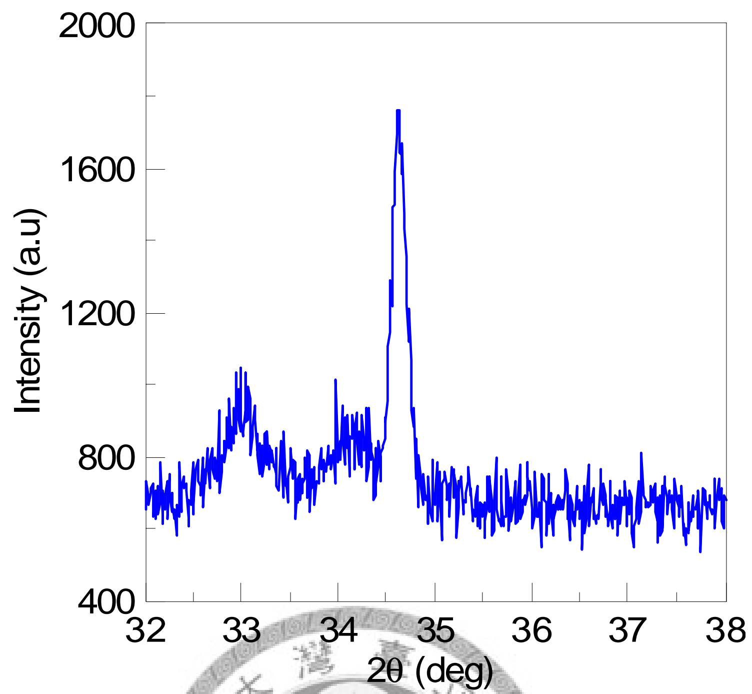

Fig. 3.9 The XRD pattern of ZnO film

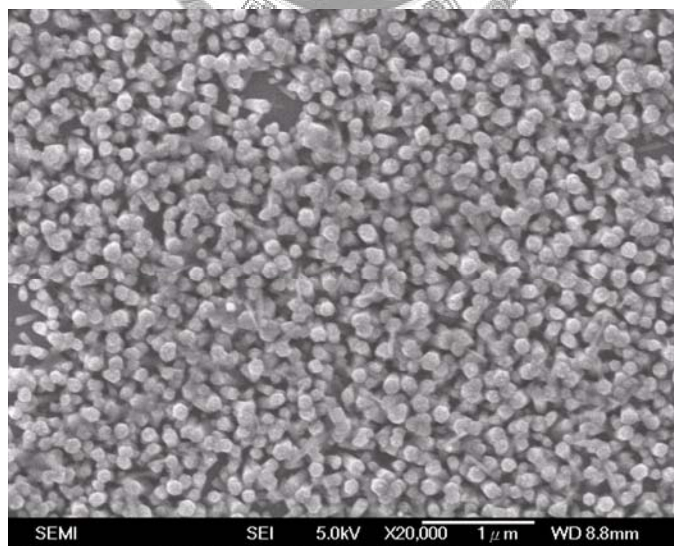

Fig. 3.10 A top-view SEM image of ZnO nanorods

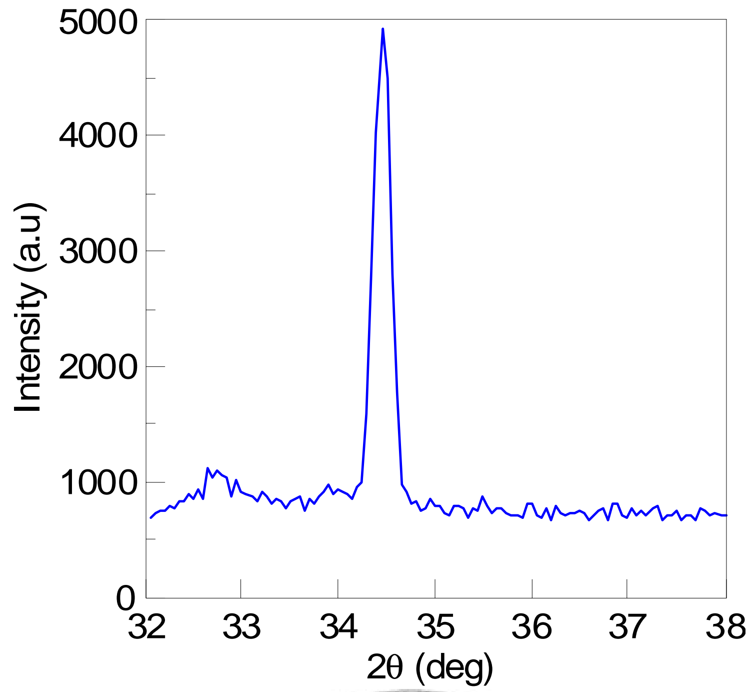

Fig. 3.11 The XRD pattern of ZnO nanorods

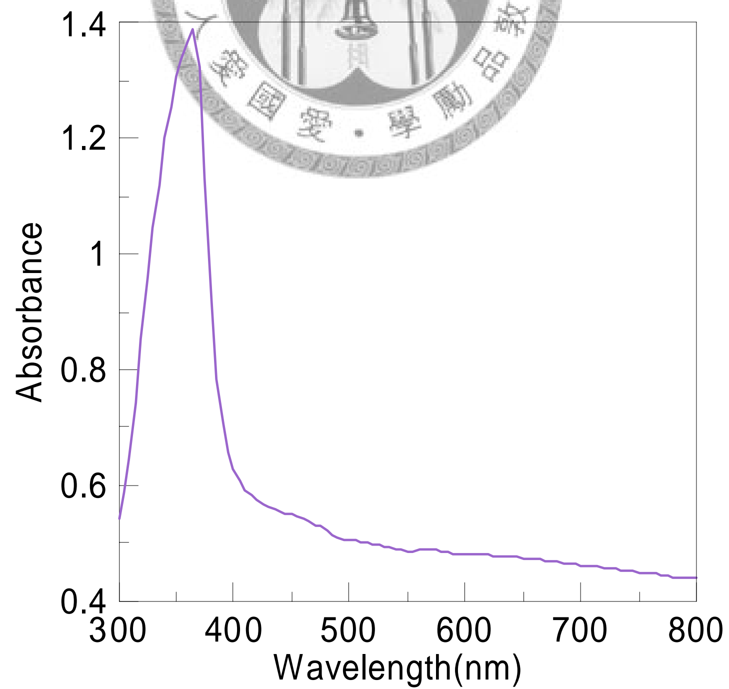

Fig. 3.12 A UV-Vis absorption curve of ZnO nanorods

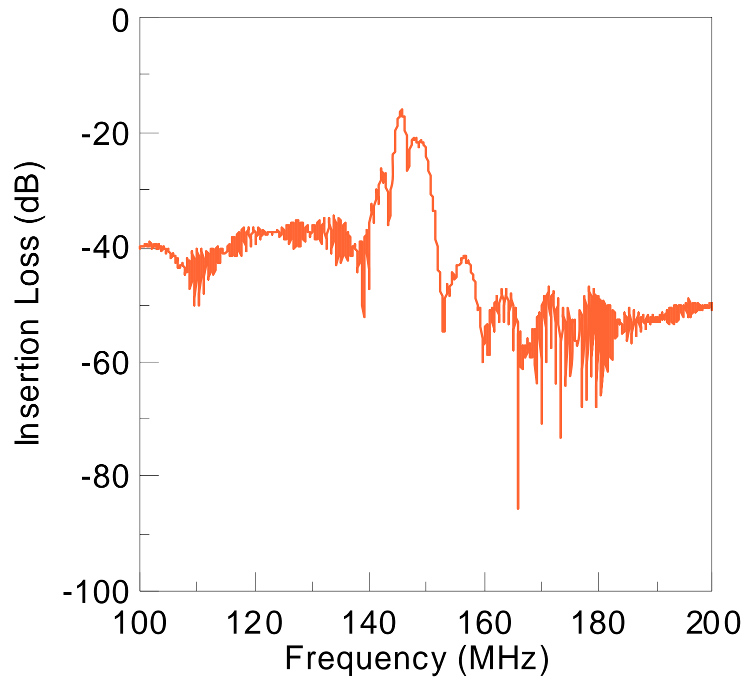

Fig. 3.13 Frequency response of a SAW device with ZnO nanorod

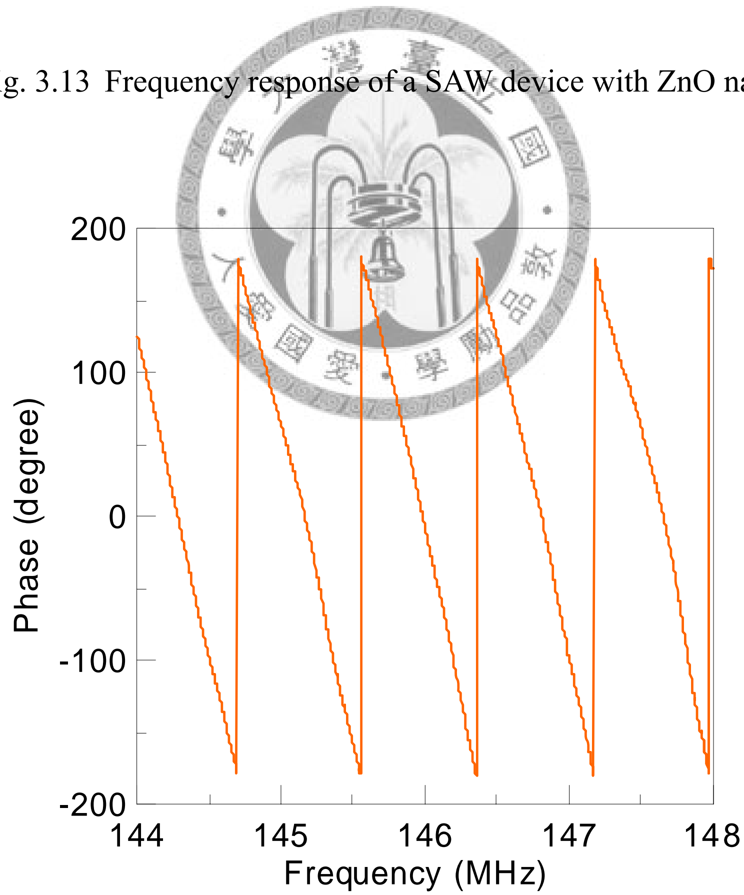

Fig. 3.14 Phase of a SAW device with ZnO nanorod

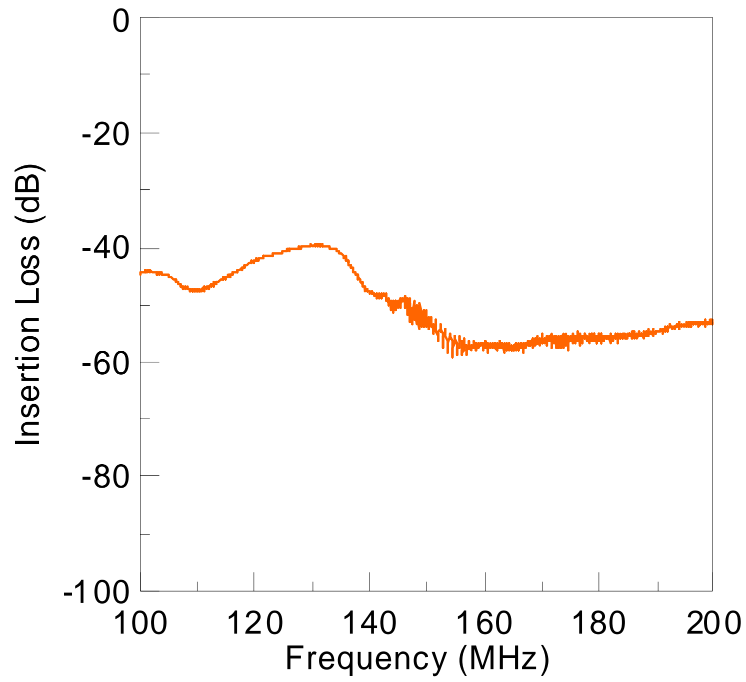

Fig. 3.15 Frequency response of a SAW device with over-height ZnO nanorods

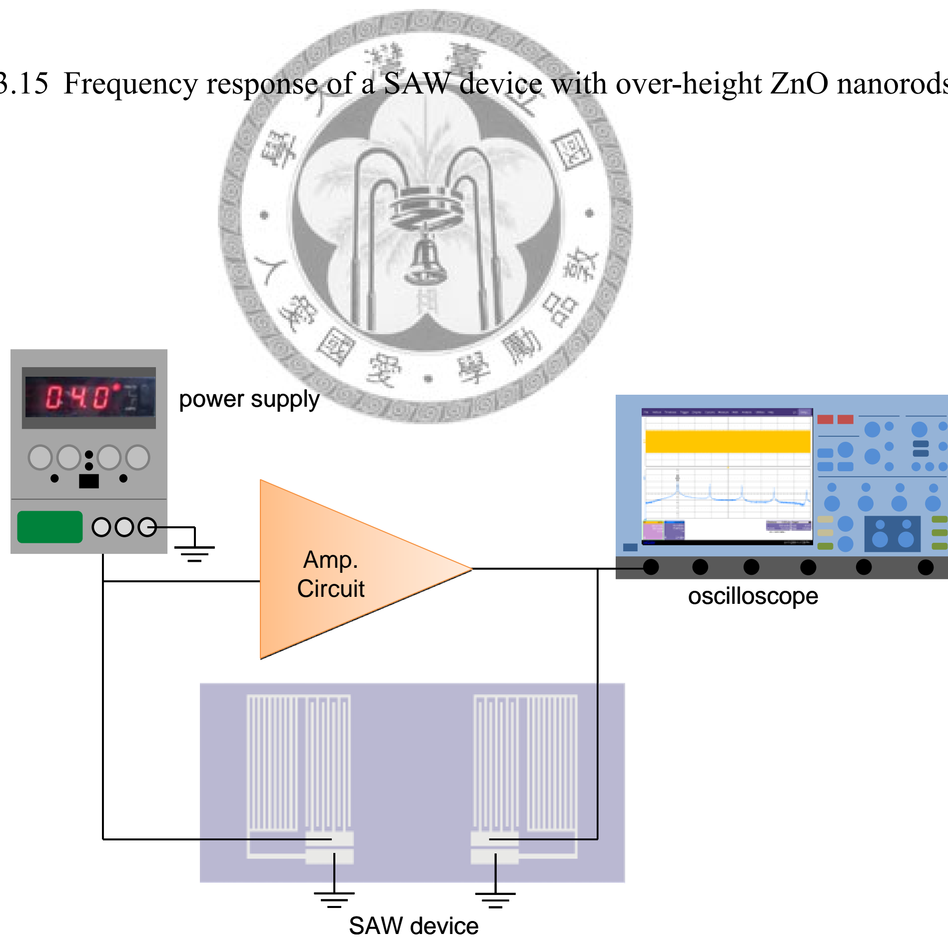

Fig. 3.16 A schematic of a two-port SAW oscillator

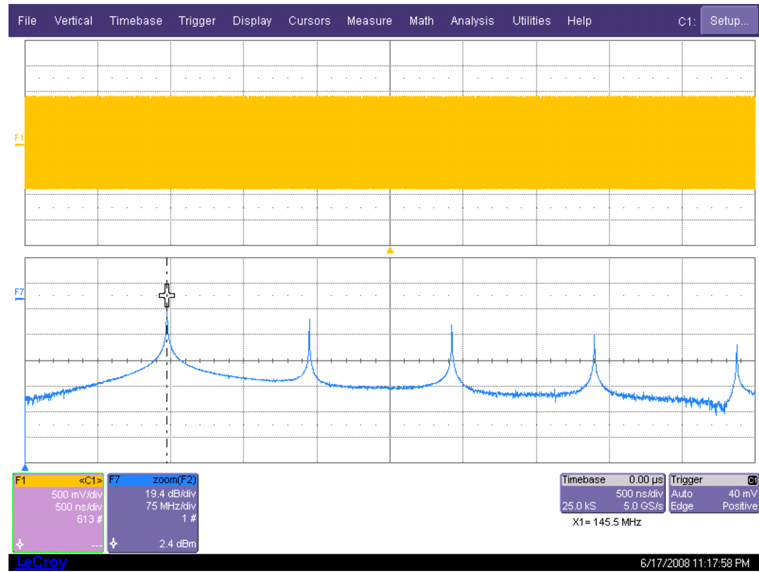

Fig. 3.17 Signal of a two-port SAW oscillator

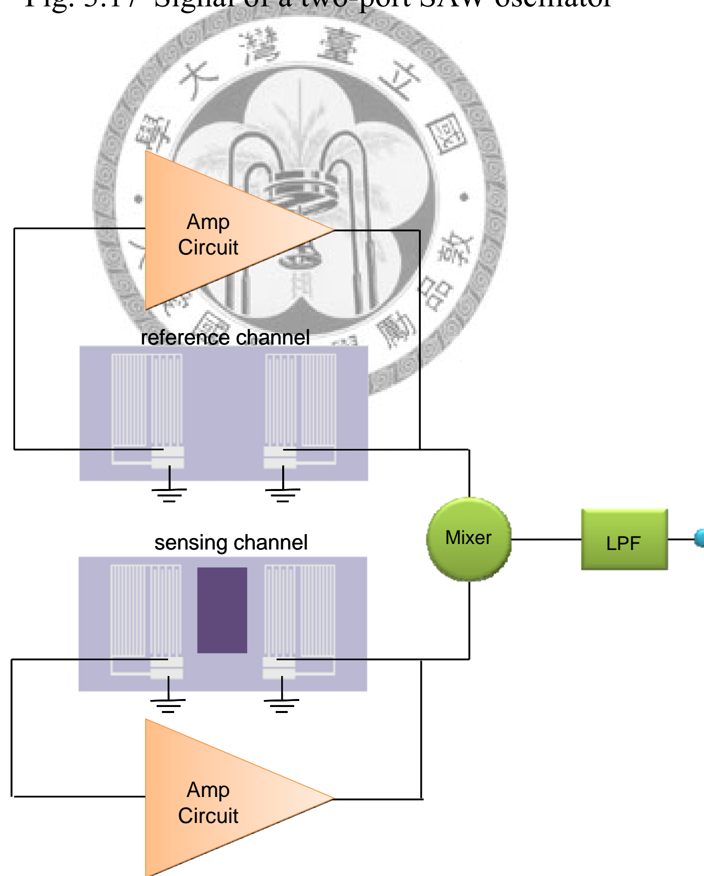

Fig. 3.18 A dual-channel SAW oscillator system

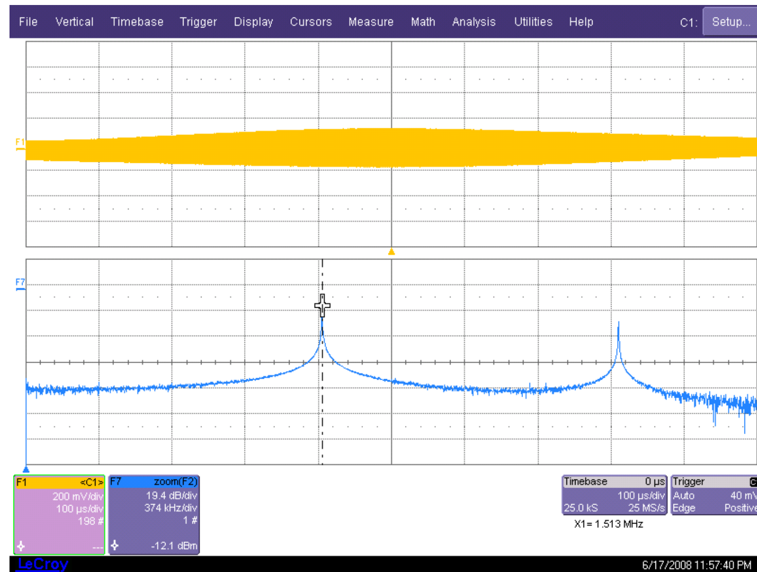

Fig. 3.19 Frequency and time domain signal of the oscillator system

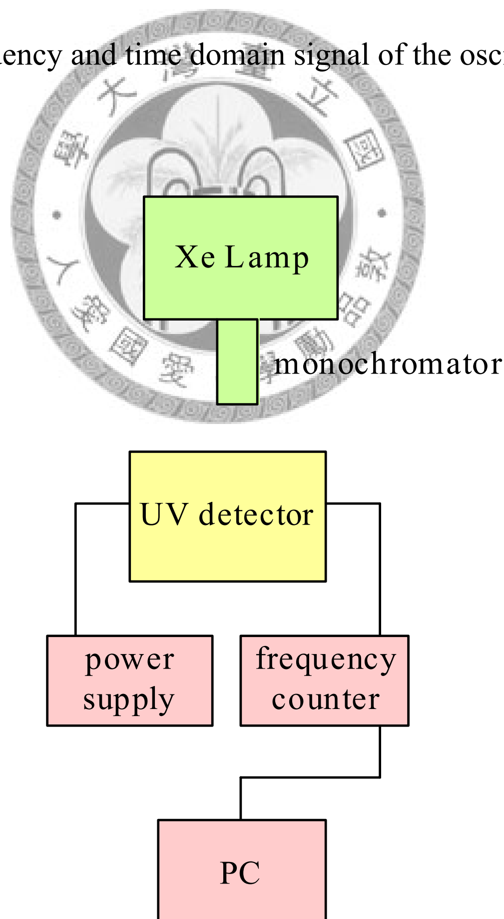

Fig. 3.20 Experimental setup of a UV sensing system

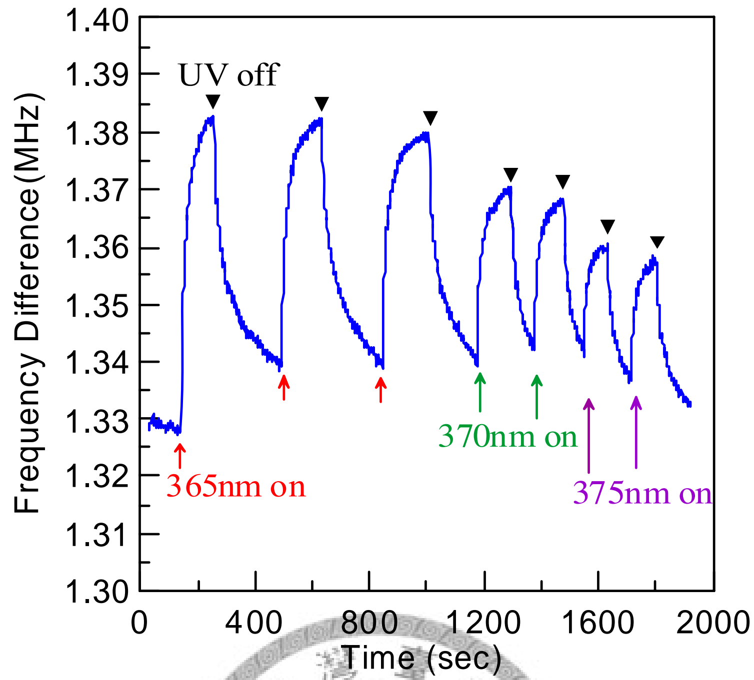

Fig. 3.21 Response of a UV detector under UV illumination

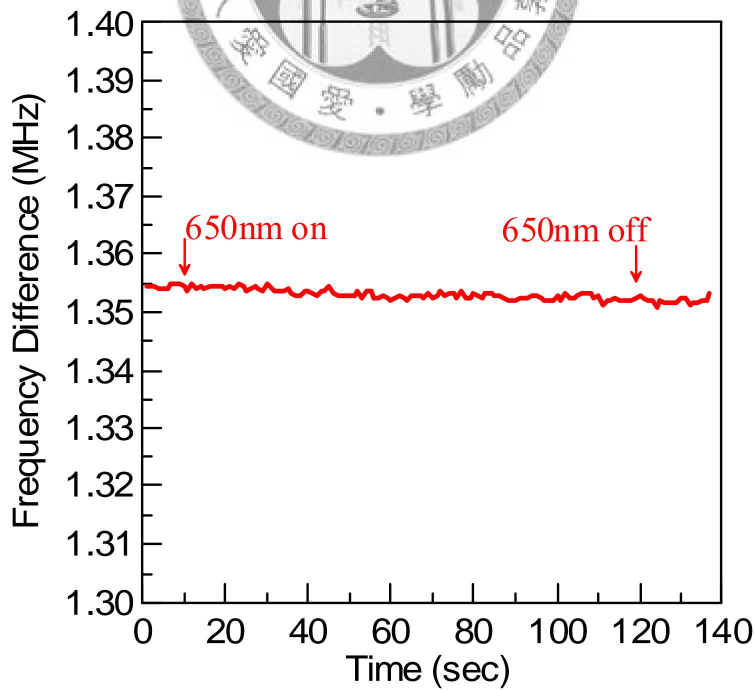

Fig. 3.22 Response of a UV detector under 650 nm illumination

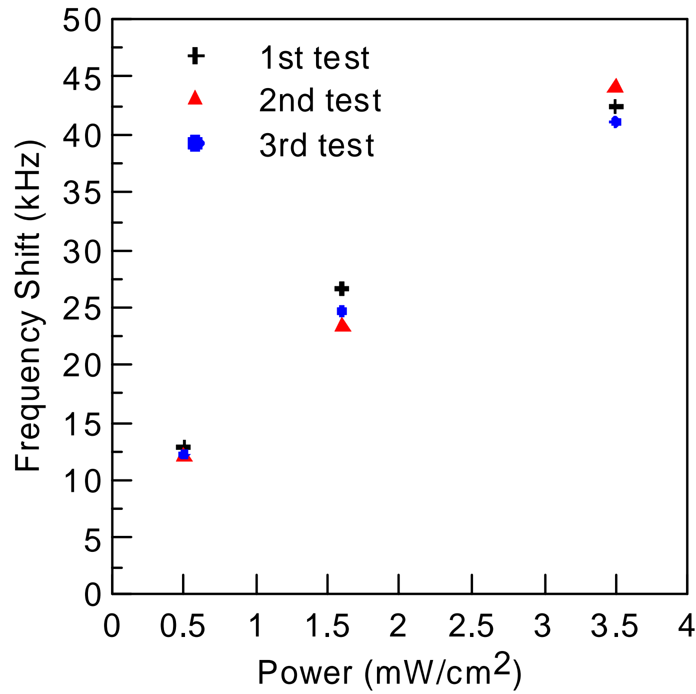

Fig. 3.23 Response of a UV detector toward different light power densities

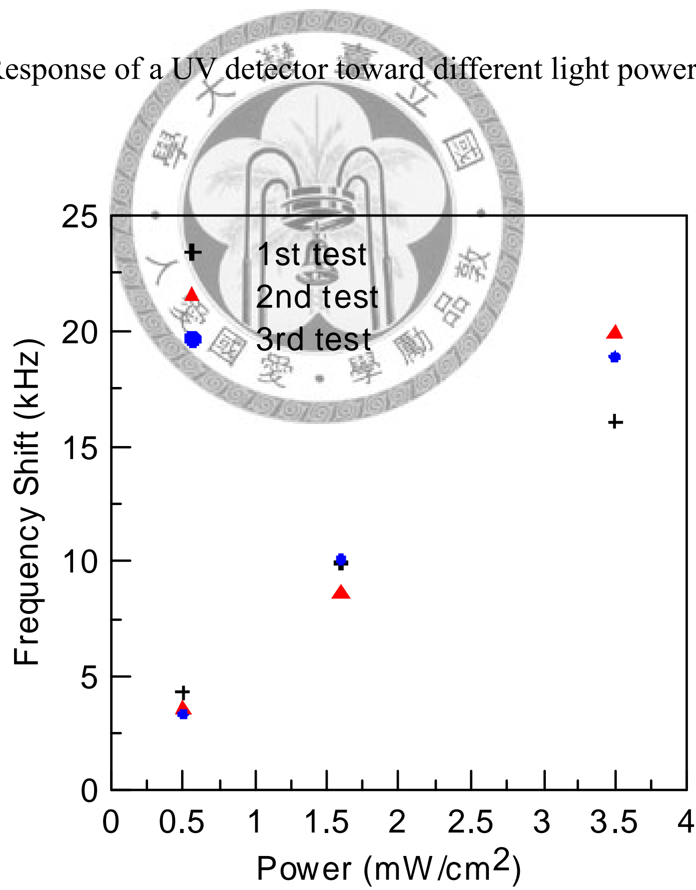

Fig. 3.24 Response of a UV detector under 365nm UV illumination for 10 s

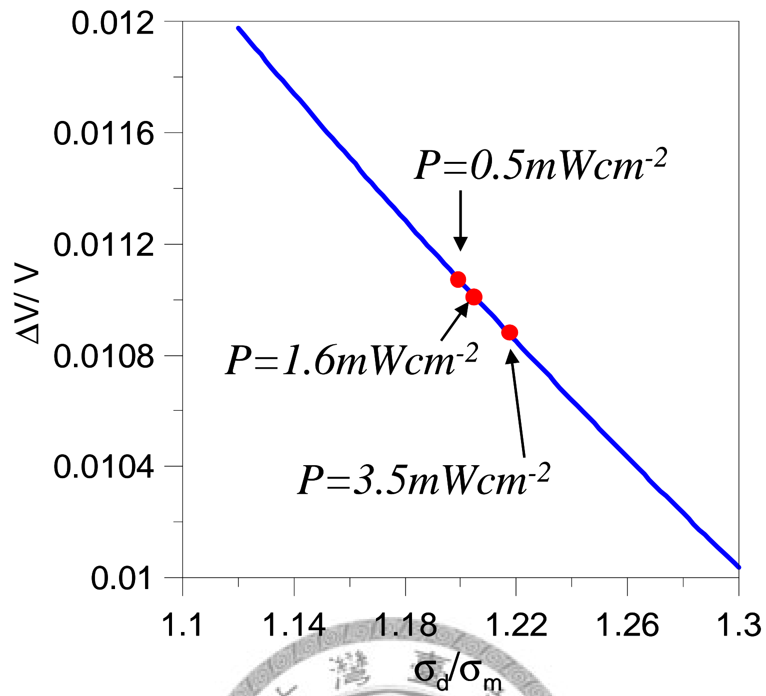

Fig. 3.25 Velocity shifts of different 365nm power densities

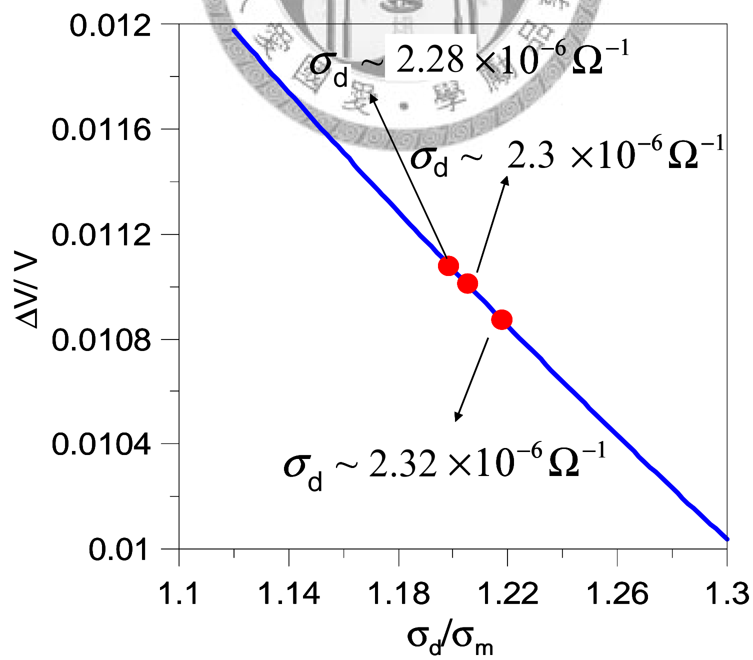

Fig. 3.26 Average sheet conductivities under 365nm illuminations for a period of time

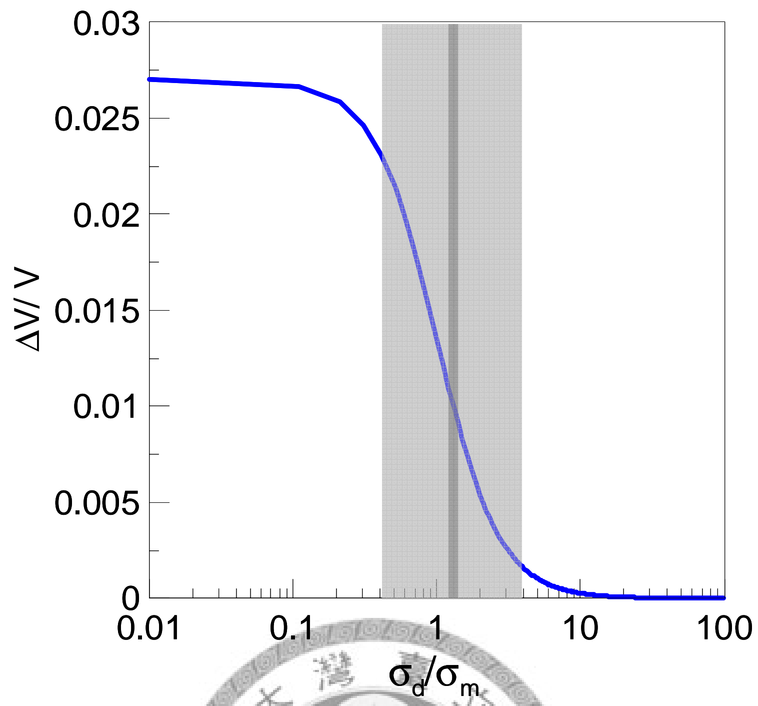

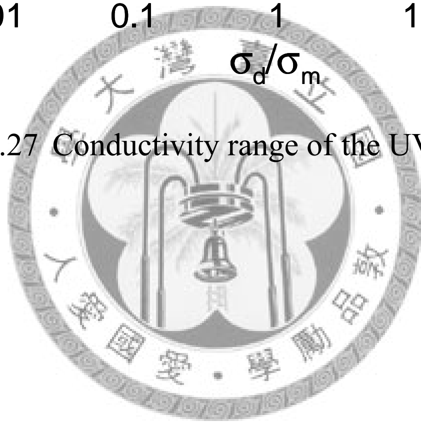

Fig. 3.27 Conductivity range of the UV detector

Chapter 4 A Silicon-based Lamb Wave Sensor for Ultraviolet Detection

Characteristics of Lamb wave propagation due to AE interactions have been introduced in Chapter 2. To demonstrate the effect of AE interactions on Lamb wave propagation, a silicon-based ZnO Lamb wave UV detector is realized for the first time. Section 4.1 points out important considerations when designing a silicon-based ZnO Lamb wave device. Then, fabrication processes of micro two-port Lamb wave devices which are fabricated on a silicon substrate are introduced in Sec. 4.2. Sec. 4.3 shows the measurement results of silicon-based acoustic wave devices before setting up an ultraviolet sensing system. In Sec. 4.4, a Lamb wave UV sensing system is constructed, and performances of Lamb wave microsensors due to AE interactions are measured and discussed.

4.1 Design of a Silicon-based Lamb Wave Device

Lamb wave is a type of elastic waves which propagates in plates of finite thickness. Similar to bulk and surface waves, Lamb waves can be used to detect various changes such as mechanical, pressure, biological/chemical, mass/density and thermal. In recent years, Lamb wave devices have shown advantages of being sensors.[81,83,109] A number of Lamb wave sensors have been made on silicon because by combining CMOS and MEMS technologies, silicon-based sensors and electric circuits can easily be integrated into a single chip. In this research, a Lamb wave device fabricated on silicon wafer is adopted as a sensor to reveal the AE effect. This section introduces design considerations of a Lamb wave device basically consisting of ZnO film and silicon.

When realizing a silicon-based Lamb wave device, a ZnO film and IDTs are deposited and

patterned on a silicon wafer first, as shown in Fig. 4.1, then the silicon wafer are etched to the require thickness to form a Lamb wave device, as schematically shown in Fig. 4.2. Finally, a Lamb wave device consisting only of ZnO/nitride membrane, as shown in Fig. 4.3, can be fabricated by etching 300 μm-thick silicon. To assure successful excitation of IDTs, excitation efficiency of the surface wave device shown in Fig. 4.1 is also considered. Therefore, when designing a Lamb wave device, numerical simulations of surface wave propagations are discussed first. This section divides into two parts; the first part shows the phase velocity and coupling coefficient of a ZnO/silicon SAW device, and the second part gives the dispersion relations of Lamb wave phase velocity and coupling coefficient.

4.1.1 Dispersions of a Si-based Surface Wave Device

When realizing a Lamb wave device, the line width of IDTs, i.e., the wavelength of acoustic wave, needs to be determined first. In this research, several wavelengths are designed, and the corresponding frequencies and velocities can thus be given from the calculated dispersion curves. To confirm the success fabrication of IDTs, measurement of SAW signal before the silicon is etched to the required thickness is needed. Therefore, the corresponding SAW frequency and coupling coefficient is calculated as a comparison for further experimental results. Herein a ZnO/Si_3N_4/Si layered structure is discussed.

Velocity and coupling coefficient of a ZnO/ Si_3N_4/Si layered structure, as shown in Fig. 4.1, are calculated based on the transfer matrix method presented by Honein et al. in 1991[88] and Wu and Chen in 2002[89]. Fig. 4.4 shows the SAW velocity dispersions of a ZnO/ Si_3N_4/Si layered structure with different nitride thickness. As shown in the figure, in lower and higher frequency regions, velocity increases as silicon nitride becomes thicker. When the frequency is around 200-300 MHz, velocity variations due to varied nitride thickness are small. Fig. 4.5 indicates coupling coefficients of a ZnO/ Si_3N_4/Si layered structure with

various nitride thickness. As shown in this figure, the coupling coefficient becomes smaller when the thickness of nitride increases. In this research, designed wavelengths range from 8-12 μm, as shown in Table 4.1, and the corresponding SAW frequencies range from 300 to 600 MHz with different nitride thickness. In the designed wavelengths and the corresponding frequencies, the coupling coefficients are larger than 0.05%, which indicates that under these designed wavelengths, the SAW signals can be successfully generated. Moreover, as a support membrane and also as a stop layer for silicon etching, the thickness of silicon nitride can not be too small. Thus, a 1 μm thick Si_3N_4 is chosen as the support membrane.

4.1.2 Design Consideration of a Si-based Lamb Wave Device

In the previous section, SAW characteristics of ZnO/ Si_3N_4/Si structure are discussed. Under the choice of 1 μm thick Si_3N_4, the SAW signal excitations can be successful based on numerical simulations. If the thickness of silicon is etched such that the order of the whole structure is comparable with designed wavelengths (8~12 μm), the excitation efficiencies are also discussed. Fig. 4.6 is velocity dispersions of SAW and A_0 mode in a ZnO/ Si_3N_4/Si structure with different thickness of silicon. Fig. 4.6 shows that when the thickness of silicon decreases, the velocity slows down, while at higher frequencies, the Lamb wave velocities approach to SAW no matter how thick the silicon is. This phenomenon results from that as the thickness of silicon increases, the whole structure becomes stiffer and the velocity increases.

Fig. 4.7 shows coupling coefficients of ZnO/Si_3N_4/Si structure with different thickness of silicon. The red dashed-line indicates the coupling coefficient of SAW. The figure shows that when thickness of silicon is in the range of 5 to 10 μm, coupling coefficients of A_0 modes only differ slightly from the one of SAW. At most frequencies the

coupling coefficients are even smaller than the one of SAW. Only when frequencies are lower than 200MHz, all coupling coefficients of A0 modes are larger than that of SAW. Therefore, when the Lamb wave device is composed of ZnO/ Si_3N_4/Si, coupling coefficients of A_0 mode are not always larger than that of SAW. Because the Lamb wave UV detector utilizes acoustoelectric effect, which strongly depends on coupling coefficient. The Lamb wave device is composed of ZnO/ Si_3N_4/Si discussed above is not a good choice for UV detection. The performance of a ZnO/ Si_3N_4/Si Lamb wave UV detector will be discussed in Sec. 4.4 .

Now, consider a Lamb wave device consists of ZnO and Si_3N_4 membrane, which means that silicon is all etched away, as shown in Fig. 4.3. In Fig. 4.8, the bold line shows A_0 mode of Lamb wave dispersion in a ZnO/ Si_3N_4 structure, with 0.5 μm ZnO and 1 μm Si_3N_4. The dashed line is SAW dispersion in a ZnO/Si_3N_4/Si structure. Fig. 4.9 shows coupling coefficients of A_0 mode of Lamb wave and SAW, respectively. Fig. 4.8 shows that phase velocity of A_0 mode of Lamb wave in a ZnO/Si_3N_4 structure is smaller than that of SAW in a ZnO/Si_3N_4/Si structure, which indicates that with a same wavelength, frequency of A_0 mode would be lower than SAW frequency in this case. However, Fig. 4.9 shows that at a constant frequency, coupling coefficients of A_0 mode is much larger than the one of SAW. The coupling coefficient of a ZnO/Si_3N_4 Lamb wave device can even be four times larger than SAW of a ZnO/Si_3N_4/Si structure. Therefore, the advantage of a ZnO/Si_3N_4 Lamb wave device using AE effect is obvious. Large coupling coefficient of a ZnO/Si_3N_4 Lamb wave device is highly suitable for sensing application using the AE effect. To demonstrate this, the performance of a ZnO/ Si_3N_4 Lamb wave UV sensor will be discussed in Sec. 4.4.

In this section, SAW dispersion of ZnO/Si_3N_4/Si structure, Lamb wave dispersion of ZnO/Si_3N_4/Si and ZnO/Si_3N_4 membranes are discussed. Numerical simulations show that

when using the AE effect, a Lamb wave device composed only of ZnO/Si_3N_4 membrane is more suitable for sensing compared with a $ZnO/Si_3N_4/Si$ Lamb wave device. In the following sections, fabrication and measurement of silicon-based Lamb wave devices are discussed. Furthermore, UV detectors based on $ZnO/Si_3N_4/Si$ and ZnO/Si_3N_4 Lamb wave devices are also constructed, measured, and compared.

4.2 Fabrication of a Silicon-based Lamb Wave Device

This section details the manufacturing process of realizing a micro Si-based Lamb wave device.

A Si-based Lamb wave device with micro-scale electrodes can be fabricated through photolithographic process. Fig. 4.10 shows fabrication process and fabrication steps are described as follows.

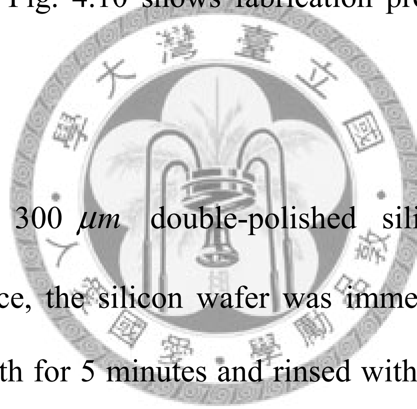

(i) Wafer Cleaning:

The substrate is a 300 μm double-polished silicon wafer. To prevent any contaminants on the surface, the silicon wafer was immersed in acetone for 5 minutes, followed by a methanol bath for 5 minutes and rinsed with deionised water for 5 minutes. Then the wafer was dried by nitrogen gas. Alternatively, the wafer can be immersed in a mixture of three parts of H_2SO_4 and one part of H_2O_2 for cleaning.

(ii) Deposition of silicon nitride layers:

After cleaning the substrate, silicon nitride (Si_3N_4) layers were deposited. The upper Si_3N_4 layer acted as a support membrane for the Lamb wave device and as a stop layer, while the bottom layer served as an etching mask in potassium hydroxide (KOH) solution. In this study, a Low Pressure Chemical Vapor Deposition (LPCVD) system was used to deposit the low-stress Si_3N_4 at 850℃. The thickness of Si_3N_4 was 1 μm. The reason why LPCVD was adopted rather than Plasma-Enhanced Chemical Vapor Deposition (PECVD)

is that the Si_3N_4 film deposited by LPCVD is much more dense and stronger than the one deposited by PECVD.

(iii) Deposition of ZnO thin film:

A ZnO thin film, functioning as a piezoelectric medium which enables Lamb wave excitation and as a sensing material, was deposited on a Si_3N_4/Si structure by a radio-frequency magnetron sputtering system. Before sputtering, the vacuum pressure of the sputtering system was pumped down to the order of 10^{-6} Torr. A 4” ZnO target is with a purity of 99.99%. A 15 minute pre-sputter process was performed to remove the dirt of the surface of the ZnO target. This pre-sputter process can avoid dirt adhere to the surface of the target which may result in unstable growth of the ZnO thin film. The sputtering conditions were 150 W for 3.5 hours, with 25% Ar and 45% O_2. And the substrate temperature was 200℃. Under these sputtering parameters, a 0.5 μm-thick ZnO film was deposited on a Si_3N_4/Si structure.

(iv) Coating of Photoresist:

By using a Laurell spin coater, positive photoresist (EPG-512) was spun at 1000rpm for 5 seconds, 1500 rpm for 5 seconds and 3000 rpm for 30 seconds. Using these parameters, a 1 micron photoresist layer was formed. Next, to drive off excess solvents, the photoresist-coated wafer was prebaked on a hotplate at 90℃ for 90 seconds. Then the photoresist-coated wafer was cooled to room temperature before exposure process.

(v) Exposure and Developing:

The exposure time of the wafer coated with photoresist was 10 seconds by using a Karl Suss double side mask aligner. Then the exposed wafer was developed in a EPD-100 developer, followed by a deionised water. It is noted that the timing of exposure and developing should be precisely controlled to avoid under-developing or over-developing. The pattern was checked by careful inspection under a microscope.

(vi) Metallization:

Fabrication process of this Lamb wave structure utilizes lift-off technique, thus hard bake of the photoresist was not employed before the metal thin-film evaporation. Moreover, before metallization, the wafer with patterned photoresist must be carefully protected to prevent dirt from adhering to the wafer surface. Here, aluminum is adopted as metal film to form IDTs. Aluminum thin film was deposited on the patterned substrate by E-beam evaporation and the thickness was 150nm.

(vii) Lift-off and Removal of Photoresist:

After evaporation, aluminum thin film, which was blanket-deposited all over the substrate, covered the photoresist and areas where the photoresist has been cleared. During the lift-off process, the photoresist and the Al thin film deposited above it were removed with acetone. Only the Al thin film which was deposited directly on the substrate stayed, thus the electrode pattern was formed. After lift-off, the wafer was rinsed by methanol to prevent any residual acetone on the wafer. Then the wafer was rinsed by deionised water for 5 minutes to remove methanol and dried by nitrogen gas.

After the lift-off process, SAW frequency response of a ZnO/Si3N4/Si layered structure can be measured. If the signal is good, the following process can be done. Otherwise, the processes described above should be repeated to achieve successful fabrication. The measurement results are shown in Sec 4.3.

(viii) Coating of Photoresist:

In the following steps, the back side of the wafer surface was patterned. Positive photoresist (SPR 220) was spun at 500rpm for 5 seconds, 1500 rpm for 10 seconds and 3000 rpm for 30 seconds By a Laurell spin coater. Using these parameters, a 5 micron photoresist layer was formed. Next, the photoresist-coated wafer was prebaked on a hotplate at 90℃ for 5 minutes. Because the developer etches aluminum, the front side of

the wafer surface with IDTs pattern needed protection. Therefore, a EPG-512 photoresist was spun on the top side of the wafer surface and the prebake time was 90 seconds at 90℃. The double side photoresist-coated wafer was cooled down to room temperature before it was exposed.

(ix) Exposure and Developing:

This step defined the region where the Si_3N_4 would be etched. In this step, a double side mask aligner was needed to align the marks of the front and back side of the wafer surface. After aligning, the exposure time of the wafer coated with SPR 220 was 40 seconds by using a Karl Suss double side mask aligner. Then the exposed wafer was developed in a TMAH developer, followed by deionised water. The development time was about 1 minute and 30 seconds.

(x) Etching of Si_3N_4 film:

Before etching the Si_3N_4 film, a post bake of the wafer was performed in an oven at 90℃ for 20 minutes. The post bake supported the formation and hardening of the required shape of the photoresist. After post bake and cooling, the Si_3N_4 film unprotected by the photoresist was then dry-etched by Reactive Ion Etching (RIE) technique. The RIE machine used chemically reactive plasma which was generated under low pressure by an electromagnetic field to remove material, usually oxide and nitride deposited on wafers. High-energy ions from the plasma attacked the wafer surface and etched the Si_3N_4 film unprotected by the photoresist. For etching Si_3N_4, the flow rate of CF_4 and O_2 were 30sccm and 3 sccm, respectively. The power was 70W, and the reactive time was 21 minutes. After etching, the wafer was rinsed in acetone, methanol and deionised water for 5 minutes respectively to remove the photoresist, and dried by nitrogen gas.

(xi) Wet Etching of Silicon:

The Si_3N_4 film not etched by RIE was used as a mask for silicon etching. Only the

region where silicon is not protected by the Si_3N_4 film was etched. Here a potassium hydroxide (KOH) solution was used as the etchant. The back side of the wafer was immersed in a 30% KOH solution at 80℃ for 3 hours and 30 minutes while the front side of wafer was protected by a home-made Teflon mask. The etching rate was 74 $\mu m/hr$. The thickness of silicon after etching was in a range of 40-50 μm due to non-uniform etching.

(xii) Etching of Silicon by ICP:

The thickness of silicon after 3.5hr KOH etching ranged from 40-50 μm. The last step of the whole fabrication process was to etch silicon to the desired thickness. The designed wavelengths were 8-12 μm, hence the silicon thickness must be smaller than 8 micron to assure Lamb wave excitation. Inductively Coupled Plasma (ICP) technique was employed to etch silicon to the desired thickness. The etching rate of ICP was set to 0.8micron per cycle. In this research, a Lamb wave device with 7 μm-thick silicon and a Lamb wave excitation on a membrane composed only of ZnO and Si_3N_4 were fabricated and discussed. The measurement results are shown in Sec. 4.3.

4.3 Measurement of Silicon-based Acoustic Wave Devices

This section divides into four parts; the first part gave characteristics of Si_3N_4 and ZnO thin films. Then, before silicon was etched, frequency response of ZnO(0.5)/ Si_3N_4(1)/Si(300) SAW devices were measured. The number in parentheses represents the thickness of the material. Next, Lamb wave signals of ZnO(0.5)/Si_3N_4(1)/Si(7) structures were measured and discussed. Finally, a Lamb wave device composed of ZnO(0.5)/Si_3N_4(1) membrane was measured.

4.3.1 Characteristics of Si_3N_4 and ZnO Thin Films

In Sec. 4.2, Si_3N_4 films were deposited on both sides of silicon wafer by LPCVD. To test the characteristics of Si_3N_4 films as a stop layer which resists KOH etching, a

Si_3N_4 –deposited silicon wafer was patterned and then etched by a KOH solution. After the 300 μm-thick silicon on the region which was not protected by Si_3N_4 films was all etched, the wafer was rinsed by deionised water and dried by nitrogen gas. Fig. 4.11 (a) shows the Si_3N_4 membrane which acts as a etch stop layer and support layer for the following deposited ZnO thin film. In Fig. 4.11 (a), Si_3N_4 membrane is not flat and is with periodic wrinkled pattern. This implies that residual stress occurs when the Si_3N_4 membrane is released from silicon. A wrinkled Si_3N_4 membrane is not suitable for being a support layer for ZnO film. Therefore, post-deposition annealing process was used to reduce the residual stress of Si_3N_4 membrane.

Post-deposition annealing is a popular method for relieving stress in thin films. During post-deposition annealing, boundary defects of thin films can be eliminated and some of the energy stored in the film which causes stress can be released. In this research, a silicon wafer with Si_3N_4 membrane in a box furnace was with heat treatment at 1095℃ for 1 hour. Fig. 4.11 (b) shows a photograph of the Si_3N_4 membrane after annealing. Compare Fig. 4.11 (a) and (b), the Si_3N_4 membrane became flat and uniform after heat treatment. Therefore, after LPCVE deposition, Si_3N_4 films should be annealed before the ZnO film is sputtered on the Si_3N_4 film.

ZnO film, the main part of a Lamb wave device, serves as the piezoelectric media and the semiconducting sensing film. Thus, the property of the sputtered ZnO thin film should be investigated. X-ray diffraction (XRD) method was used to observe the diffraction peak of the ZnO film. Fig. 4.12 shows the XRD pattern of a ZnO film. A strong intensity peak at 34.46° is observed. This diffraction peak indicates preferential growth in the [0 0 2] orientation of the 0.5 μm-thick ZnO thin film. Compared with the 50 nm-thick ZnO film shown in Fig. 3.9, the intensity of 0.5 μm -thick ZnO film is much stronger and

the peak is sharper. Therefore, under the same sputtering parameters, the longer the deposition time, the thicker the ZnO film is, and the stronger [0 0 2] orientation is. After the whole structure is fabricated, Energy Dispersive Spectrometer (EDS) is adopted for elemental analysis. Fig. 4.13 shows a result of a ZnO/ Si_3N_4/Si structure with IDTs by EDS. The result shows the elements Zn and O are strong; the Si and Al elements are also observed.

4.3.2 SAW Signals of a ZnO/Si_3N_4/Si Layered Structure

In the fabrication process mentioned in Sec. 4.2, to ensure successful wave-excitation by IDTs, SAW devices should be measured before the silicon was etched. Fig. 4.14 is a photograph of fabricated IDTs and gratings with a linewidth of 2μm. It shows that the aluminum IDTs and gratings were all well-fabricated on ZnO. Following fabrication, frequency responses of ZnO(0.5)/ Si_3N_4(1)/Si(300) SAW devices were measured by an Agilent 8714ES Network Analyzer. In this research, three wavelengths are designed and fabricated and the IDT parameters are listed in Table 4.1. In the following, three types of SAW devices are measured and discussed.

Fig. 4.15 shows the measured frequency response of a ZnO(0.5)/ Si_3N_4(1)/Si(300) SAW device with a wavelength of 8 micron. The center frequency was 537 MHz, and insertion loss was 33dB. This figure shows that the acoustic signal is obvious. Fig. 4.16 is the time domain signal of this SAW device. It shows a strong direct response and the triple transit signal was also obvious, which indicates acoustic waves were successfully generated. Fig. 4.17 show the SAW signal of 8μm-wavelength after time gating, which means that the electromagnetic feedthrough was not included. In Fig. 4.17, the peak frequency remained 537MHz while the insertion loss was 35dB, only slightly lower than the original signal. Thus, the performance of the frequency response of this 537MHz SAW device is good.

A measured frequency response of a ZnO(0.5)/ Si_3N_4(1)/Si(300) SAW device with a wavelength of 9.8 μm is shown in Fig. 4.18. The thin line is the original SAW signal directly measured by a network analyzer, and the bold line represents the frequency response of this SAW device after time gating. In this figure, the center frequency was 447MHz and the loss of the original signal and time-gated signal were 31 and 34dB, respectively. This figure demonstrates that the acoustic signal at the wavelength of 9.8 μm is also strong and obvious.

Fig. 4.19 shows the measured frequency response of a ZnO(0.5)/ Si_3N_4(1)/Si(300) SAW device with a wavelength of 12 μm. The thin line represents the SAW signal measured by a network analyzer, and the bold line is the time-gated frequency response of this SAW device. The center frequency of this SAW device was 375MHz. The insertion loss of the measured frequency response was 35dB while the one of the time-gated signal was 38dB.

In brief, ZnO(0.5)/ Si_3N_4(1)/Si(300) SAW devices with wavelengths of 8, 9.8 and 12 μm are well-fabricated and performances are all good. Therefore, the following fabrication process of which the silicon is etched can be accomplished and Lamb wave devices can be realized.

4.3.3 Lamb Wave Signals of a ZnO/Si_3N_4/Si structure

After checking the successful excitations of acoustic waves by IDTs, the back side of the wafer was patterned and silicon was etched using a KOH solution and an ICP system. The etching process stopped when the silicon thickness reached 7 μm to assure Lamb wave generation of the ZnO/Si_3N_4/Si structure. Fig. 4.20 shows a time domain signal of a ZnO(0.5)/Si_3N_4(1)/Si(7) Lamb wave structure, and the wavelength is 8 μm. It shows that the direct response is obvious. Fig. 4.21 is the measured frequency responses of a

$ZnO(0.5)/Si_3N_4(1)/Si(7)$ Lamb wave device with a wavelength of 8 μm. The dashed line represents the measured signal directly from a network analyzer, and the solid line represents the time-gated Lamb wave signal of this structure. The center frequency was 535MHz. The insertion loss of the original measured signal was 38dB, and that of the time-gated signal was 41dB. Compared with Fig. 4.15 and Fig. 4.17, the center frequency and the signal pattern of this Lamb wave structure are similar to those of the SAW device. This phenomenon agrees with numerical simulations shown in Fig. 4.6, which demonstrates that at a constant wavelength, Lamb wave phase velocity approaches to SAW phase velocity at high frequency.

The original measured and time-gated Lamb wave signal with a wavelength of 9.8 μm of a $ZnO(0.5)/Si_3N_4(1)/Si(7)$ structure is shown in Fig. 4.22. The center frequency is 430 MHz. The insertion losses of the original and time-gated signal are 46 and 54 dB, respectively. Compared with Fig. 4.18, the center frequency and of Lamb wave is lower than the SAW one. Again, this coincides with numerical calculations shown in Fig. 4.6.

Fig. 4.23 is the original measured and time-gated frequency responses of a $ZnO(0.5)/Si_3N_4(1)/Si(7)$ Lamb wave device with a wavelength of 12 μm. In this figure, the Lamb wave signal is weaker than the ones with smaller wavelength, as shown in Fig. 4.21 and Fig. 4.22. This phenomenon can be explained by Fig. 4.7. For a $ZnO(0.5)/Si_3N_4(1)/Si(7)$ Lamb wave device, coupling coefficients becomes smaller as the frequency decreases.

In brief, Lamb wave devices based on $ZnO/Si_3N_4/Si$ structure with silicon equal to 7 μm were measured and discussed. The performances of $ZnO(0.5)/Si_3N_4(1)/Si(7)$ Lamb wave structure are similar to the one of SAW when the wavelength is small. When the wavelength becomes larger, the characteristics of Lamb wave device such as coupling

coefficient decreases. Therefore, a Lamb wave device with better performance needs to be fabricated. In the next section, a Lamb wave device consists of ZnO/ Si_3N_4 membrane was measured will be discussed.

4.3.4 Lamb Wave Signal of a ZnO/ Si_3N_4 Membrane

In this section, a Lamb wave device based on a ZnO/ Si_3N_4 membrane fabricated by etching the whole silicon to the Si_3N_4 stop layer was measured. Fig. 4.24 shows a photograph of a ZnO/ Si_3N_4 membrane-Lamb wave device adhered to a PCB board. In this figure, the membrane is not flat. Though the stress of Si_3N_4 was reduced by post-deposition annealing, a 0.5 μm-thick ZnO gave the membrane another stress such that residual stress still existed in this structure. However, the flat Si3N4 membrane supported the ZnO layer such that the 1.5 μm-thick ZnO/ Si_3N_4 membrane still held and was not fragile even when it was wire-bonded on a PCB board. Before adhering to a PCB board, a ZnO/ Si_3N_4 membrane-Lamb wave device was measured by a network analyzer. Fig. 4.25 shows the original Lamb wave frequency response of a ZnO/ Si_3N_4 membrane with a wavelength of 8 μm. The time domain signal of this membrane is shown in Fig. 4.26. As shown in this figure, the direct response and the triple transit echo are obvious, which indicates that Lamb waves on a 1.5 μm-thick ZnO/Si_3N_4 membrane were successfully generated. Fig. 4.27 is the frequency response of this ZnO/ Si_3N_4 membrane after time-gating. After time gating, the signal to noise ratio of Lamb wave is good. Therefore, an ultra-thin membrane Lamb wave device based on ZnO and Si_3N_4 is fabricated and Lamb wave successfully generated in this structure. In the next section, a Lamb wave UV detector is constructed and the performance is discussed.

4.4 An Silicon-based Lamb-Wave Ultraviolet Microsensor

After verifying the performances of the Lamb wave device, an ultraviolet sensing

system based on the Lamb wave device was realized. This section begins with the construction of a UV-sensing system. Next, experimental results of Lamb wave UV detector based on $ZnO/Si_3N_4/Si$ structure and ZnO/Si_3N_4 membrane are presented. Finally, comparison of experimental results and numerical calculations of the acoustoelectric effect are discussed and analyzed.

4.4.1 Construction of a Silicon-based Lamb Wave UV Detecting System

Experimental setup of a UV detecting system is shown in Fig. 4.28. The Lamb-Wave devices described in Sec. 4.3 are used as UV microsensors. Here, a two-port Lamb wave sensor wire-bonded on a PCB board is connected to a network analyzer through SMA connectors. A UV source is composed of a Xenon lamp and a UV filter. The Lamb wave sensor is then illuminated by this UV source. When the ZnO sensing film is under UV illumination, acoustic loss which results from the acoustoelectric effect can be observed by a network analyzer. Then the measurement results are transmitted to a personal computer with a general purpose interface bus (GPIB) cable for further data analysis.

4.4.2 Characteristics of Lamb Wave UV microsensors

First, a Lamb wave UV sensor based on a $ZnO(0.5)/Si_3N_4(1)/Si(7)$ structure was measured. The wavelength of this UV microsensor was 9.8 μm. Before the UV light turned on, the wire-bonded Lamb wave sensor was connected to a network analyzer and the signal was stable, as the dashed line shown in Fig. 4.29. Compare Fig. 4.29 with Fig. 4.22, after wire-bonded and adhered to a PCB board, the signal measured through SMA connectors was weaker than that measured directly by probes. However, Lamb wave signal can still be measured. When the measured signal was stable for several minutes, a 370nm UV light source with a power density of $0.06mWcm^{-2}$ turned on. The insertion loss became larger, as shown in the solid line in Fig. 4.29. The difference between the response with and without UV illumination was only about 0.1dB. After time gating process, the difference between

the responses with and without UV illumination is shown in Fig. 4.30. In this figure, the dashed line represents that the UV source was off and the solid line represents that the sensor was under UV illumination. As Fig. 4.30 shows, after time-gating, a loss of 1dB at 429MHz is observed of this sensor with UV illumination.

When the light source is out of the UV range, the sensor should be insensitive. To demonstrate this characteristic, the UV sensor based on a $ZnO(0.5)/Si_3N_4(1)/Si(7)$ structure was subjected to a 650nm light source with a power density of 0.186mW cm^{-2}.
Fig. 4.31 shows the UV sensor response when 650nm light source turned off and on, respectively. The dashed line represents that 650nm was off and the solid line means that the 650nm was on. As can be seen in the figure, there was no difference of insertion losses of the UV sensor between on/off 650nm. Fig. 4.32 shows time-gated signals of the UV sensor under 650nm illumination. Again, there was no change whether a 650nm was on or off. Therefore, a Lamb wave UV sensor based on a $ZnO(0.5)/Si_3N_4(1)/Si(7)$ structure can tell the difference of acoustic losses between UV illumination on and off. Moreover, the UV sensor is insensitive to a light source which is not in the UV range.

Though a Lamb wave UV sensor based on a $ZnO(0.5)/Si_3N_4(1)/Si(7)$ structure was successfully fabricated and tested, the acoustic loss due to the AE effect by UV illumination was only 0.1dB. Next, a $ZnO(0.5)/Si_3N_4(1)$ membrane is used as a Lamb wave UV sensor and the characteristics are discussed.

A Lamb wave UV sensor based on a $ZnO(0.5)/Si_3N_4(1)$ membrane with a 8 μm-wavelength was measured. Before the UV light turned on, the wire-bonded Lamb wave sensor was connected to a network analyzer and the signal was stable before a UV source turned on. Then, the sensor was subjected to a 370nm illumination for 4 on-off cycles. The power density of this 370nm UV source was 0.06 $mWcm^{-2}$. The sensor was repeatable and the response of one on-off cycle is shown in Fig. 4.33. The dashed line

represents that the UV source was off and the solid line represents that the sensor was under UV illumination. As shown in this figure, when a 370nm UV source turned on, an obvious difference was observed. The difference was about 0.8 dB at 255MHz. Fig. 4.34 shows the UV sensor response after time gating when 370nm was off and on. As shown in this figure, after excluding electromagnetic feedthrough, insertion losses of the pass band due to the AE effect by UV illumination were obvious and the value was 1.8 dB at 255.56MHz.

Moreover, to demonstrate that the UV sensor based on a $ZnO(0.5)/Si_3N_4(1)$ membrane is insensitive to a light source which is not in a UV range, the UV sensor was subjected to a 650nm light source with a power density of 0.186mW cm^{-2}. Fig. 4.35 shows sensor response when a 650nm source was on and off. This figure indicates that the $ZnO(0.5)/Si_3N_4(1)$ membrane UV sensor is insensitive to a 650nm light source. After time gating, there was no difference of the UV sensor before and after the 650nm turned on, as Fig. 4.36 shows.

Therefore, a Lamb wave UV sensor based on a $ZnO(0.5)/Si_3N_4(1)$ membrane is fabricated and measured for the first time, and it insensitive to a light source which is not in the UV range. Moreover, the UV sensor shows an obvious difference between acoustic losses which was under or without UV illumination.

Finally, comparisons between Lamb wave UV sensors based on $ZnO(0.5)/Si_3N_4(1)/Si(7)$ structure and $ZnO(0.5)/Si_3N_4(1)$ membrane are discussed. As mentioned in Sec. 2.3.2 and 2.3.3, for a Lamb wave device, acoustic loss due to AE interaction is modified as Eq. (2.47)

$$\frac{\Gamma}{k_x(f)} = \frac{K_{eff}^2(f)}{2} \frac{\sigma_d / \sigma_m}{1 + (\sigma_d / \sigma_m)^2}$$

Fig. 4.37 shows the calculated Lamb wave attenuation due to AE interactions in Si-based Lamb wave UV sensors by using Eq. (2.47). The bold line represents loss of a ZnO(0.5)/Si_3N_4(1) Lamb wave UV sensor, the thinner line represents loss of a ZnO(0.5)/Si_3N_4(1)/Si(7) structure, and the dashed line represents SAW loss in a ZnO(0.5)/Si_3N_4(1)/Si(300) layered structure. The simulation result indicates that the loss of a 255MHz ZnO/Si_3N_4 Lamb wave UV sensor is much larger than the loss of a 430MHz ZnO/Si_3N_4/Si UV sensor. And the losses of a ZnO/Si_3N_4/Si(7) UV sensor are similar to the SAW losses of a ZnO/Si_3N_4/Si(300) layered SAW device. Compare Fig. 4.30 with Fig. 4.34, the UV sensing response of a ZnO/Si_3N_4 Lamb wave sensor are much more obvious than a ZnO/Si_3N_4/Si sensor, which matches well with the theoretical prediction. Therefore, with a proper choice of operating frequency and thickness of each film in a layered plate, excellent performances of a Lamb wave sensor can be obtained. On the other hand, if an improper laminated plate is chosen, such as a ZnO(0.5)/Si_3N_4(1)/Si(7) structure, the performance of a Lamb wave UV sensor is not good. Moreover, loss due to AE interactions is small and similar to a ZnO(0.5)/Si_3N_4(1)/Si(300) SAW device, as Fig. 4.37 indicates.

Briefly, Si-based Lamb wave UV sensor are designed, fabricated, and measured for the first time. Results demonstrate that a ZnO(0.5)/Si_3N_4(1) membrane is a preferable candidate as a sensor using the AE effect. By introducing dispersion relations of Lamb waves into a AE theoretical model, large sensing responses can obtained by choosing proper frequency-thickness product of Lamb waves in a plate. Therefore, this research provides a principle and method for designing Lamb wave microsensors for further applications.

IDT wavelength(μm)	8	9.8	12
IDT pairs	70		
grating number	70		
aperture (λ)	100		
distance between IDT and gratings (λ)	3		
propagation length (μm)	2000-3000		

Table 4.1 IDT parameters

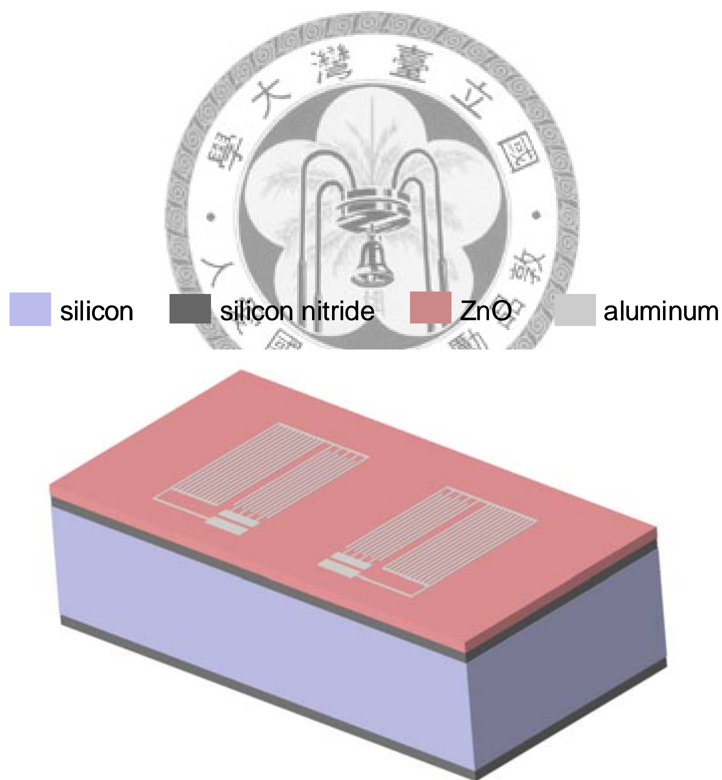

Fig. 4.1 A ZnO/ SiN_x /Silicon surface wave device

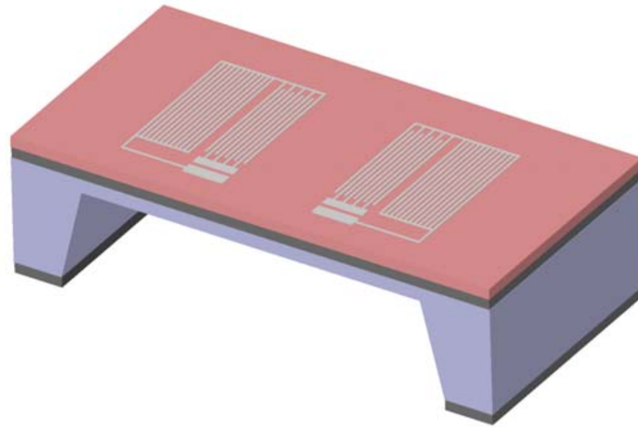

Fig. 4.2 A ZnO/ SiN_x /Silicon Lamb wave device

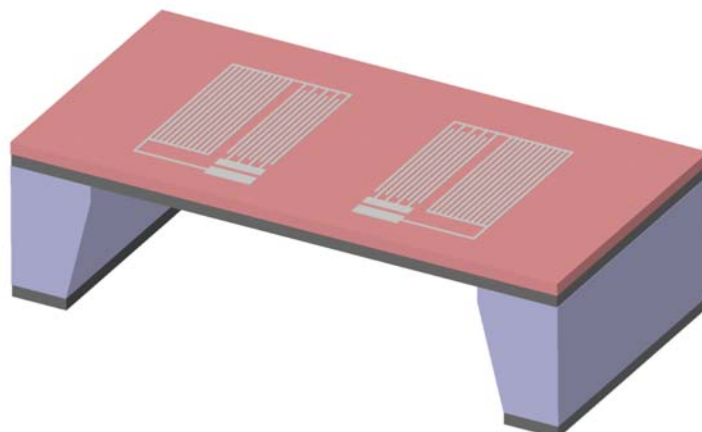

Fig. 4.3 A ZnO/SiN_x Lamb wave device

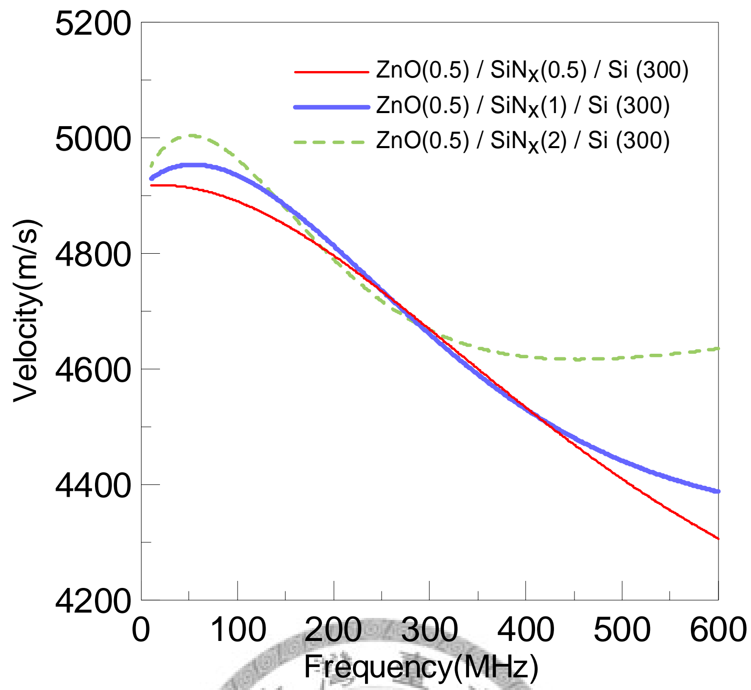

Fig. 4.4 SAW velocity dispersion of $ZnO/SiN_x/Si$

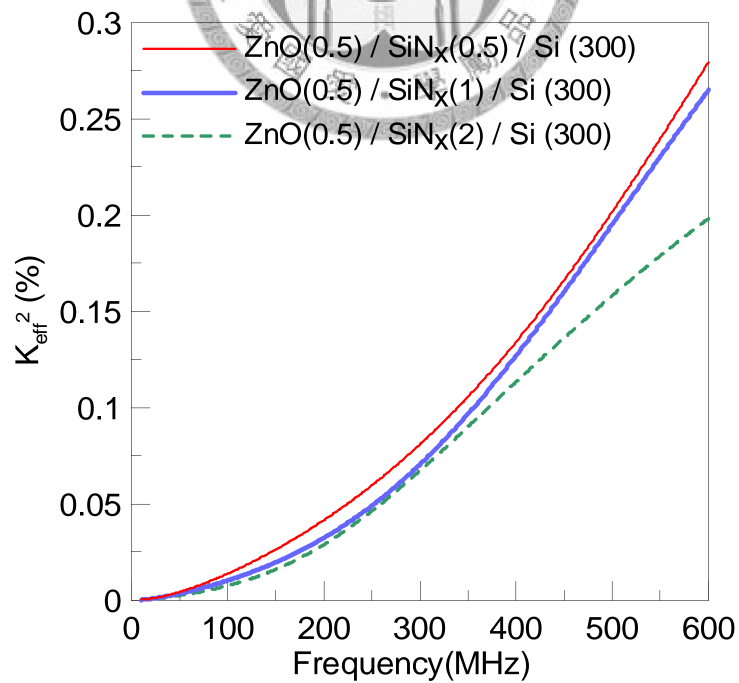

Fig. 4.5 Coupling coefficient of SAW on $ZnO/SiN_x/Si$ structures

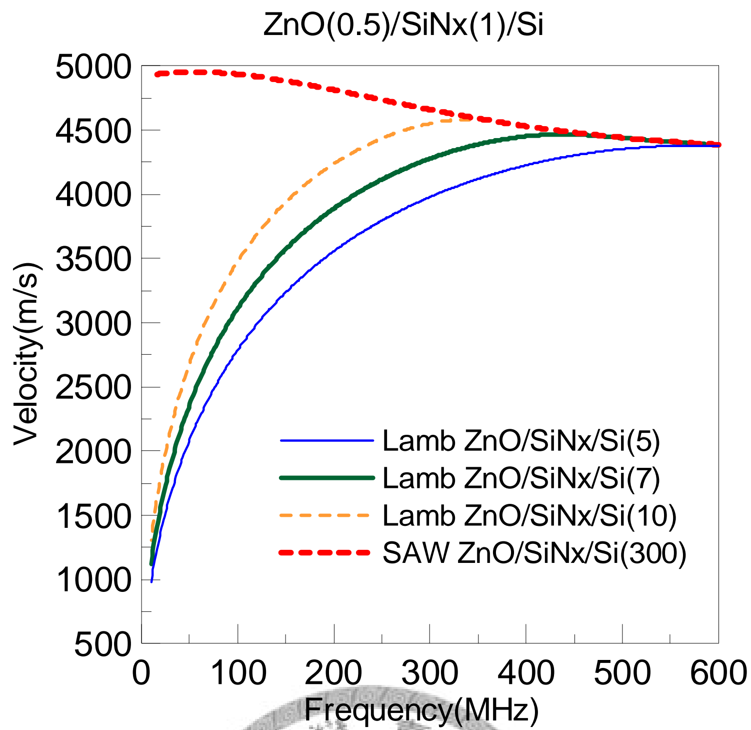

Fig. 4.6 Velocity dispersion of SAW and A_0 mode in ZnO/SiNx/Si

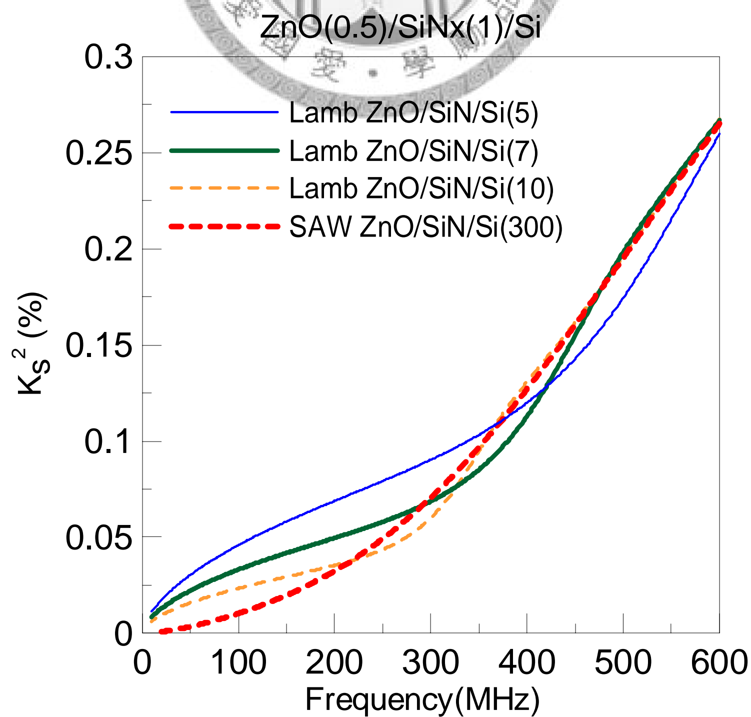

Fig. 4.7 Coupling coefficient of SAW and A_0 mode in ZnO/SiNx/Si

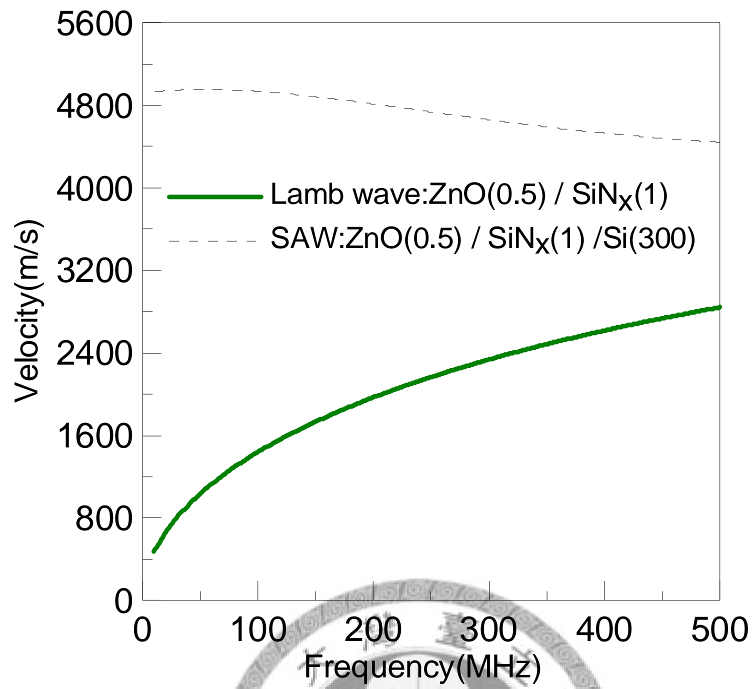

Fig. 4.8 A_0 mode of Lamb wave dispersion in ZnO/SiN_x

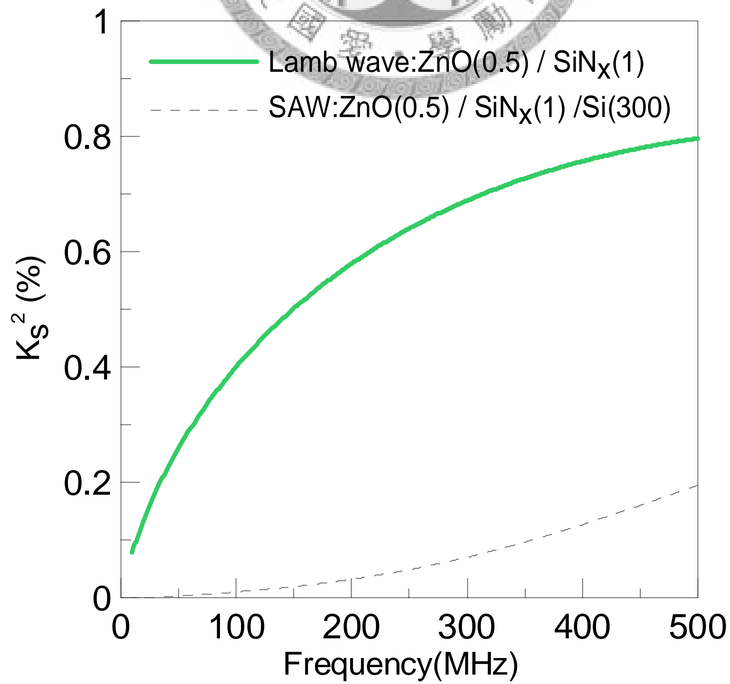

Fig. 4.9 Coupling coefficient of A_0 mode in ZnO/SiN_x

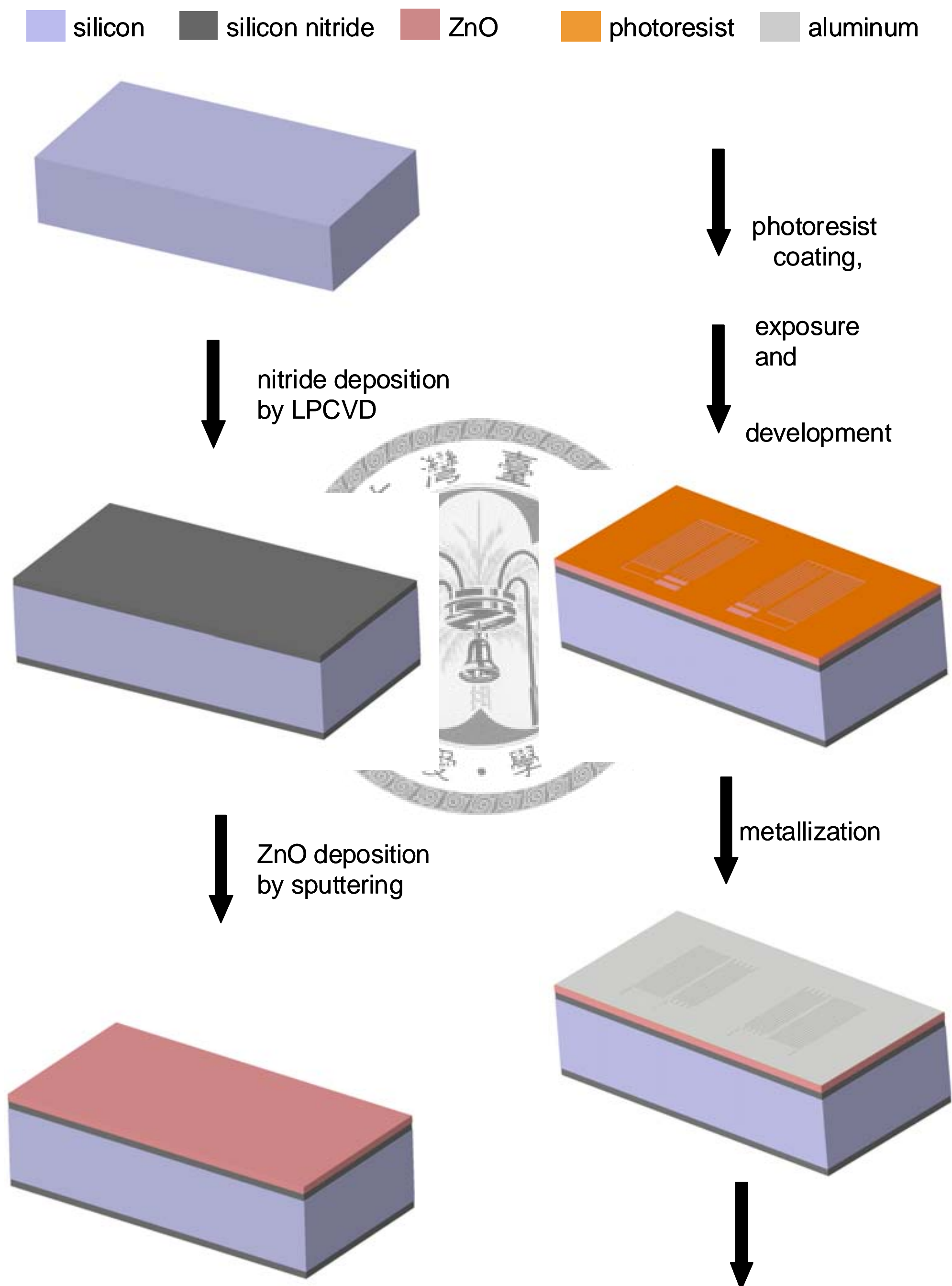

Fig. 4.10 Fabrication process of a Si-based Lamb wave device

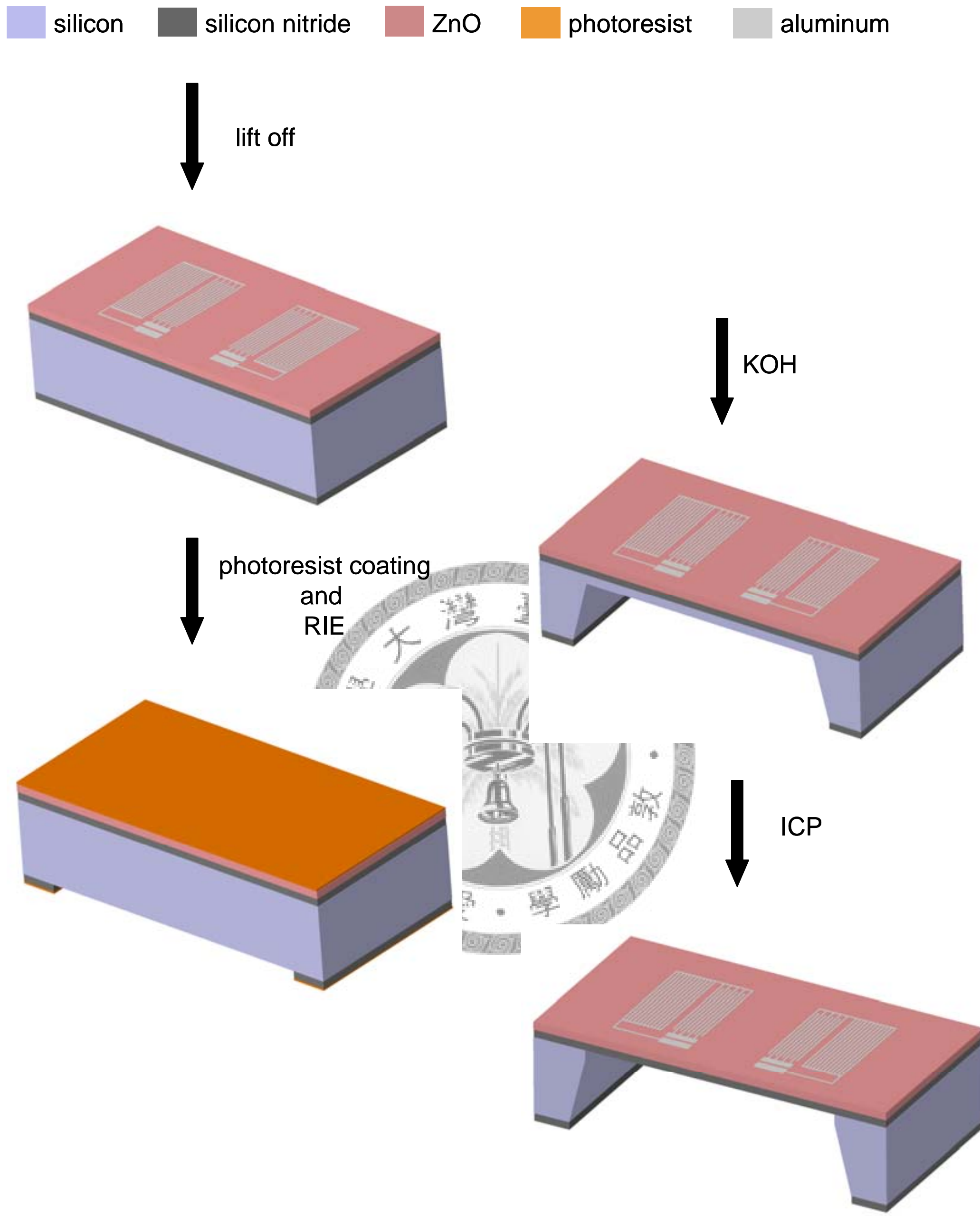

Fig. 4.10 Fabrication process of a Si-based Lamb wave device (cont.)

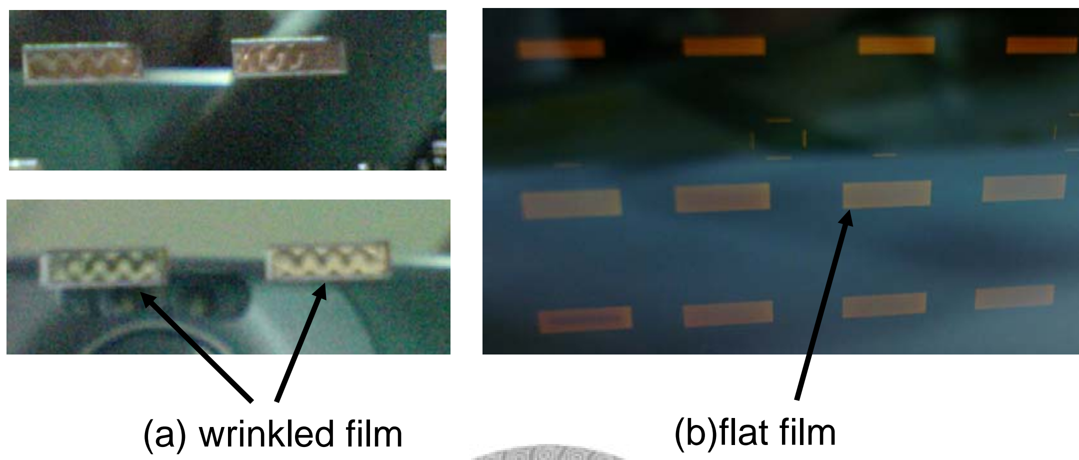

Fig. 4.11 Si_3N_4 membrane (a) before annealing (b) after annealing

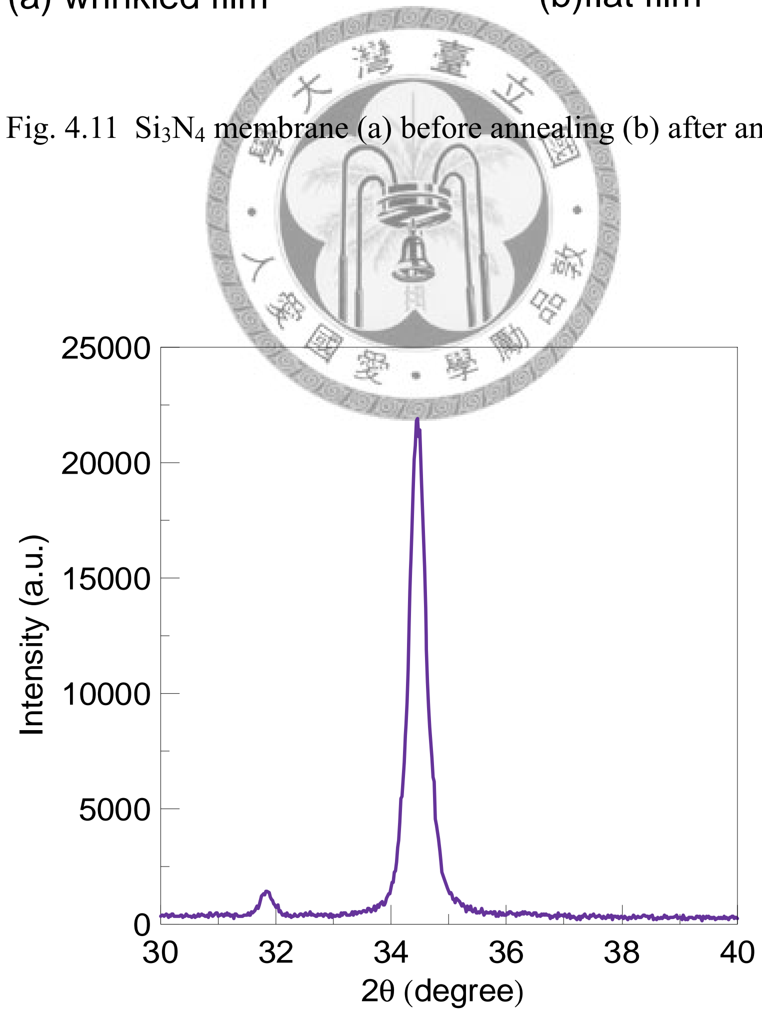

Fig. 4.12 XRD pattern of a ZnO thin film

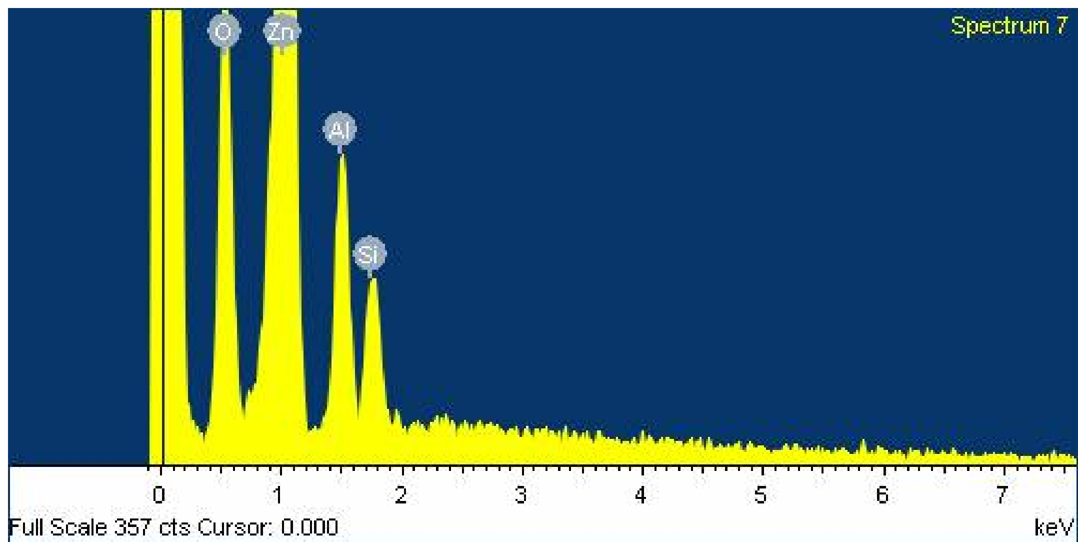

Fig. 4.13 EDS pattern of $ZnO/Si_3N_4/$ Si structure patterned with IDTs

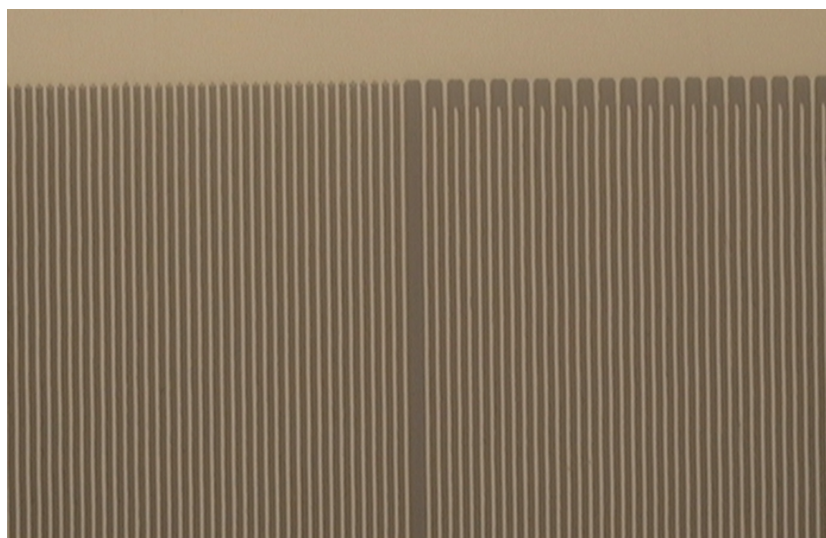

Fig. 4.14 Photograph of IDTs and gratings, linwidth= 2 micron

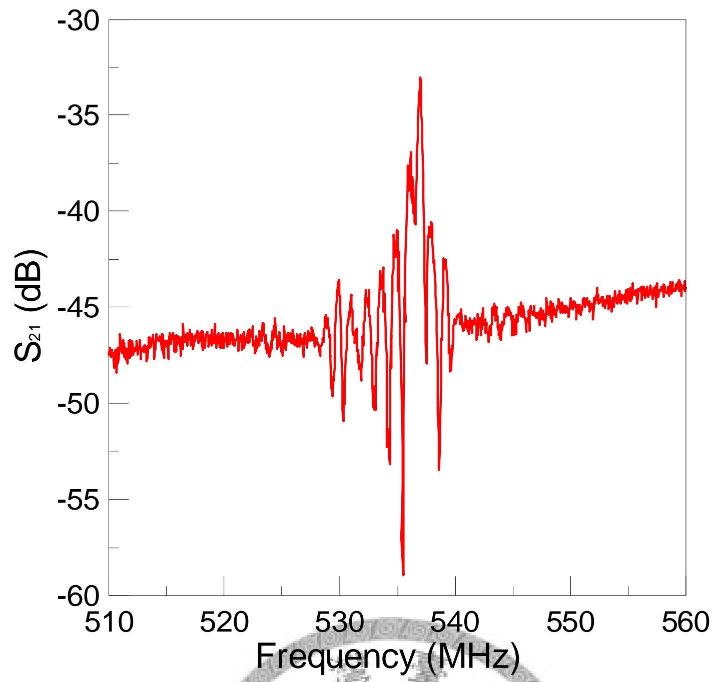

Fig. 4.15 Frequency response of a $ZnO/Si_3N_4/Si$ SAW device, IDT wavelength=8 micron

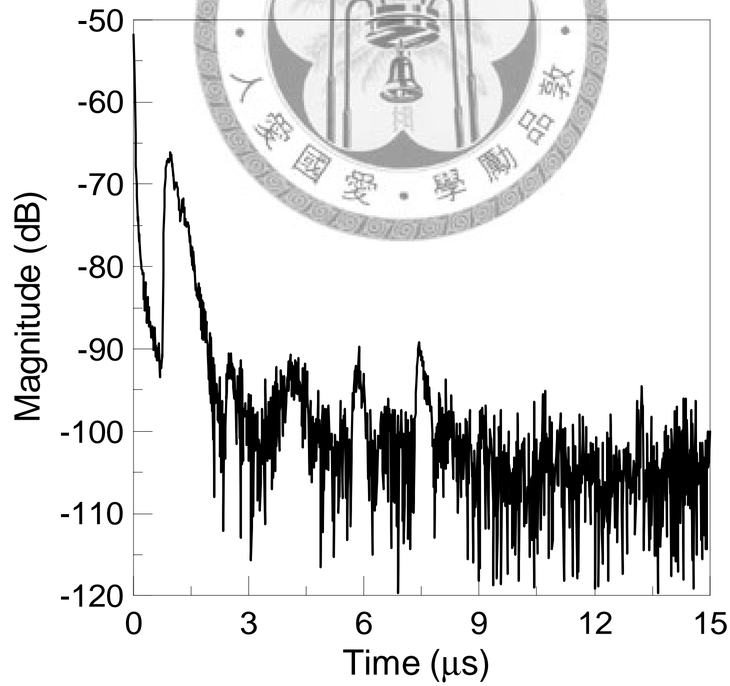

Fig. 4.16 Time domain of a $ZnO/Si_3N_4/Si$ SAW device

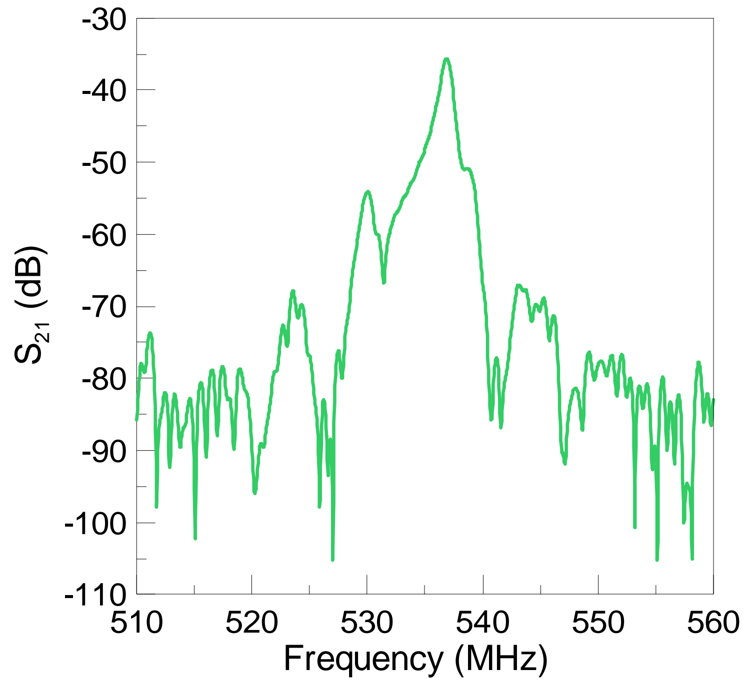

Fig. 4.17 Time-gated SAW signal of a $ZnO/Si_3N_4/Si$ structure

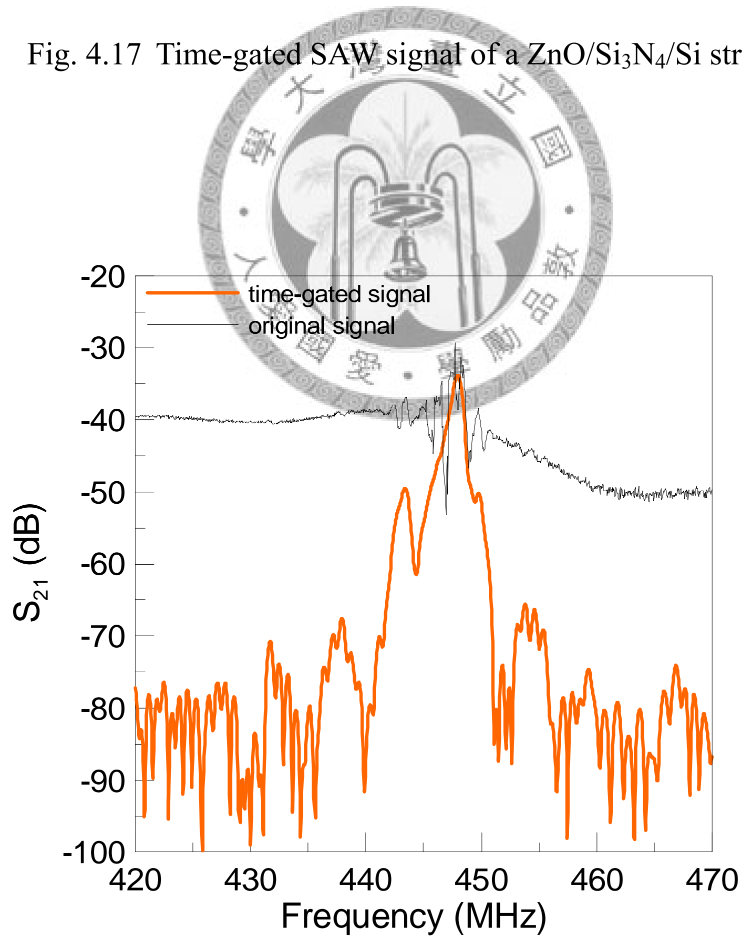

Fig. 4.18 SAW signal of a $ZnO/Si_3N_4/Si$ structure, IDT wavelength=9.8 micron

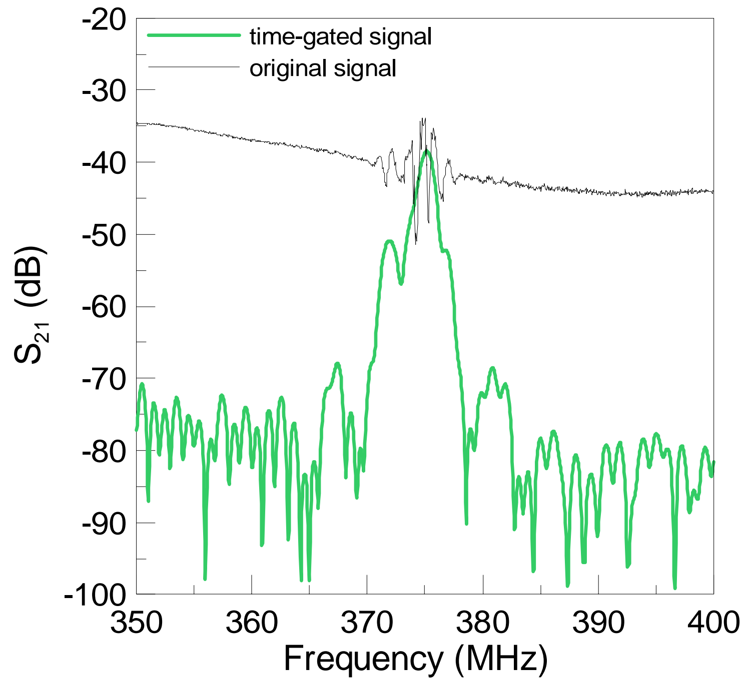

Fig. 4.19 SAW signal of a $ZnO/Si_3N_4/Si$ structure, IDT wavelength=12 micron

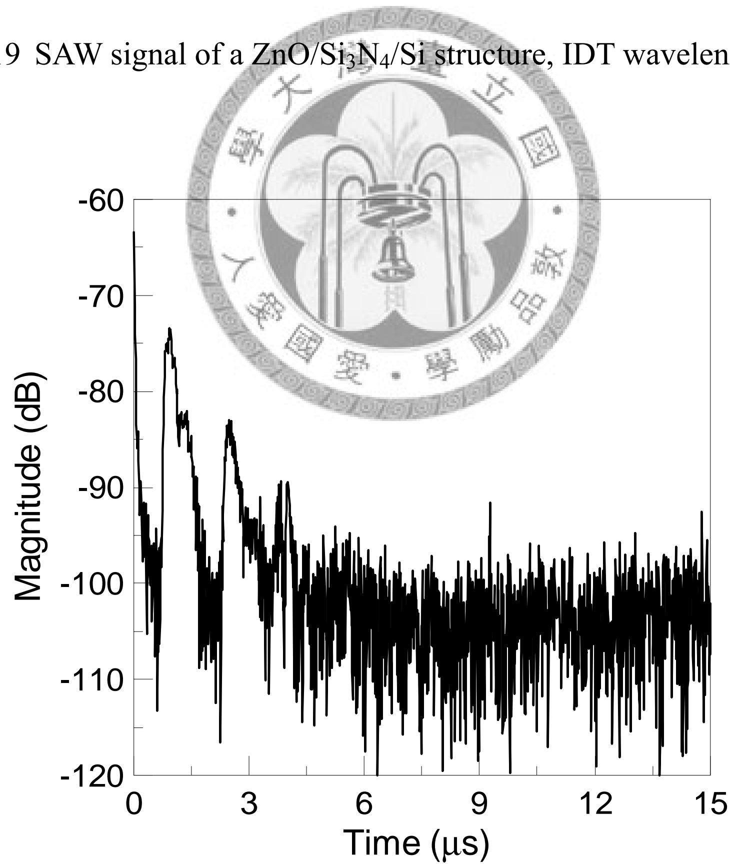

Fig. 4.20 Time domain of a $ZnO/Si_3N_4/Si$ Lamb wave device, wavelength=8 micron

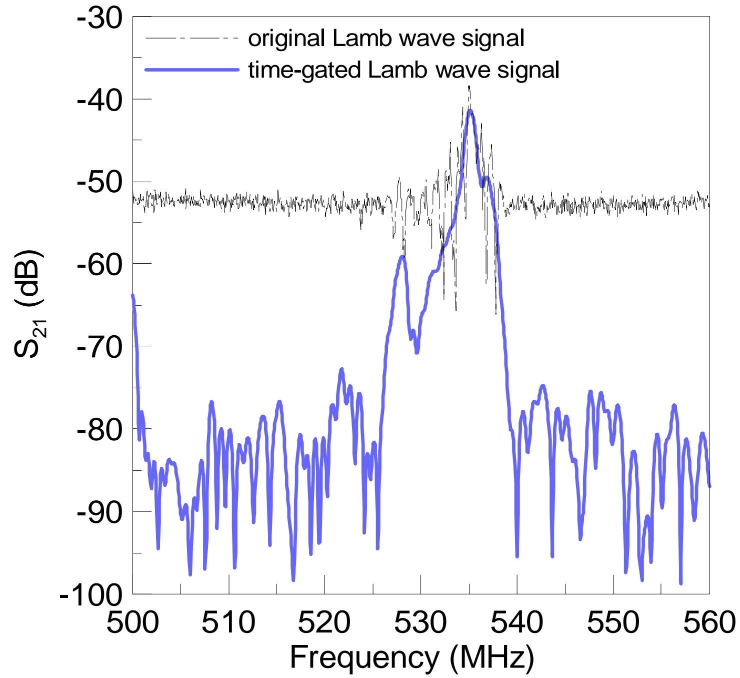

Fig. 4.21 Lamb wave signal of a $ZnO/Si_3N_4/Si$ structure, wavelength=8 micron

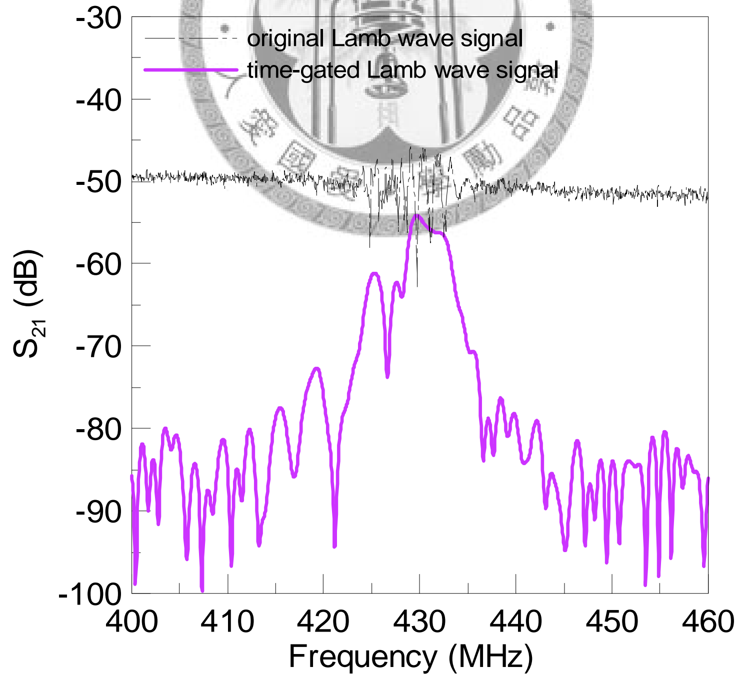

Fig. 4.22 Lamb wave signal of a $ZnO/Si_3N_4/Si$ structure, wavelength=9.8 micron

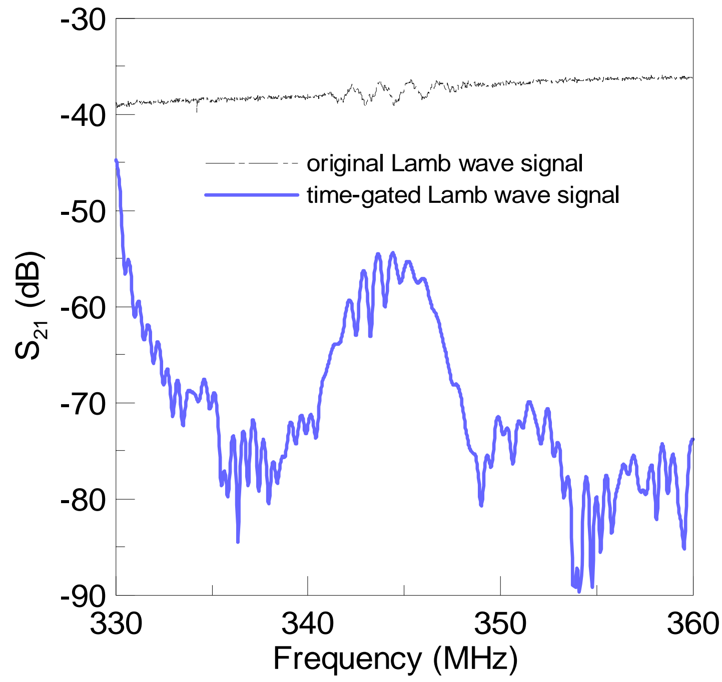

Fig. 4.23 Lamb wave signal of a $ZnO/Si_3N_4/Si$ structure, wavelength=12 micron

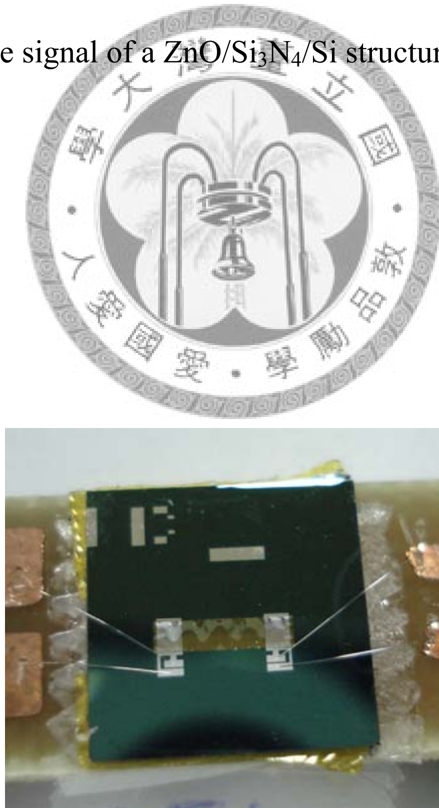

Fig. 4.24 A photograph of a ZnO/Si_3N_4 Lamb wave device

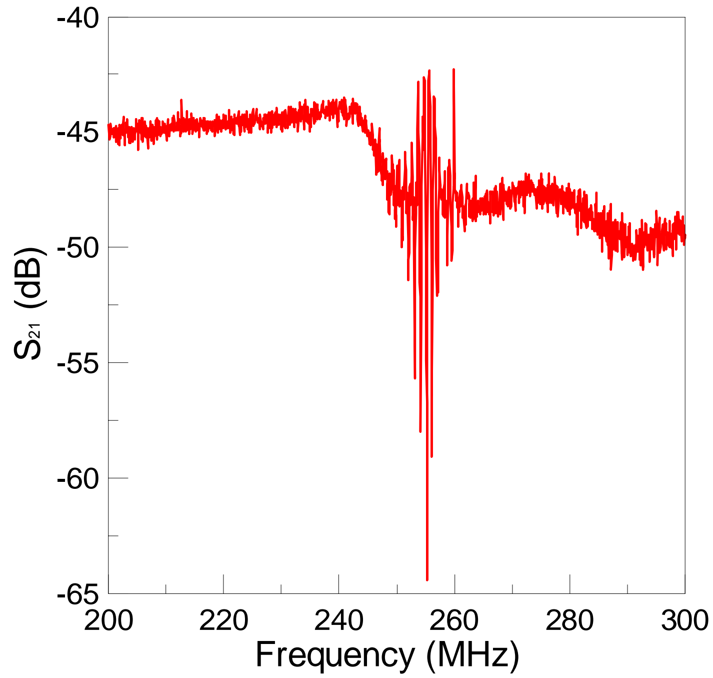

Fig. 4.25 Frequency response of a ZnO/Si_3N_4 Lamb wave device

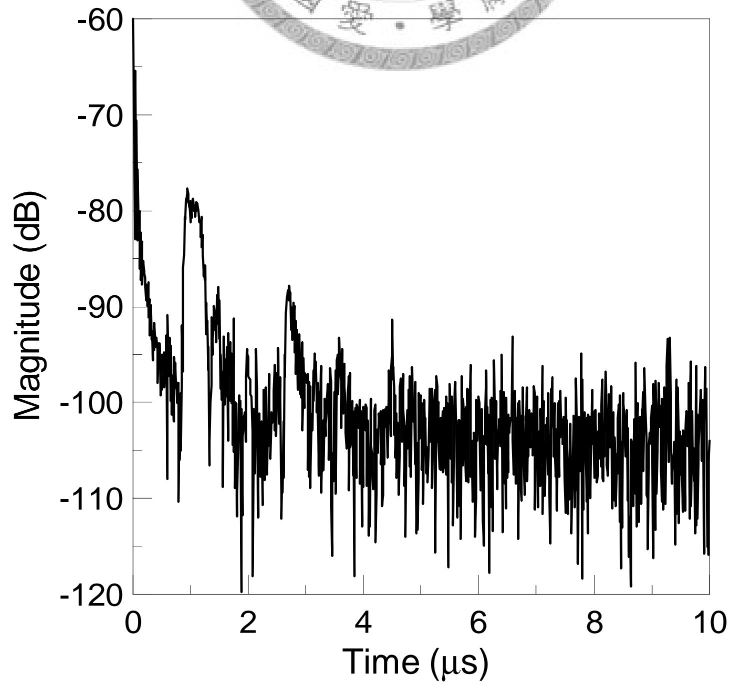

Fig. 4.26 Time domain of a ZnO/Si_3N_4 Lamb wave device

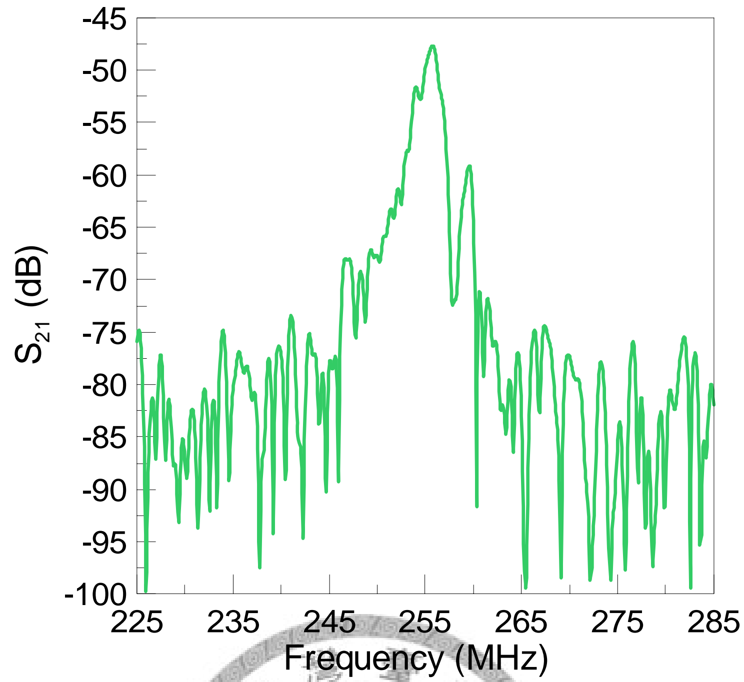

Fig. 4.27 Time-gated Lamb wave signal of a ZnO/Si_3N_4 membrane

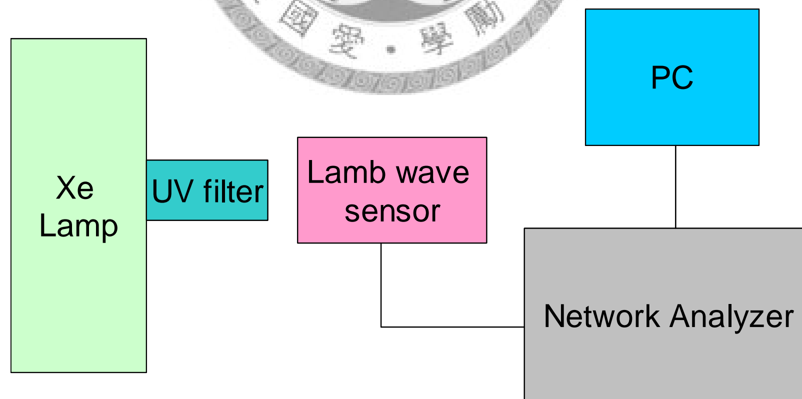

Fig. 4.28 A Lamb wave UV sensing system

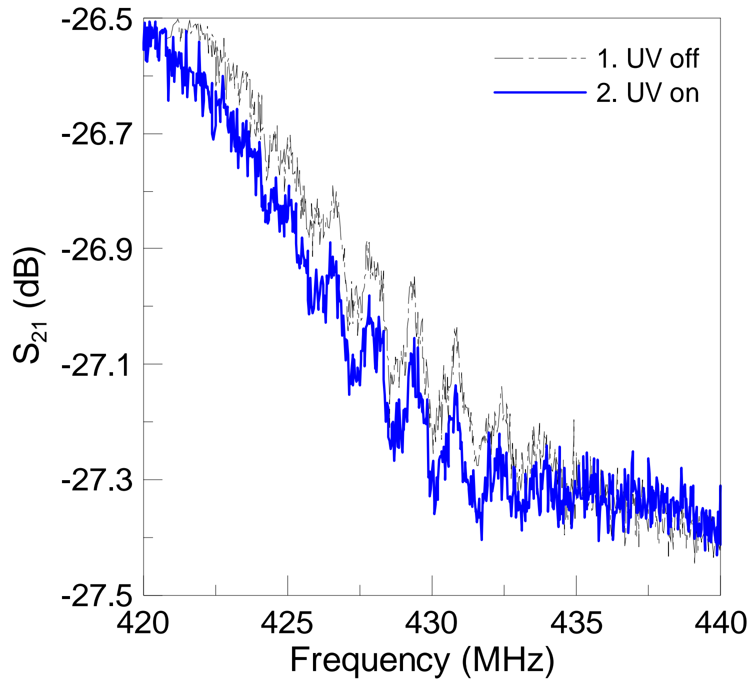

Fig. 4.29 Response of a $ZnO(0.5)/Si_3N_4(1)/Si(7)$ Lamb wave UV sensor under 370nm illumination

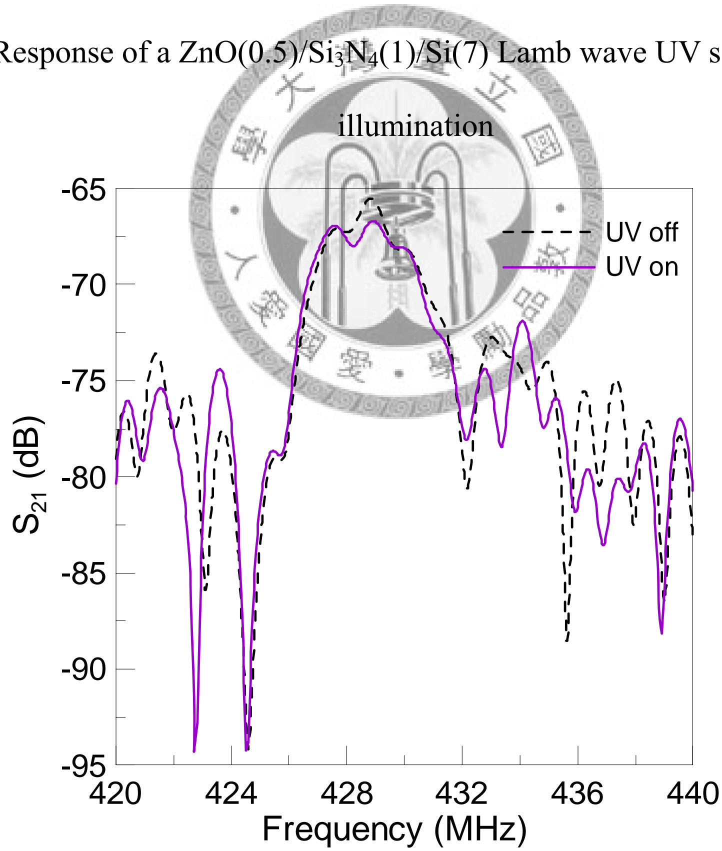

Fig. 4.30 Time-gated signal of a $ZnO(0.5)/Si_3N_4(1)/Si(7)$ Lamb wave UV sensor under 370nm illumination

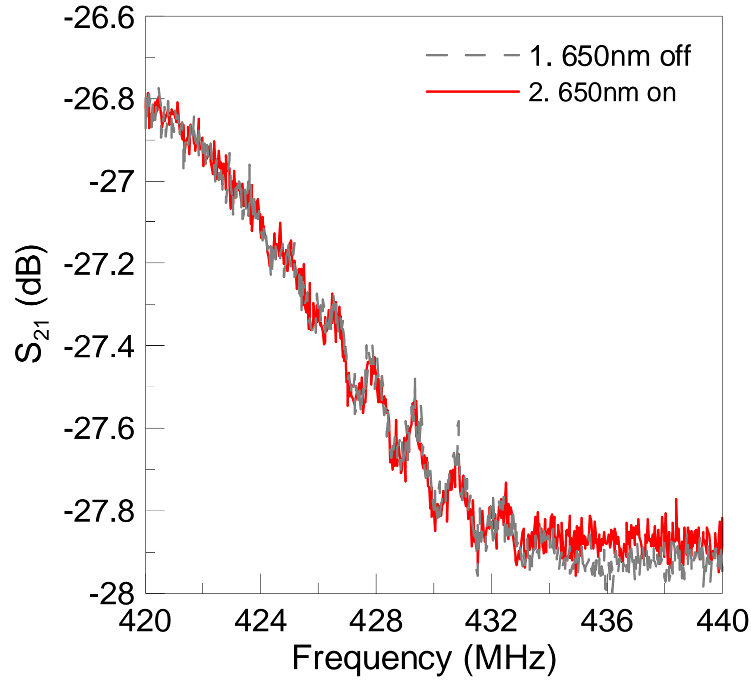

Fig. 4.31 Response of a $ZnO(0.5)/Si_3N_4(1)/Si(7)$ Lamb wave UV sensor under 650nm illumination

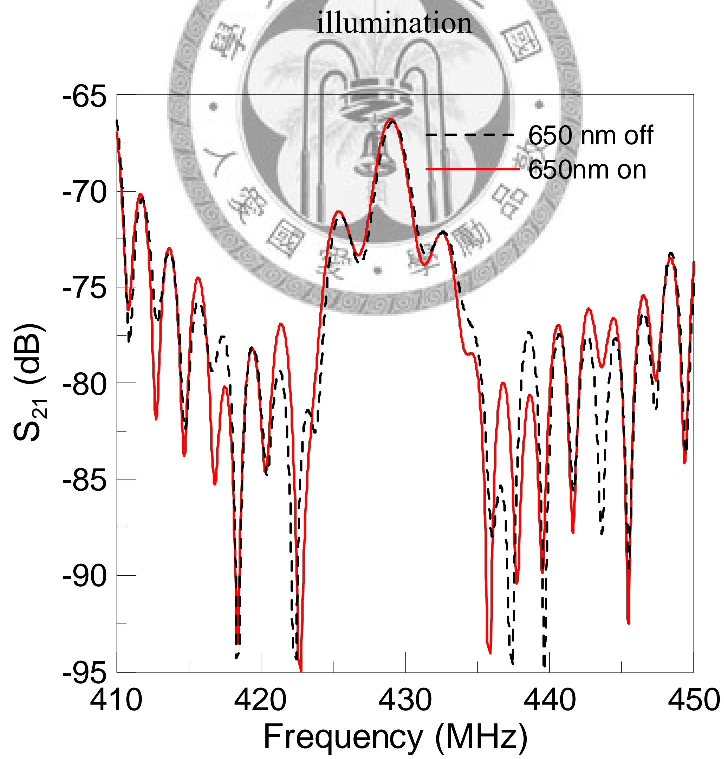

Fig. 4.32 Time-gated signal of a $ZnO(0.5)/Si_3N_4(1)/Si(7)$ Lamb wave UV sensor under 650nm illumination

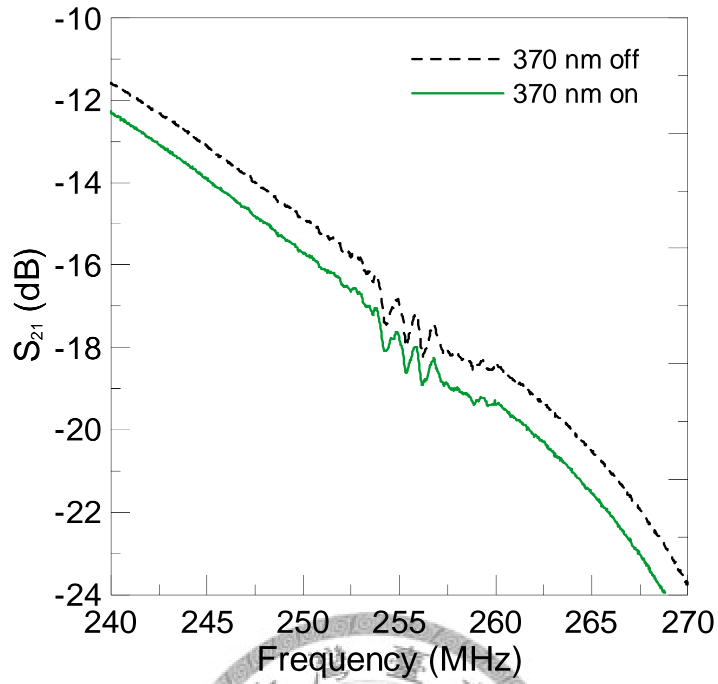

Fig. 4.33 Response of a $ZnO(0.5)/Si_3N_4(1)$ Lamb wave UV sensor under 370nm illumination

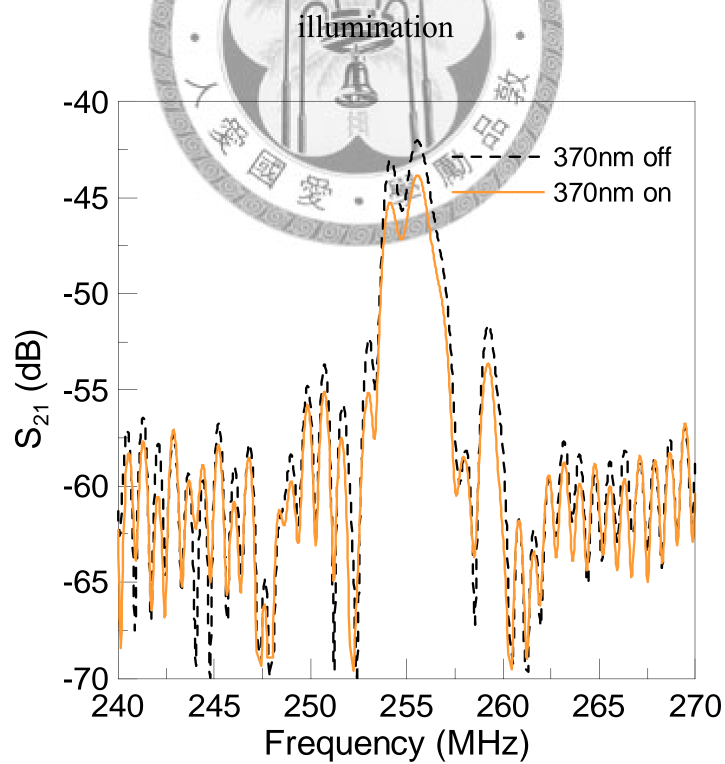

Fig. 4.34 Time-gated signal of a $ZnO(0.5)/Si_3N_4(1)$ Lamb wave UV sensor under 370nm illumination

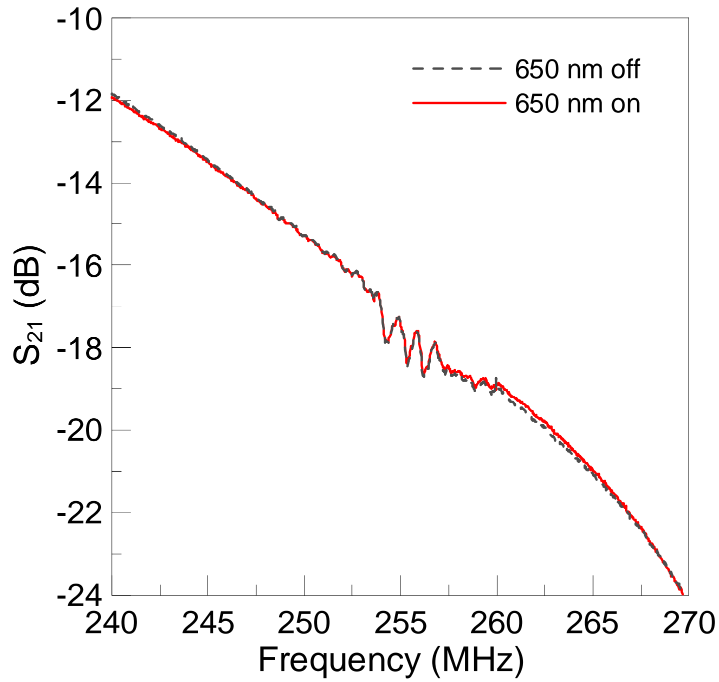

Fig. 4.35 Response of a $ZnO(0.5)/Si_3N_4(1)$ Lamb wave UV sensor under 650nm illumination

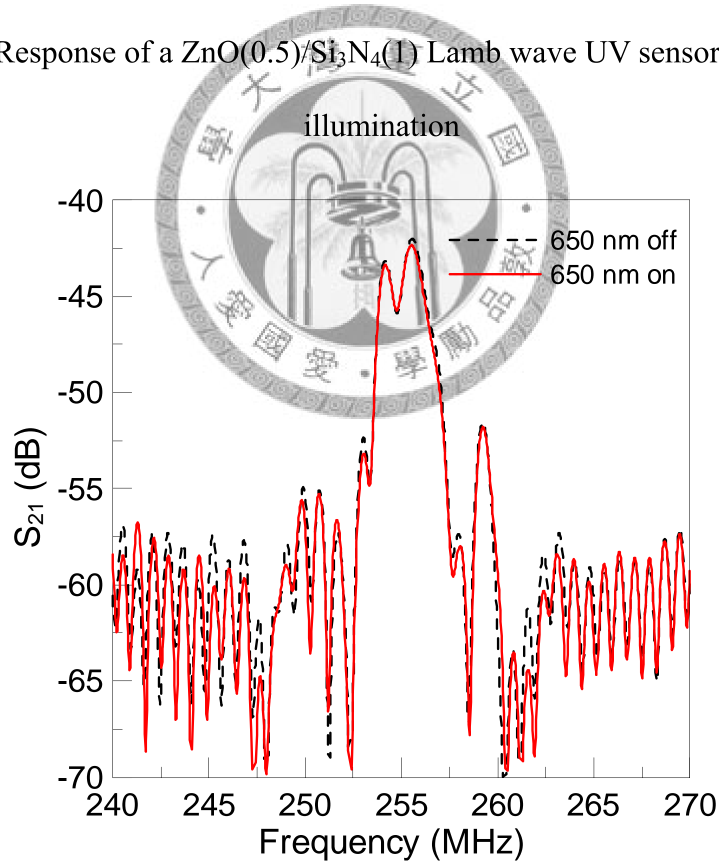

Fig. 4.36 Time-gated signal of a $ZnO(0.5)/Si_3N_4(1)$ Lamb wave UV sensor under 650nm illumination

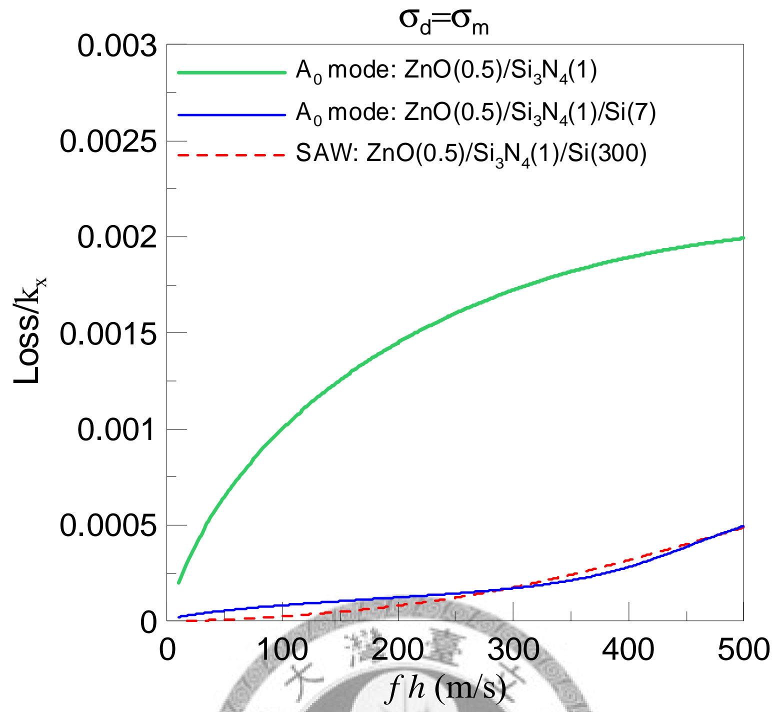

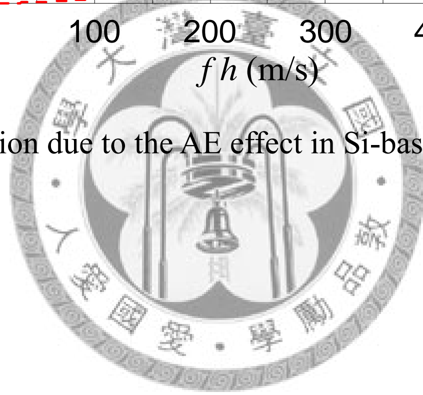

Fig. 4.37 Attenuation due to the AE effect in Si-based Lamb wave sensors

Chapter 5 Conclusions and Prospects

This chapter divides into two parts. Sec. 5.1 gives conclusions of this study. Sec. 5.2 points out some prospects extending from this work.

5.1 Conclusions

In this study, surface and Lamb wave microsensors using the acoustoelectric effect have been both theoretically and experimentally investigated. Some conclusions are given as follows.

1. An AE model applied to SAW propagation are briefly reviewed and introduced in this work first. SAW velocity changes resulting from the AE interactions in a LiNbO3 substrate coating with a ZnO film were calculated. Results show that at $\sigma_d = \sigma_m$, SAW velocity change reaches a value of 1.3%. Furthermore, by introducing the dispersion relations, a modified AE model was used to deal with the influences of AE interactions on Lamb wave propagation. Based on the numerical calculations, we found that at $\sigma_d = \sigma_m$, the SAW velocity change of ZnO is about 0.25% while the velocity change of Lamb wave in ZnO is larger than 0.4% at frequencies above 200MHz. Moreover, a maximum Lamb wave velocity change reaches approximately 0.6% at 700MHz. Results indicate that by choosing a proper frequency, the velocity change of Lamb wave in a ZnO plate due to the AE interactions can be 2.4 times larger than the one of SAW in ZnO. Similarly, attenuations of Lamb waves due to the AE effect can be much larger than SAW loss by choosing higher operating frequencies of a ZnO plate. On the other hand, for frequencies lower than 100MHz, the velocity changes of Lamb waves are smaller than 0.2%, which are even smaller than that of SAW. Attenuations of Lamb waves are also smaller than SAW attenuation at low frequencies. In other words, with an improper choice of operating frequency, influences of AE interactions on Lamb wave propagation in a ZnO plate are not

strong and are even weaker than the influences on SAW propagation in ZnO. In short, characteristics of Lamb wave propagation influenced by AE interactions in a piezoelectric semiconducting plate depend strongly on frequency, thus dispersion relations must be taken into account when designing a Lamb wave sensor using the AE effect.

2. A Si-based layered structure is commonly adopted when fabricating a Lamb wave microsensor. In this regard, influences of AE interactions on Lamb wave propagation in Si-based layered structures are analyzed before realizing the Si-based Lamb wave sensor. Numerical results show that in a $ZnO(0.5)/Si_3N_4(0.2)/SiO_2(0.2)$ laminated plate, velocity changes and attenuation of Lamb waves can be more than three times of SAW in a $ZnO(0.5)/Si_3N_4(0.2)/SiO_2(0.2)/Si(300)$ layered structure by choosing proper frequencies. Under this design, a $ZnO/Si_3N_4/SiO_2$ Lamb wave sensor using the AE interactions is a preferable candidate rather than a $ZnO/Si_3N_4/SiO_2/Si$ SAW sensor. Nevertheless, velocity changes and attenuation of Lamb waves in a $ZnO(0.5)/Si_3N_4(0.2)/SiO_2(0.2)/Si(5)$ laminated plate only differ slightly from those of SAW in a $ZnO(0.5)/Si_3N_4(0.2)/SiO_2(0.2)/Si(300)$ layered structure. For frequencies between 400 and 800MHz, velocity changes and attenuation of Lamb waves in $ZnO(0.5)/Si_3N_4(0.2)/SiO_2(0.2)/Si(5)$ are even smaller than those of SAW in $ZnO(0.5)/Si_3N_4(0.2)/SiO_2(0.2)/Si(300)$. Therefore, performances of a Si-based Lamb wave sensor depend strongly on both frequency and structure. When designing a Si-based Lamb wave sensor using the AE effect, thickness of each layer and the operating frequency must be properly chosen to ensure obvious velocity changes and attenuation due to AE interactions. Based on the analysis of the acoustoelectric-effect model for Lamb wave propagation presented in this work, a principle and method for designing a Lamb wave sensor using the AE effect is provided.

3. One of the objectives of this dissertation is to discuss the relation between the SAW

microsensor response and the AE effect. Comparing to the existing literature just using ZnO film as the sensing material, a ZnO-nanorad based SAW UV detector was demonstrated for the first time. Under a UV source of 365 nm, frequency shifts reached a maximum value of over 40 kHz; on the other hand, the UV detector was insensitive when a light source was outside of UV range. Frequency shifts was 19 kHz after 365 nm was switched on only for 10 s, much larger than the existing literature. Results show that performances of this UV detector such as repeatability, sensitivity, response time and environmental-fluctuation elimination are excellent. To further compare the measurement results with the theoretical model, SAW velocity changes of a value around 1% were calculated from measured frequency shifts and the values are approximate to the theoretical value of 1.3% at $\sigma_d = \sigma_m$, where the AE interactions occur. By substituting average velocity changes into equations associated with AE interactions, the average conductivities of ZnO sensing material under 365nm illuminations for a period of time were first calculated. The calculated conductivities were all around $2\times10^{-6}\Omega^{-1}$. Numerical results show that the AE interactions are effective when conductivities ranges from $7.63\times10^{-7}\Omega^{-1}$ to $7.63\times10^{-6}\Omega^{-1}$. In this case, by increasing conductivities of ZnO of the UV sensor, larger effect of acoustoelectric interactions can be further obtained. Therefore, the inversed calculation of ZnO conductivities in this work provides a further design consideration, such as adjusting deposition parameters of ZnO to increase conductivities, for a UV sensor in the future.

4. To discuss the influences of AE interaction on dispersive Lamb wave propagation, experimental investigations of Si-based Lamb wave UV microsensors were demonstrated for the first time. A $ZnO/Si_3N_4/Si$ and a ZnO/Si_3N_4 Lamb wave UV microsensor were designed. Results of the numerical analysis show that the attenuation of a ZnO/Si_3N_4 Lamb

wave sensor due to the AE effect is larger than that of a $ZnO/Si_3N_4/Si$ Lamb wave sensor. On the experimental side, under a 0.06 $mWcm^{-2}$ 370nm-UV illumination, a 0.8dB decrease of insertion loss (IL) of the ZnO/Si_3N_4 Lamb wave sensor and a only 0.1dB decrease of IL of the $ZnO/Si_3N_4/Si$ UV sensor were measured. After a time-gating process, a 1.8 dB drop of IL of the ZnO/Si_3N_4 Lamb wave sensor and a 0.8 dB drop of IL of the $ZnO/Si_3N_4/Si$ UV sensor were observed respectively. The experimental findings are in accordance with the numerical results.

5.2 Prospects

Several prospects which extends form this research are described as follows.

1. Influences of temperature on the AE interactions in theoretical calculations and experiments studied in this work were not included. For a semiconducting film, conductivity depends on temperature and sensing responses can be enhanced by heating the sensor when using AE interaction as the sensing mechanism. Thus, the temperature effect of the sensing material can be measured and discussed through proper experimental designs.

2. When fabricating a ZnO-based membrane Lamb wave microsensor, residual stress remains a critical issue. In this research, the stress of Si_3N_4 which was used as support membrane has been reduced by post-deposition annealing. However, residual stress of a ZnO thin film has not been solved yet. One of the possible solutions for reducing the stress of a ZnO thin film is by adjusting sputtering parameters such as RF power, temperature, gas flow rates and the distance between the target and the substrate. Another method to relieve ZnO stress is tuning the heat-treatment parameters such as temperature and time during post-deposition annealing process. These methods need full and organized experimental designs to find out parameters which are useful for reducing the stress of a

ZnO film.

3. The Lamb wave UV microsensors studied in this work was measured by a network analyzer. For a realistic application, a UV sensor based on a Lamb wave oscillator which can deal with relatively small frequency shift shows a preferable candidate. To form an oscillating circuit, the insertion loss of the Lamb wave devices must be improved first. The insertion loss can be enhanced by using the design method provided in this research, such as the choice of sensing material and the frequency-thickness product of a structure. Performance of a Lamb wave sensor can also be improved by the deposition technique of the sensing material and the technique of fabrication process. Furthermore, silicon-based acoustic wave sensors and electric circuits can be integrated into a single chip by combining CMOS and MEMS technologies in the future.

4. By combining different sensing films and sensing targets, various applications such as light, gas, bio-sensing of surface and Lamb wave microsensors using AE interaction can be explored. For example, a ZnO nanostructure was employed to achieve a highly-sensitive SAW UV sensor in this research. Similarly, ZnO nanostructures grown on a Lamb wave UV microsensor can be further designed and realized. Furthermore, various sensing material with nanostructures can be employed in surface and Lamb wave microsensors for exploring novel applications.

Appendix A

This appendix introduces the details of elastic wave propagations affected by acoustoelectric interaction in an unbounded piezoelectric semiconductor.

A.1 Piezoelectric Constitutive Relations and Equations of Motion

A solid with piezoelectricity becomes electrically polarized under the action of a mechanical force, called the direct piezoelectric effect which was discovered by the Curies in 1880. On the contrary, the inverse piezoelectric effect is that a piezoelectric solid becomes mechanically deformed when an electric field is applied. The generalized constitutive relations[84] in index notation are written as

$$\tau_{ij} = C_{ijkl} S_{kl} - e_{lij} E_l \tag{A.1}$$

$$D_i = e_{ikl} S_{kl} + \varepsilon_{il} E_l \tag{A.2}$$

where τ_{ij} is the stress field, D_i is the electric displacement field, S_{kl} is the strain field, E_l is the electric field, and C_{ijkl}, e_{lij}, and ε_{il} are elastic stiffness constants, piezoelectric constants, and permittivity, respectively. Equations (A.1) and (A.2) reveal that mechanical stress and electric displacement are described in terms of the independent variables electric field and strain field.

For acoustic wave propagation in a piezoelectric semiconducting medium, the mechanical displacement of an arbitrary point with position $\mathbf{r}$, varying with time t, can be denoted as $u_i(\mathbf{r},t)$. The equation of motion from Newton's law with neglecting the body force are given by

$$\tau_{ij,j} = \rho \ddot{u}_i \tag{A.3}$$

where $\mathbf{r} = (x_1, x_2, x_3)$ is the position vector and ρ is the mass density.

In a piezoelectric semiconducting solid, the electric and mechanical variables are interdependent, which implies a coupling between elastic field and electromagnetic field. These fields can in principle be determined only by solving the equations both of Newton and Maxwell simultaneously, and the solutions are mixed elasto-electromagnetic waves. In practice, the elastic wave velocity accompanied by electric field is 10^4 to 10^5 times smaller than the electromagnetic wave velocity which is accompanied by mechanical strain. Consequently, the magnetic field associated with mechanical vibrations can be negligible. This implies that the electromagnetic filed associated with an electric field is quasi-static. Therefore, the Maxwell's equations can be approximated as

$$\nabla\times\mathbf{E}=-\frac{\partial\mathbf{B}}{\partial t}\cong 0 \quad \text{giving} \quad \mathbf{E}=-\nabla\phi \tag{A.4}$$

As in electrostatics, the field **E** can thus be derived from the electric potential ϕ. In this study, the propagation of elastic waves in a piezoelectric semiconducting medium is with the assumption called quasi-static approximation.

Under quasi-static approximation, substituting the strain $S_{kl}=1/2\left(u_{k,l}+u_{l,k}\right)$ and the electric field $E_l=-\phi_{,l}$, Eq. (A.1) and (A.2) can be rewritten as

$$\tau_{ij}=C_{ijkl}u_{k,l}+e_{lij}\phi_{,l} \tag{A.5}$$

$$D_i=e_{ikl}u_{k,l}-\varepsilon_{il}\phi_{,l} \tag{A.6}$$

A.2 Poisson's Equation and the Continuity Equation

In the previous section, equations of motion and the constitutive relations of piezoelectric semiconductors are described. To solve the wave equation, the effect of mobile carriers must be taken into account. The two laws which are of use in connecting the mechanical displacements to mobile carriers are Poisson's equation and the continuity equation.

Poisson's equation, equivalent to Gauss' law for the electric field, is

$$D_{i,i} = Q \tag{A.7}$$

where D_i is the electric displacement field and Q is the volume density of free charge. (coulomb per meter cubed). Eq. (A.7) describes that the divergence of the displacement flux density is equal to the free charge density. The continuity equation, also known as the law of conservation of charge, is given by

$$J_{i,i} = -\dot{Q} \tag{A.8}$$

where J_i is the volume current density, or simply called current density (amperes per meter square). The continuity equation states that the divergence of the current density due to flow of charges is equal to the time rate of decrease of the charge density.

The free charge density Q can be written as[13]

$$Q = -qn_s \tag{A.9}$$

where q is the magnitude of the electronic charge, and n_s is the number of electrons per unit volume required to produce the free charge Q.

To simplify the model, only an n type of extrinsic semiconductor is considered [13]. The current density for such type of material can be expressed as

$$J_i = -q(n + fn_s)\mu_{ij}\phi_{,j} + \frac{f}{\beta}\mu_{ij}n_{s,j} \tag{A.10}$$

The first term is the drift term due to an applied electric field, and the second is diffusion due to thermal energy. n is the mean current density, f is the fraction of the acoustically produced space charge which is mobile, μ_{ij} is the electron mobility, $\beta = (\mathrm{k}T)^{-1}$ is the constant related to Boltzmann's constant k and temperature T.

After introducing several important equations describing acoustic and electric fields,

the coupling effect of acoustic and electric fields can be obtained through wave equations of a piezoelectric semiconductor.

A.3 Wave Equations of a Piezoelectric Semiconductor

From the equation of motion Eq. (A.3) and the constitutive relation Eq. (A.5), one can write

$$\tau_{ij,j} = C_{ijkl}u_{k,lj} + e_{lij}\phi_{,lj} = \rho\ddot{u}_i \tag{A.11}$$

By combining Eq. (A.6), (A.7), and Eq. (A.9), the electric displacement which correlates the mechanical displacement and the free charge density is given by

$$D_{i,i} = e_{ikl}u_{k,li} - \varepsilon_{il}\phi_{,li} = -qn_s \tag{A.12}$$

From Eq. (A.12), the n_s, the number of electrons required to produce the free charge Q, can be written as

$$n_s = -\frac{1}{q}\left[e_{ikl}u_{k,li} - \varepsilon_{il}\phi_{,li}\right] \tag{A.13}$$

Moreover, by combining the continuity equation Eq. (A.8) with Eq. (A.10), one can get

$$J_{i,i} = -q(n + fn_s)\mu_{ij}\phi_{,ji} + \frac{f}{\beta}\mu_{ij}n_{s,ji} = q\dot{n}_s \tag{A.14}$$

Substitute Eq. (A.13) into Eq. (A.14), one can written

$$-qn\mu_{ij}\phi_{,ji} + \frac{f\mu_{ij}}{q\beta}\varepsilon_{pl}\phi_{,lpji} - \frac{\partial}{\partial t}\varepsilon_{pl}\phi_{,lp} = -\frac{\partial}{\partial t}\left[e_{pkl}u_{k,lp}\right] + \frac{f\mu_{ij}}{q\beta}e_{pkl}u_{k,lpji} \tag{A.15}$$

Rewrite Eq. (A.11) and Eq. (A.15), we can get the wave equations of a piezoelectric semiconducting material, which give

$$
\begin{cases}
\rho \ddot{u}_i = C_{ijkl} u_{k,lj} + e_{lij} \phi_{,lj} \\
\dfrac{\partial}{\partial t}\left[\varepsilon_{pl} \phi_{,lp} \right] - \dfrac{f \mu_{ij}}{q\beta} \varepsilon_{pl} \phi_{,lpji} + qn\mu_{ij} \phi_{,ji} = \dfrac{\partial}{\partial t}\left[e_{pkl} u_{k,lp} \right] - \dfrac{f \mu_{ij}}{q\beta} e_{pkl} u_{k,lpji}
\end{cases}
\tag{A.16}
$$

As can be seen in Eq. (A.16), the forms are similar to the wave equations of a piezoelectric insulator. If the material is piezoelectric but not semiconducting, i.e., the mobility μ_{ij} can be neglected, these two equations in Eq. (A.16) reduce to piezoelectric wave equations.

Consider a plane wave propagating in the piezoelectric semiconducting media, the solutions are proportional to a complex wave function $\exp[i(\omega t - k\hat{\ell} \bullet \mathbf{r})]$, where ω is the circular frequency, k is the wave number, $\hat{\ell} = \ell_x \hat{x} + \ell_y \hat{y} + \ell_z \hat{z}$ represents a unit vector in the propagation direction, and $\mathbf{r}=(x, y, z)$ is the position vector.

Thus the equations in Eq. (A.16) can be reduced as

$$
\rho \omega^2 u_i = k^2 \ell_l C_{ijkl} \ell_j u_k + k^2 \ell_l e_{lij} \ell_j \phi
\tag{A.17}
$$

and

$$
\left[i\omega \ell_l \varepsilon_{pl} \ell_p + k^2 \frac{f \ell_i \mu_{ij} \ell_j}{q\beta} \ell_p \varepsilon_{pl} \ell_l + qn \ell_j \mu_{ij} \ell_i \right] \phi =
\left[i\omega \ell_l e_{pkl} \ell_p + k^2 \frac{f \ell_j \mu_{ij} \ell_i}{q\beta} \ell_p e_{pkl} \ell_l \right] u_k
\tag{A.18}
$$

After substitution Eq. (A.18) into Eq. (A.17) and some rearrangement of terms, we have

$$
\rho \omega^2 u_i = k^2 \bar{C}_{ijkl} u_k
\tag{A.19}
$$

where

$$
\bar{C}_{ijkl} = \ell_l C_{ijkl} \ell_j + \frac{ i\omega \ell_r e_{ris} \ell_s \ell_l e_{pkl} \ell_p + k^2 \dfrac{f \ell_i \mu_{ij} \ell_j}{q\beta} \ell_l e_{pkl} \ell_p \ell_r e_{ris} \ell_s }{ i\omega \ell_p \varepsilon_{pl} \ell_l + k^2 \dfrac{f \ell_j \mu_{ij} \ell_i}{q\beta} \ell_p \varepsilon_{pl} \ell_l + qn \ell_j \mu_{ij} \ell_i }
\tag{A.20}
$$

is the complex elastic constant with diffusion effect. If the material is not semiconducting, i.e. μ_{ij} is negligible, $\bar{C}_{ijkl}$ can be reduced to piezoelectrically stiffened elastic constant.[8]

A.4 Acoustoelectric Effect of a Piezoelectric Semiconductor

Define a conductivity frequency $\omega_{C_{ij}}$, which is also called relaxation frequency, be the ratio between conductivity $\sigma_{ij} = nq\mu_{ij}$ and permittivity ε_{ij}, and define diffusion frequency be $\omega_{D_{ij}} = (q\beta/f\mu_{ij})(\omega/k)^2$ [13], which is associated with the diffusion coefficient $\mu_{ij}/q\beta$ in a semiconductor. Then Eq. (A.20) can be rewritten as

$$\bar{C}_{ijkl} = \ell_l C_{ijkl} \ell_j + \frac{\ell_r e_{ris} \ell_s \ell_l e_{pkl} \ell_p}{\ell_p \varepsilon_{pl} \ell_l} \frac{1 + \dfrac{\ell_i \omega_{C_{ij}} \ell_j}{\ell_i \omega_{D_{ij}} \ell_j} + \left(\dfrac{\omega}{\ell_i \omega_{D_{ij}} \ell_j}\right)^2 + i \dfrac{\ell_i \omega_{C_{ij}} \ell_j}{\omega}}{1 + 2\left(\dfrac{\ell_i \omega_{C_{ij}} \ell_j}{\ell_i \omega_{D_{ij}} \ell_j}\right) + \left(\dfrac{\omega}{\ell_i \omega_{D_{ij}} \ell_j}\right)^2 + \left(\dfrac{\ell_i \omega_{C_{ij}} \ell_j}{\omega}\right)^2} \quad \text{(A.21)}$$

Now, consider that acoustic waves propagates along the x-direction, $\hat{\ell} = \hat{x}$, $\ell_x = [1\ 0\ 0]$, then the expression of $\bar{C}_{ijkl}$ is reduced as

$$\bar{C}_{i1k1} = C_{i1k1} \left\{ 1 + \frac{e_{1i1} e_{1k1}}{C_{i1k1} \varepsilon_{11}} \left[\frac{1 + \dfrac{\omega_{C_{11}}}{\omega_{D_{11}}} + \left(\dfrac{\omega}{\omega_{D_{11}}}\right)^2 + i \dfrac{\omega_{C_{11}}}{\omega}}{1 + 2\left(\dfrac{\omega_{C_{11}}}{\omega_{D_{11}}}\right) + \left(\dfrac{\omega}{\omega_{D_{11}}}\right)^2 + \left(\dfrac{\omega_{C_{11}}}{\omega}\right)^2} \right] \right\} \quad \text{(A.22)}$$

If we further assume conductivity frequency and diffusion frequency are isotropic and drop the subscript for convenience, Eq. (A.22) can be expressed as

$$\bar{C} = C\left\{1+\frac{e^2}{C\varepsilon}\left[\frac{1+(\omega_C/\omega_D)+(\omega/\omega_D)^2+i(\omega_C/\omega)}{1+2(\omega_C/\omega_D)+(\omega/\omega_D)^2+(\omega_C/\omega)^2}\right]\right\} \tag{A.23}$$

Using the complex elastic constant in Eq. (A.23), one can obtain acoustic propagating properties of a piezoelectric semiconductor with isotropic conductivity and mobility in which waves propagate along the *x*-direction.

Velocity and absorption constants in terms of $\bar{C}$ [13] are

$$v = v_0 \operatorname{Re}(\bar{C}/C)^{1/2},\ v_0 = (C/\rho)^{1/2} \tag{A.24}$$

$$\Gamma = \frac{\omega}{v_0} C^{1/2} \operatorname{Im}\left(\bar{C}^{-1/2}\right) \tag{A.25}$$

Where $v_0 = (C/\rho)^{1/2}$ is an acoustic velocity in a nonpiezoelectric insulator. Since $e^2/C\varepsilon = K^2/(1-K^2) \cong K^2$ is small ($K^2 \ll 1$), where K^2 is the electromechanical coupling coefficient, the velocity would be

$$v = v_0\left\{1+\frac{K^2}{2}\left[\frac{1+(\omega_C/\omega_D)+(\omega/\omega_D)^2}{1+2(\omega_C/\omega_D)+(\omega/\omega_D)^2+(\omega_C/\omega)^2}\right]\right\} \tag{A.26}$$

and absorption constant is

$$\Gamma = \frac{\omega}{v_0}\frac{K^2}{2}\left[\frac{\omega_C/\omega}{1+2(\omega_C/\omega_D)+(\omega/\omega_D)^2+(\omega_C/\omega)^2}\right] \tag{A.27}$$

Eq. (A.26) and (A.27) represent the propagation properties of bulk acoustic waves in a piezoelectric semiconducting medium. As defined before, on can write conductivity frequency as $\omega_C = \sigma/\varepsilon$ and diffusion frequency as $\omega_D = (q\beta/f\mu)(\omega/k)^2$. Therefore, Eq. (A.26) and (A.27) indicate that acoustic wave velocity and acoustic loss are modulated by conductivity and mobility of the material.

To reveal the effects of acoustoelectric interaction, three cases, $\omega_C \gg \omega_D$, $\omega_C = \omega_D$ and

$\omega_C \ll \omega_D$ are discussed. In the following, CdS, a piezoelectric semiconductor of hexagonal symmetry is used as an example here; and the wave propagating along the hexagonal axis, also called C axis, is considered.

(1) $\omega_C \gg \omega_D$:

The case which the conductivity frequency ω_C is much larger than the diffusion frequency ω_D means that the conductivity is large and the diffusivity which is to smooth out carrier fluctuations can not be neglected. If $\omega_C = 100\omega_D$, the curves of velocity and loss are shown in Fig. A.1. The x axis is the ratio of acoustic circular frequency ω and ω_C. The vertical axis on the left side represents acoustic loss, in the form of the acoustic loss over ω/v_0 in units of $K^2/2$. On the right side, the vertical axis indicates acoustic velocity variation in terms of $v - v_0/v_\infty - v_0$, where $v_\infty = v_0\left(1 + e^2/2C\varepsilon\right)$ is the acoustic velocity in a pure piezoelectric insulator. In Fig. A.1, the velocity variation shows that the value ranges from v_0 to v_∞, which means that under acoustoelectric interaction, the maximum acoustic velocity is the velocity of a pure piezoelectric medium, and the minimum acoustic velocity equals to the velocity of a nonpiezoelectric material. The red circle in the figure shows the velocity $v = v_0 + v_\infty/2$ occurs at $\omega = 0.1\omega_C$. The triangle shows that the maximum loss occurs at the frequency smaller than $0.1\omega_C$. The maximum loss is smaller than $0.05\left(K^2/2\right)$, which means when $\omega_C \gg \omega_D$, the acoustic loss resulting from acoustoelectric interaction is not obvious. Therefore, when the conductivity frequency is much larger than diffusion frequency, the acoustoelectric effect is not strong and is hard for the use of real application.

(2) $\omega_C = \omega_D$:

Fig. A.2 shows acoustic velocity and loss when the conductivity frequency ω_C is equal to the diffusion frequency ω_D. The two vertical axes represent the same meaning with case (1), $\omega_C \gg \omega_D$. Acoustic velocity also varies from v_0 to v_∞, as in the case. However, acoustic loss becomes larger compared with the case of $\omega_C \gg \omega_D$. The maximum acoustic loss which occurs at $\omega \simeq \omega_C$ is six times larger than that of the case $\omega_C \gg \omega_D$.

(3) $\omega_C \ll \omega_D$:

When the condition $\omega_D \gg \omega_C, \omega$ is satisfied, Eq. (A.26) and (A.27) can be further reduced as

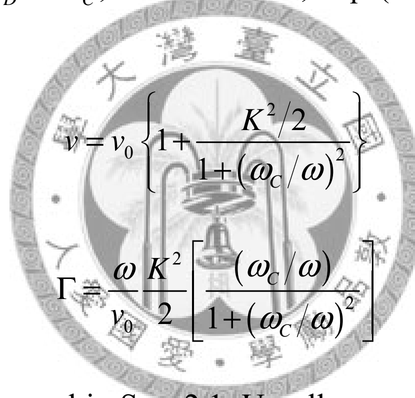

$$v = v_0 \left\{ 1 + \frac{K^2/2}{1+(\omega_C/\omega)^2} \right\} \tag{A.28}$$

$$\Gamma = \frac{\omega}{v_0}\frac{K^2}{2}\left[\frac{(\omega_C/\omega)}{1+(\omega_C/\omega)^2}\right] \tag{A.29}$$

This is in fact the case discussed in Sec. 2.1. Usually, ω_D for a given temperature can be treated as a constant. For n-type CdS, ω_D at 300K is in the order of 10^{10} and the term (ω/k) in ω_D are relatively small changes which can be ignored. High ω_D means that diffusion coefficient $\mu_{ij}/q\beta$ is small and carrier diffusion can thus be neglected. Fig. A.3 illustrates velocity dispersion and loss when ignoring diffusion of carriers. The velocity variation shows that the value goes from v_0 to v_∞ as the previous cases. When acoustic frequencies are very low, the velocity is equal to v_0; while at high frequencies, the velocity is v_∞. Acoustic loss approaches to zero at very high or low frequencies. For example, when ω is much lower than ω_C, the dielectric relaxation time is short that the

carriers can redistribute rapid enough to screen the piezoelectric field, thus the velocity is equal to v_0. On the contrary, when $\omega \gg \omega_C$, the relaxation time is too long that the material act as an insulator and the velocity is v_∞.The maximum acoustic loss occurs at $\omega = \omega_C$, and the term $\Gamma v_0/\omega$ which is associated with acoustic loss has a maximum value of $K^2/4$, as the triangle indicated in Fig. A.3. From the discussion of case (1) to case (3), acoustic loss increases when diffusion frequency comparing to conductivity frequency becomes higher, and the maximum loss is $K^2/4$. The velocity $v = v_0 + v_\infty/2$ occurs at $\omega = \omega_C$, as the red circle shown in the figure. As shown in Fig. A.3, acoustic loss and the slope of velocity change is largest at frequencies around $\omega = \omega_C$, which indicates that the AE interaction is strong around $\omega = \omega_C$; while at high or low frequencies, the AE effect are not obvious.

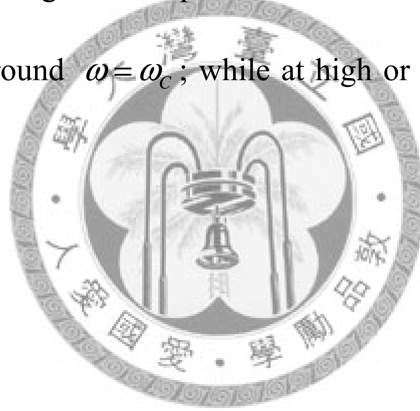

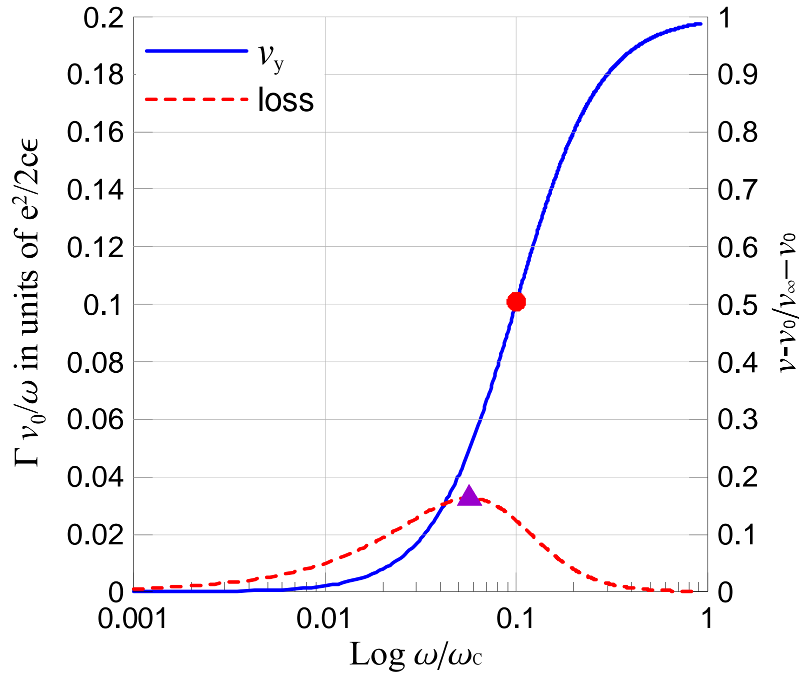

Fig. A.1 Acoustic velocity and loss when conductivity frequency is much larger than diffusion frequency

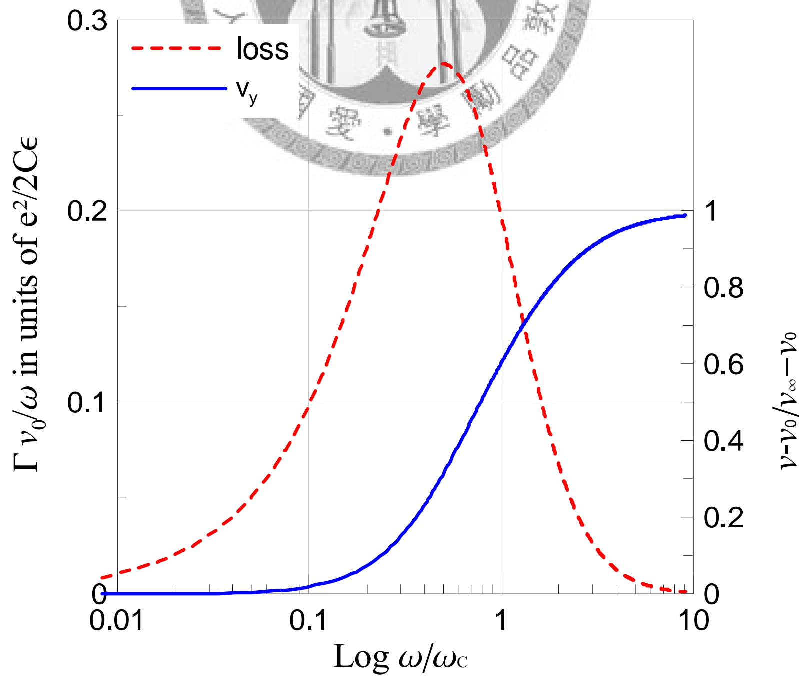

Fig. A.2 Acoustic velocity and loss when conductivity frequency is equal to diffusion frequency

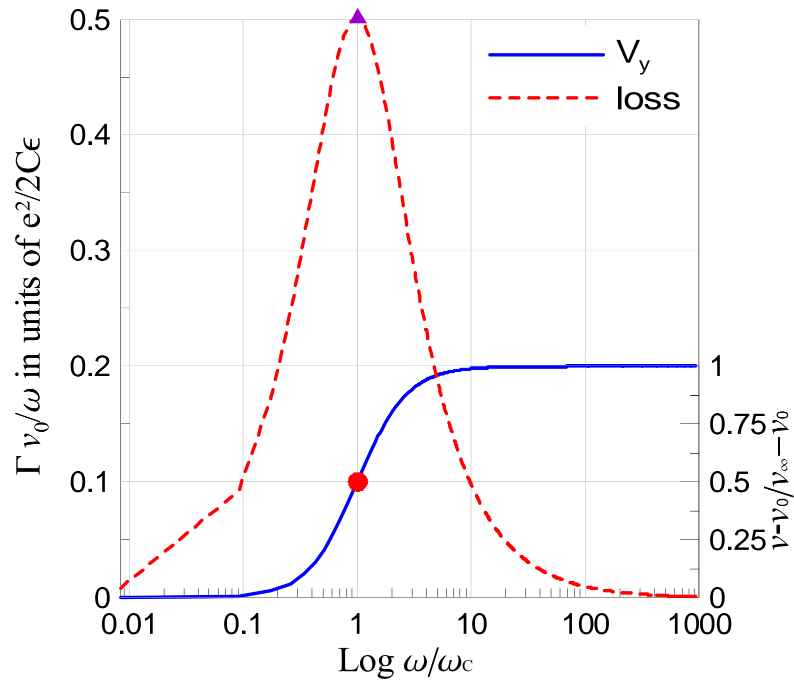

Fig. A.3 Acoustic velocity and loss when conductivity frequency is much smaller than diffusion frequency

Appendix B

This appendix gives the coordinate transformation which is used for calculations of material constants of anisotropic materials.

Common piezoelectric insulators or piezoelectric semiconductors are anisotropic crystals, which indicate that the acoustic characteristics depend on crystal cuts and the direction of wave propagations. Therefore, material constants of piezoelectric semiconductors should be transformed into the corresponding crystal cuts and propagation axis then calculated through the coordinate transformation.

Consider a material with piezoelectric anisotropy, as shown in Fig. B.1, (x, y, z) is the specimen coordinate, where the z axis perpendicular to the surface of the specimen represents the normal of the cut of the crystal and the x axis represents the wave propagation. In Fig. B.2, (X, Y, Z) represents the crystallographic reference frame. When the crystal cut and the direction of propagation are not consistent with the crystallographic coordinate system, the Euler angles (ϕ, θ, ψ) which follow IEEE standard on piezoelectricity published in 1978 are used to rotate the material into the specimen coordinate system. The rotation follows the Z-X-Z convention, where ϕ describes the first counterclockwise rotation around the Z axis, θ is the second counterclockwise rotation around the new X axis. These two rotations rotate the crystallographic coordinate to the cut of the crystal. Finally, ψ describes the third counterclockwise rotation around the new Z axis and the crystallographic coordinate is transformed into the direction of wave propagation. The relationship between the specimen coordinate and the crystallographic coordinate system is

$$\begin{Bmatrix} X \\ Y \\ Z \end{Bmatrix} = \left[a_{ij} \right] \bullet \begin{Bmatrix} x \\ y \\ z \end{Bmatrix} \tag{B.1}$$

where the corresponding transformation matrix $\left[a_{ij} \right]$ is

$$\left[a_{ij} \right] = \begin{bmatrix} \cos\psi & \sin\psi & 0 \\ -\sin\psi & \cos\psi & 0 \\ 0 & 0 & 1 \end{bmatrix} \bullet \begin{bmatrix} 1 & 0 & 0 \\ 0 & \cos\theta & \sin\theta \\ 0 & -\sin\theta & \cos\theta \end{bmatrix} \bullet \begin{bmatrix} \cos\phi & \sin\phi & 0 \\ -\sin\phi & \cos\phi & 0 \\ 0 & 0 & 1 \end{bmatrix} \tag{B.2}$$

The elastic stiffness constants C_{ijkl}, piezoelectric constants e_{ijk}, permittivity ε_{ij}, conductivity σ_{ij}, and mobility μ_{ij} in a specimen coordinate can be calculated from the coefficients in the crystallographic coordinate through coordinate transformation, and the general relations are

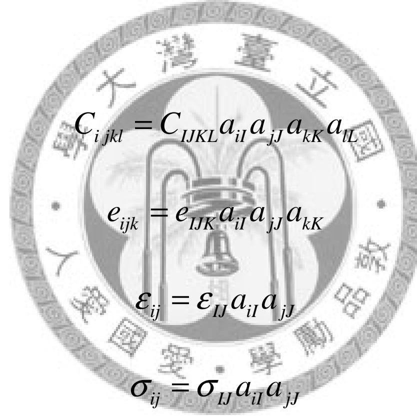

$$C_{ijkl} = C_{IJKL} a_{iI} a_{jJ} a_{kK} a_{lL} \tag{B.3}$$

$$e_{ijk} = e_{IJK} a_{iI} a_{jJ} a_{kK} \tag{B.4}$$

$$\varepsilon_{ij} = \varepsilon_{IJ} a_{iI} a_{jJ} \tag{B.5}$$

$$\sigma_{ij} = \sigma_{IJ} a_{iI} a_{jJ} \tag{B.6}$$

$$\mu_{ij} = \mu_{IJ} a_{iI} a_{jJ} \tag{B.7}$$

where $I, J, K, L, i, j, k, l = 1,2,3$

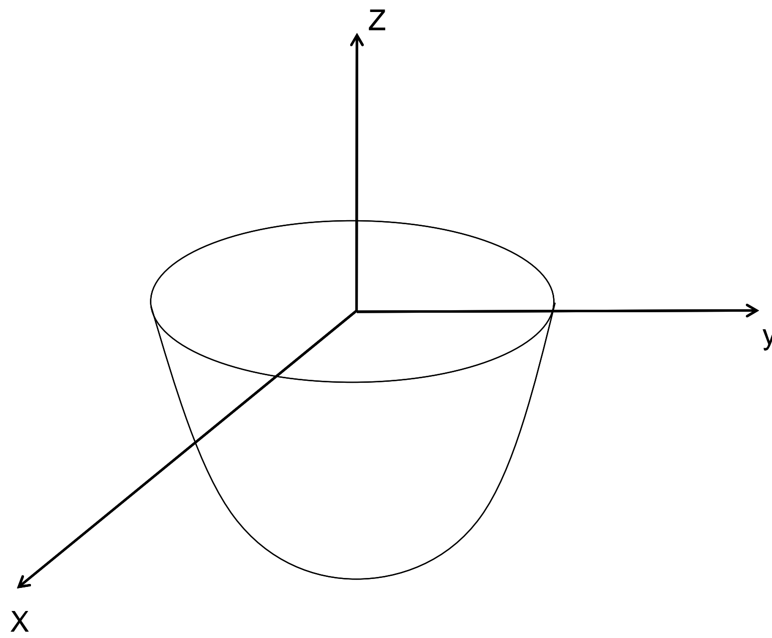

Fig B.1 Specimen coordinate system

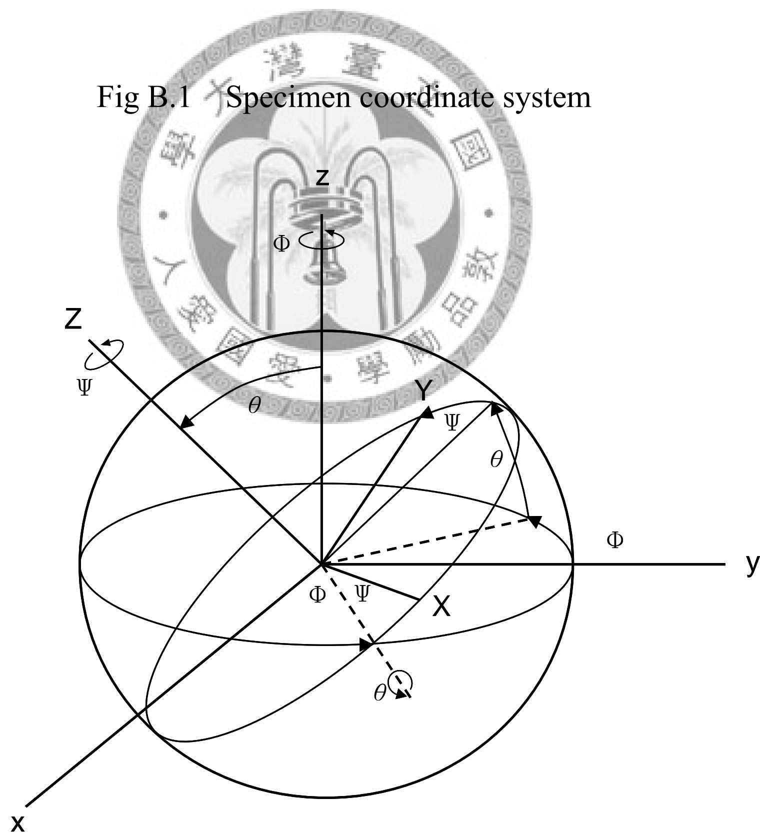

Fig. B.2 Euler angles between specimen and crystalline coordinate system

REFERENCES

[1] J. W. Gardner, V. K. Varadan, and O. O. Awadelkarim, *Microsensors, MEMS and Smart Devices* (Wiley, New York, 2001).

[2] Electronics.caResearchNetwork, in *Global microsensors market slated for high growth through 2013* (Electronics.ca Publications, 2008).

[3] D. S. Ballantine Jr., R. M. White, S. J. Martin et al., *Acoustic Wave Sensors: Theory, Design, & Physico-Chemical Applications*. (Academic Press, San Diego, 1997).

[4] B. Drafts, "Acoustic wave technology sensors," Microwave Theory and Techniques, IEEE Transactions on **49** (4), 795 (2001).

[5] F. Hassani, O. Tigli, S. Ahmadi et al., "Integrated CMOS surface acoustic wave gas sensor: design and characteristics," Sensors, 2003. Proceedings of IEEE **2**, 1199 (2003).

[6] S. Ahmadi, C. Korman, M. Zaghloul et al., "CMOS integrated gas sensor chip using SAW technology," Circuits and Systems, 2003. ISCAS '03. Proceedings of the 2003 International Symposium **4**, 848 (2003).

[7] A. Polh, "A review of wireless SAW sensors," Ultrasonics, Ferroelectrics and Frequency Control, IEEE Transactions on **47** (2), 317 (2000).

[8] B. A. Auld, *Acoustic Fields and Waves in Solids*. (Krieger Pub Co, Malabar, 1990).

[9] L. Rayleigh, "On waves propagated along the plane surface of an elastic solid," Proc. London Math. Soc. **s1-17** (1), 4 (1885).

[10] H. Lamb, "On Waves in an elastic plate," Proceedings of the Royal Society of London. Series A, Containing Papers of a Mathematical and Physical Character **93** (648), 114 (1917).

[11] R. M. White and F. W. Voltmer, "Direct piezoelectric coupling to surface elastic waves," Applied Physics Letters **7** (12), 314 (1965).

[12] K. A. Ingebrigtsen, "Linear and nonlinear attenuation of acoustic surface waves in a piezoelectric coated with a semiconducting film," Journal of Applied Physics **41** (2), 454 (1970).

[13] A. R. Hutson and D. L. White, "Elastic wave propagation in piezoelectric semiconductors," Journal of Applied Physics **33** (1), 40 (1962).

[14] A. J. Ricco, S. J. Martin, and T. E. Zipperian, "Surface acoustic wave gas sensor based on film conductivity changes," Sensors and Actuators **8**, 319 (1985).

[15] J. F. Vetelino, R. K. Lade, and R. S. Falconer, "Hydrogen sulfide surface acoustic wave gas detector," IEEE 1986 Ultrasonics Symposium, 549 (1986).

[16] M. Penza and L. Vasanelli, "SAW NOx gas sensor using WO3 thin-film sensitive coating," Sensors and Actuators B: Chemical **41** (1-3), 31 (1997).

[17] R. Giriunuene and E. Garska, "Acoustoelectric gas sensor with casserite film," Ultragarsas **35** (2), 27 (2000).

[18] S. J. Ippolito, A. Ponzoni, K. Kalantar-Zadeh et al., "Layered WO3/ZnO/36degree-LiTaO3 SAW gas sensor sensitive towards ethanol vapour and humidity," Sensors and Actuators B: Chemical **117** (2), 442 (2006).

[19] F. C. Huang et al., "A room temperature surface acoustic wave hydrogen sensor with Pt coated ZnO nanorods," Nanotechnology **20** (6), 065501 (2009).

[20] D. Ciplys, R. Rimeika, M. S. Shur et al., "Visible--blind photoresponse of GaN-based surface acoustic wave oscillator," Applied Physics Letters **80** (11), 2020 (2002).

[21] E. Monroy et al., "Wide-bandgap semiconductor ultraviolet photodetectors," Semiconductor Science and Technology **18** (4), R33 (2003).

[22] P. Sharma and K. Sreenivas, "Highly sensitive ultraviolet detector based on ZnO/LiNbO3 hybrid surface acoustic wave filter," Applied Physics Letters **83** (17), 3617 (2003).

[23] F. Calle, T. Palacios, J. Pedros et al., "Surface-acoustic-wave-controlled photodetectors," Proceedings of SPIE **5502**, 439 (2004).

[24] Nuri W. Emanetoglu, J. Zhu, Y. Chen et al., "Surface acoustic wave ultraviolet photodetectors using epitaxial ZnO multilayers grown on r-plane sapphire," Apply Physics Letters **85** (17), 3702 (2004).

[25] Z. Xu, H. Deng, J. Xie et al., "Photoconductive UV detectors based on ZnO films prepared by sol-gel method," Journal of Sol-Gel Science and Technology **36** (2), 223 (2005).

[26] D. Y. Song et al., "247nm solar-blind ultraviolet p-i-n photodetector," Journal of Applied Physics **100** (9), 096104 (2006).

[27] C. Jiafa et al., "High-performance 4H-SiC-based ultraviolet p-i-n photodetector," Journal of Applied Physics **102** (2), 024505 (2007).

[28] L. Ying et al., "High responsivity 4H-SiC based metal-semiconductor-metal ultraviolet photodetectors," Science in China Series G Physics Mechanics and Astronomy **51** (11), 1616 (2008).

[29] R. Fabrizio et al., "Electro-optical response of ion-irradiated 4H-SiC Schottky ultraviolet photodetectors," Applied Physics Letters **92** (9), 093505 (2008).

[30] J. Kondoh and S. Shiokawa, presented at the Ultrasonics Symposium, 1993. Proceedings., IEEE 1993, 1993 (unpublished).

[31] Z. A. Shana and F. Josse, "Quartz crystal resonators as sensors in liquids using the acoustoelectric effect," Analytical Chemistry **66** (13), 1955 (2002).

[32] R. H. Parmenter, "The acousto-electric effect," Physical Review **89** (5), 990 (1953).

[33] C. Kittel, "An electron transfer mechanism for ultrasonic attenuation in metals," Acta Metallurgica **3** (3), 295 (1955).

[34] W. P. Mason, "Ultrasonic attenuation due to lattice-electron -interaction in normal

conducting metals," Physical Review **97** (2), 557 (1955).

[35] R. W. Morse, "Ultrasonic attenuation in metals by electron relaxation," Physical Review **97** (6), 1716 (1955).

[36] A. Van Den Beukel, "On the theory of the acousto-electric effect," Applied Scientific Research **5** (1), 459 (1956).

[37] G. Weinreich, "Acoustodynamic effects in semiconductors," Physical Review **104** (2), 321 (1956).

[38] G. Weinreich, T. M. Sanders, and H. G. White, "Acoustoelectric effect in n-type germanium," Physical Review **114** (1), 33 (1959).

[39] A. R. Hutson, "Piezoelectricity and conductivity in ZnO and CdS," Physical Review Letters **4** (10), 505 (1960).

[40] H. Jaffe, D. Berlincourt, H. Krueger et al., "Piezoelectric Properties of Cadmium Sulfide Crystals," Proceedings of the 14th Annual Symposium on Frequency Control, 19 (1960).

[41] W. C. Wang, "Strong Acoustoelectric Effect in CdS," Physical Review Letters **9** (11), 443 (1962).

[42] K. Blotekjaer and C. F. Quate, "The coupled modes of acoustic waves and drifting carriers in piezoelectric crystals," Proceedings of the IEEE **52** (4), 360 (1964).

[43] J. S. A. Wixforth, M. Wassermeier, and J.P.Kotthaus, "Surface acoustic waves on GaAs/AlGaAs heterostructures," Physical Review B **40** (11) (1989).

[44] R. Adler, "Simple theory of acoustic amplification," IEEE Trans. Sonics and Ultrason. **su-18** (3) (1971).

[45] H. Hanebrekke and K. A. Ingebrigtsen, "Acoustoelectric amplification of surface waves in structure of cadmium-selenide film on lithium niobate," Electronics Letters **6** (16), 520 (1970).

[46] I. M. Asher and M. O. Scully, "Acoustoelectric amplification-a phonon-laser approach: theory of a single acoustic mode," Physical Review A **8** (4), 1988 (1973).

[47] G. S. Kino, "Acoustoelectric interactions in acoustic-surface-wave devices," Proceedings of the IEEE **64** (5), 724 (1976).

[48] J. S. Yang and H. G. Zhou, "Acoustoelectric amplification of piezoelectric surface waves," Acta Mechanica **172** (1), 113 (2004).

[49] I. J. Fritz, "Transverse acoustoelectric effect in the separated-medium surface-wave configuration," Journal of Applied Physics **52** (11), 6749 (1981).

[50] F. Palma and P. K. Das, "Acoustoelectric interaction in layered semiconductor," Ultrasonics, Ferroelectrics and Frequency Control, IEEE Transactions on **34** (3), 376 (1987).

[51] P. E. Lippens, M. Lannoo, and J. F. Pouliquen, "Calculation of the transverse acoustoelectric voltage in a piezoelectric-extrinsic semiconductor structure," Journal of Applied Physics **66** (3), 1209 (1989).

[52] V. A. Vyun, presented at the Ultrasonics Symposium, 1994 Proceedings, 1994 IEEE, 1994 (unpublished).

[53] A. O. Govorov, A. V. Kalameitsev, M. Rotter et al., "Nonlinear acoustoelectric transport in a two-dimensional electron system," Physical Review B **62** (4), 2659 (2000).

[54] H. J. Kutschera, A. Wixforth, A. V. Kalameitsev et al., presented at the Ultrasonics Symposium, 2001 IEEE, 2001 (unpublished).

[55] T. M. Niemczyk, S. J. Martin, G. C. Frye et al., "Acoustoelectric interaction of plate modes with solutions," Journal of Applied Physics **64** (10), 5002 (1988).

[56] C. H. Yang and C. J. Shue, "Guided waves propagating in a piezoelectric plate immersed in a conductive fluid," IEEE Ultrasonics Symposium, 415 (1998).

[57] Y. C. Lee and S. H. Kuo, "Leaky Lamb wave of a piezoelectric plate subjected to

conductive fluid loading: Theoretical analysis and numerical calculation," Journal of Applied Physics **100** (7), 073519 (2006).

[58] J. Yang, X. Yang, and J. Turner, "Amplification of acoustic waves in laminated piezoelectric semiconductor plates," Archive of Applied Mechanics **74** (3), 288 (2004).

[59] D. L. White, "Amplification of ultrasonic waves in piezoelectric semiconductors," Journal of Applied Physics **33** (8), 2547 (1962).

[60] S. Urabe, "Voltage controlled monolithic SAW phase shifter and its application to frequency variable oscillator," Sonics and Ultrasonics, IEEE Transactions on **29** (5), 255 (1982).

[61] M. Rotter, W. Ruile, G. Scholl et al., "Novel concepts for GaAs/LiNbO3 layered systems and their device applications," Ultrasonics, Ferroelectrics and Frequency Control, IEEE Transactions on **47** (1), 242 (2000).

[62] J. Zhu, Y. Chen, G. Saraf et al., "Voltage tunable surface acoustic wave phase shifter using semiconducting/piezoelectric ZnO dual layers grown on r-Al2O3," Applied Physics Letters **89** (10), 103513 (2006).

[63] G. N. Saddik, D. S. Boesch, S. Stemmer et al., "dc electric field tunable bulk acoustic wave solidly mounted resonator using SrTiO[sub 3]," Applied Physics Letters **91** (4), 043501 (2007).

[64] M. Streibl, C. Rocke, A. O. Govorov et al., "Novel optoelectronic signal processing via the combination of SAW and semiconductor heterostructures," IEEE Ultrasonics Symposium, 107 (1998).

[65] A. Wixforth, "Interaction of surface acoustic waves, electrons, and light," International Journal of High Speed Electronics and Systems (IJHSES) **10** (4), 1193 (2000).

[66] M. M. de Lima, Jr., R. Hey, J. A. H. Stotz et al., "Acoustic manipulation of electron--hole pairs in GaAs at room temperature," Applied Physics Letters **84** (14),

2569 (2004).

[67] B. Reulet, A. Y. Kasumov, M. Kociak et al., "Acoustoelectric effects in carbon nanotubes," Physical Review Letters **85** (13), 2829 (2000).

[68] J. Ebbecke, C. J. Strobl, and A. Wixforth, "Acoustoelectric current transport through single-walled carbon nanotubes," Physical Review B **70** (23), 233401 (2004).

[69] V. I. Talyanskii, M. R. Graham, and H. E. Beere, "Acoustoelectric Y-branch switch," Applied Physics Letters **88** (8), 083501 (2006).

[70] V. I. Talyanskii and et al., "An acoustoelectric single photon detector," Semiconductor Science and Technology **22** (3), 209 (2007).

[71] J. F. Vetelino, R. Lade, and R. S. Falconer, presented at the IEEE 1986 Ultrasonics Symposium, 1986 (unpublished).

[72] W. P. Jakubik, "Hydrogen detection by single and bilayer sensor structures in Surface Acoustic Wave system," J. Phys. IV France **129**, 117 (2005).

[73] F. C. Huang, Y. Y. Chen, and T. T. Wu, "A room temperature surface acoustic wave hydrogen sensor with Pt coated ZnO nanorods," Nanotechnology **20** (6), 065501 (2009).

[74] S. Parmanand, M. Abhai, and K. Sreenivas, "Ultraviolet photoresponse of porous ZnO thin films prepared by unbalanced magnetron sputtering," Applied Physics Letters **80** (4), 553 (2002).

[75] D. Ciplys, M. S. Shur, N. Pala et al., "Ultraviolet-sensitive AlGaN-based surface acoustic wave devices," Sensors, 2004. Proceedings of IEEE **3**, 1345 (2004).

[76] D. Ciplys, M. S. Shur, A. Sereika et al., "Deep-UV LED controlled AlGaN-based SAW oscillator," physica status solidi (a) **203** (7), 1834 (2006).

[77] Nuri W. Emanetoglu, J. Zhu, Y. Chen et al., "Surface acoustic wave ultraviolet photodetectors using epitaxial ZnO multilayers grown on r-plane sapphire," Apply Physics Letters **85** (17) (2004).

[78] S. Kumar, G. H. Kim, K. Sreenivas et al., "ZnO based surface acoustic wave ultraviolet photo sensor," Journal of Electroceramics **22** (1), 198 (2007).

[79] C. C. Ma, T. J. Huang, and J. M. Yu, "Application of slanted finger interdigital transducer surface acoustic wave devices to ultraviolet array photodetectors," Journal of Applied Physics **104** (3), 033528 (2008).

[80] Z. A. Shana and F. Josse, "Quartz Crystal Resonators as Sensors in Liquids Using the Acoustoelectric Effect," Analytical Chemistry **66** (13), 1955 (1994).

[81] R. Duhamela, L. Roberta, H. Jia et al., "Sensitivity of a Lamb wave sensor with 2 μm AlN membrane," Ultrasonics **44**, e893 (2006).

[82] J. C. Yu and H. Y. Lin, "Sensing liquid density using resonant flexural plate wave devices with sol–gel PZT thin films," Microsystem Technologies **14** (7), 1073 (2008).

[83] N.Yamamoto et al., "Hydrogen Gas Sensor Using Good Characteristics of Lamb Wave," Japanese Journal of Applied Physics **47**, 4024 (2008).

[84] D. Royer and E. Dieulesaint, *Elastic Waves in Solids I: Free and Guided Propagation* (Springer, 2000).

[85] H. Matthews, *Surface Wave Filters: Design, Construction, and Use,*. (Wiley, New York, 1977).

[86] D. P. Morgan, *Surface-Wave Devices for Signal Processing*. (Elsevier, Amsterdam, 1991).

[87] Y. Y. Chen, "Theory, Experimet and Applications of Layered SAW Devices," Doctoral Dissertation, Institute of Applied Mechanics, National Taiwan University, Taipei, Taiwan (In Chinese) (2002).

[88] B. Honein, A. M. B. Braga, P. Barbone et al., "Wave Propagation in Piezoelectric Layered Media with Some Applications," Journal of Intelligent Material Systems and Structures **2** (4), 542 (1991).

[89] T. T. Wu and Y. Y. Chen, "Exact analysis of dispersive SAW devices on ZnO/diamond/Si-layeredstructures," Ultrasonics, Ferroelectrics and Frequency Control, IEEE Transactions on **49** (1), 142 (2002).

[90] Y. Y. Chen, "Exact analysis of Lamb waves in piezoelectric membranes with distinct electrode arragements," Japanese Journal of Applied Physics **48**, 07GA06 (2009).

[91] D. C. Look, "Recent advances in ZnO materials and devices," Materials Science and Engineering B **80** (1-3), 383 (2001).

[92] U. Ozgur, I. A. Ya, C. Liu et al., "A comprehensive review of ZnO materials and devices," Journal of Applied Physics **98** (4), 041301 (2005).

[93] C. Campell, *Surface Acoustic Wave Devices and Their Signal Processing Applications*. (Academic Press, Boston, 1989).

[94] R. H. Tancrell and M. G. Holland, "Acoustic surface wave filters," Proceedings of the IEEE **59**, 393 (1971).

[95] W. R. Smith, H. M. Gerard, J. H. Collins et al., "Analysis of interdigital surface wave transducers by use of an equivalent circuit model," IEEE Transactions on Microwave Theory and Techniques **MTT-17**, 856 (1969).

[96] W. R. Smith, "Experimental distinction between cross-field and in-line three-port circuit models for interdigital transducers," IEEE Transactions on Microwave Theory and Techniques **MTT-17**, 960 (1974).

[97] B. P. Abbott, "A coupling-of-modes model for SAW transducers with arbitrary reflectivity weighting," Ph. D. Dissertation, the Department of Electrical Engineering, the University of Central Florida Orlando, Florida (1989).

[98] S. M. Wang, "The design and measurement of an IF SAW filter," Master Thesis, Institute of Applied Mechanics, National Taiwan University, Taipei, Taiwan (In Chinese) (2002).

[99] T. T. Wu, Y. Y. Chen, and T. H. Chou, "A high sensitivity nanomaterial based SAW humidity sensor," Journal of Physics D: Applied Physics **41** (8), 085101 (2008).

[100] M. H. Huang, Y. Wu, H. Feick et al., "Catalytic growth of zinc oxide nanowires by vapor transport," Advanced Materials **13** (2), 113 (2001).

[101] J. J. Wu and S. C. Liu, "Low-temperature growth of well-aligned ZnO nanorods by chemical vapor deposition," Advanced Materials **14** (3), 215 (2002).

[102] Z. W. Pan, Z. R. Dai, and Z. L. Wang, "Nanobelts of semiconducting oxides," Science **291** (5510), 1947 (2001).

[103] M. H. Huang, S. Mao, H. Feick et al., "Room-temperature ultraviolet nanowire nanolasers," Science **292** (5523), 1897 (2001).

[104] C. J. Park, D. K. Choi, J. Yoo et al., "Enhanced field emission properties from well-aligned zinc oxide nanoneedles grown on the Au/Ti/n-Si substrate," Applied Physics Letters **90** (8), 083107 (2007).

[105] M. Law, L. E. Greene, J. C. Johnson et al., "Nanowire dye-sensitized solar cells," Nat Mater **4** (6), 455 (2005).

[106] A. Dorfman, N. Kumar, and J. Hahm, "Highly sensitive biomolecular fluorescence detection using nanoscale ZnO platforms," Langmuir **22** (11), 4890 (2006).

[107] X. Feng, L. Feng, M. Jin et al., "Reversible super-hydrophobicity to super-hydrophilicity transition of aligned ZnO nanorod films," Journal of the American Chemical Society **126** (1), 62 (2003).

[108] D. Ciplys, M. S. Shur, A. Sereika et al., "Deep-UV LED controlled AlGaN-based SAW oscillator," Physica Status Solidi (a) **203** (7), 1834 (2006).

[109] S. W. Wenzel and R. M. White, "A multisensor employing an ultrasonic Lamb-wave oscillator," Electron Devices, IEEE Transactions on **35** (6), 735 (1988).